

# Designing MOF Nanoarchitectures for Electrochemical Water Splitting

Ben Zhang, Yijuan Zheng, Tian Ma, Chengdong Yang, Yifei Peng, Zhihao Zhou, Mi Zhou, Shuang Li,\* Yinghan Wang,\* and Chong Cheng\*

Electrochemical water splitting has attracted significant attention as a key pathway for the development of renewable energy systems. Fabricating efficient electrocatalysts for these processes is intensely desired to reduce their overpotentials and facilitate practical applications. Recently, metal–organic framework (MOF) nanoarchitectures featuring ultrahigh surface areas, tunable nanostructures, and excellent porosities have emerged as promising materials for the development of highly active catalysts for electrochemical water splitting. Herein, the most pivotal advances in recent research on engineering MOF nanoarchitectures for efficient electrochemical water splitting are presented. First, the design of catalytic centers for MOF-based/derived electrocatalysts is summarized and compared from the aspects of chemical composition optimization and structural functionalization at the atomic and molecular levels. Subsequently, the fast-growing breakthroughs in catalytic activities, identification of highly active sites, and fundamental mechanisms are thoroughly discussed. Finally, a comprehensive commentary on the current primary challenges and future perspectives in water splitting and its commercialization for hydrogen production is provided. Hereby, new insights into the synthetic principles and electrocatalysis for designing MOF nanoarchitectures for the practical utilization of water splitting are offered, thus further promoting their future prosperity for a wide range of applications.

carrier with an extremely high energy density (approximately  $142 \text{ MJ kg}^{-1}$ ) and zero-carbon content, has been regarded as a promising clean fuel.<sup>[1,2]</sup> In this context, electrochemical water splitting, which converts electricity into storable hydrogen, is a viable and efficient solution to mitigate severe energy shortages and greenhouse gas emissions.<sup>[3]</sup> Among these strategies, hydrogen and oxygen evolution reactions, which occur on the cathode and anode, respectively, in a water electrolyzer, are considered as two critical half-reactions of the water-splitting process.<sup>[4]</sup> Theoretically, water splitting requires a thermodynamic Gibbs free energy ( $\Delta G$ ) of approximately  $237.2 \text{ kJ mol}^{-1}$ , corresponding to a standard potential ( $\Delta E$ ) of  $1.23 \text{ V}$  versus a reversible hydrogen electrode (RHE), which allows the thermodynamically uphill reaction to occur in the electrolyzer.<sup>[5]</sup> However, the unfavorable thermodynamics and resulting large overpotential are the main barriers to the scalable implementation of water electrolysis for hydrogen generation.<sup>[6,7]</sup> Currently, noble metal-based electro-

catalysts exhibit the most efficient activity for water splitting, particularly Pt-based hydrogen evolution reaction (HER) catalysts and Ir/Ru-based oxygen evolution reaction (OER) catalysts.<sup>[8,9]</sup> Nevertheless, the scarcity and high price of precious metals severely impede their widespread use in commercial water-splitting applications. Taking these limitations into

## 1. Introduction

Considering the rise in the number of global energy crises and environmental concerns, it is crucial to develop green and sustainable energy resources to substitute nonrenewable sources, such as fossil fuels. Hydrogen ( $\text{H}_2$ ), as an energy


B. Zhang, Y. J. Zheng, Dr. T. Ma, C. D. Yang, Y. F. Peng, Z. H. Zhou, Prof. Y. H. Wang, Prof. C. Cheng  
College of Polymer Science and Engineering  
State Key Laboratory of Polymer Materials Engineering  
Sichuan University  
Chengdu 610065, China  
E-mail: wang\_yh@scu.edu.cn; chong.cheng@scu.edu.cn

Dr. T. Ma  
West China School of Medicine/West China Hospital  
Sichuan University  
Chengdu 610041, China

Dr. M. Zhou  
College of Biomass Science and Engineering  
Sichuan University  
Chengdu 610065, China

Dr. S. Li  
Functional Materials  
Department of Chemistry  
Technische Universität Berlin  
Hardenbergstraße 40, 10623 Berlin, Germany  
E-mail: s.li@tu-berlin.de

Prof. C. Cheng  
Department of Chemistry and Biochemistry  
Freie Universität Berlin  
Takustraße 3, 14195 Berlin, Germany

 The ORCID identification number(s) for the author(s) of this article can be found under <https://doi.org/10.1002/adma.202006042>.

© 2021 The Authors. Advanced Materials published by Wiley-VCH GmbH. This is an open access article under the terms of the Creative Commons Attribution-NonCommercial License, which permits use, distribution and reproduction in any medium, provided the original work is properly cited and is not used for commercial purposes.

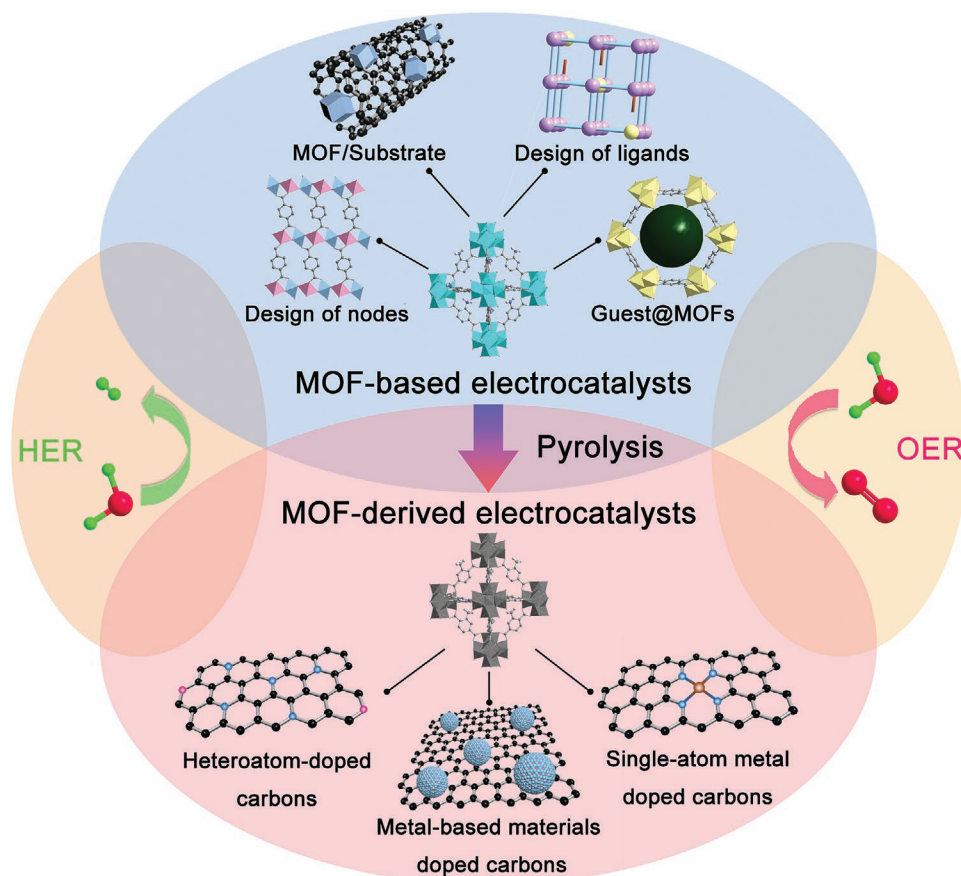
DOI: 10.1002/adma.202006042

consideration, developing non-precious alternatives with excellent activity and durability is a challenging but essential task.

As a new class of highly porous materials, metal–organic frameworks (MOFs) consisting of organic ligands and metal ions or clusters have high crystallinity and long-range order.<sup>[10,11]</sup> Owing to the intrinsic features of large surface areas, adjustable chemical components, tunable pore structures, and diverse topologies, a large number of MOFs have been employed for electrochemical water splitting.<sup>[12–17]</sup> Moreover, the properties of MOFs can be improved or modified by coupling various functional materials, including polyoxometalates (POMs), metal compounds, carbon nanotubes (CNTs), and other conductive substrates to form guests@MOFs or MOF/substrates.<sup>[18–22]</sup> The superior electrochemical performance of water splitting can be achieved from the combined advantages of more active sites and enhanced conductivity through functionalization. Additionally, the MOF-based skeleton allows the rearrangement of the elements at the molecular and atomic levels during pyrolysis. Thus, MOFs or MOF-based composites can act as templates for the synthesis of MOF-derived porous, carbon-based nanomaterials, such as metals, metal compounds, and single-atom catalysts (SACs), under thermal treatments. The pyrolysis of MOFs with ordered calcination modulates various characteristics, such as conductivity and porosity, surface area, stability, and catalytic activity; hence, such derivatives are highly interesting for water splitting.<sup>[23–30]</sup> Based on these guidelines, diverse MOF-based/derived materials have been reported in the past five years. However, a

comprehensive review summarizing MOF-based/derived materials with well-defined synthetic methods, chemical compositions, nanostructured morphologies, electrocatalytic activities, and reaction mechanisms is urgently needed to provide strong inspiration and direct future developments in engineering MOF-based/derived electrocatalysts for water splitting.

Herein, this new progress report provides pivotal advances and commentaries on recent research on engineering MOF nanoarchitectures for efficient electrochemical water splitting. First, the design of catalytic centers for MOF-based/derived electrocatalysts is summarized and compared from the aspects of synthetic strategy, chemical composition optimization, and structural functionalization at the atomic and molecular levels (**Scheme 1**). Second, we focus on the electrocatalytic performance of MOF-based/derived materials for the HER, OER, and bifunctional catalysts. In particular, significant attention has been paid to summarize the fast-growing breakthroughs on the catalytic activity, identification of the highly active sites, and fundamental mechanisms of MOF-based/derived electrocatalysts with unprecedented water splitting performance. Finally, we provide a comprehensive commentary on the current primary challenges and future perspectives on the design and commercialization of MOFs and their derived electrocatalysts for water splitting. We believe that this progress report may offer new insights into the synthetic principles and electrocatalysis in designing MOF nanoarchitectures for practical utilization in water splitting, thus further promoting their future prosperity for a wide range of applications.



**Scheme 1.** Illustration for the design of MOF nanoarchitectures for electrochemical water splitting.

## 2. Design of MOF-Based/Derived Electrocatalytic Materials

### 2.1. MOF-Based Electrocatalytic Materials

Owing to their high surface areas, controllable porous structures, and diverse active metal sites or organic linkers, MOF-based electrocatalytic materials have been extensively investigated in the field of water splitting. In this section, recent advanced synthetic strategies of MOF-based electrocatalytic materials as promising electrocatalysts are discussed in the sequence of pristine MOFs, guest-encapsulated MOFs (guests@MOFs), and substrate-modified MOFs (MOF/substrates).

#### 2.1.1. Pristine MOFs

Much attention has been paid to the selection and optimization of metal sites and organic ligands at an atomic level, which is considered a powerful strategy to regulate the electrocatalysis behavior of pristine MOFs. The component design could readily modulate the physical and chemical properties of MOFs, such as electron structures, conductivity, bonding energy of the intermediates, and stability. The commonly used strategies to optimize the catalytic performance of pristine MOFs are introducing multivalent metal sites and heterometallic doping, incorporating functional groups into organic ligands, adsorbing multiple ions onto the organic ligands or metal nodes, and immobilizing conjugated organic ligands in the skeletons.

*Structural Design of Metal Nodes in Pristine MOFs:* Some monometallic MOFs, such as Co-MOFs,<sup>[31]</sup> Cu-MOFs,<sup>[32]</sup> and Zr-MOFs,<sup>[33]</sup> have witnessed rapid and significant development in electrocatalysis. Moreover, bimetallic and trimetallic sites have shown catalytic activity in the OER. Zhao et al. designed and synthesized NiCo bimetal-organic framework nanosheets (NiCo-UMOFNs) that achieved extraordinary electrocatalytic activity toward the OER under alkaline conditions (Figure 1Aa–d).<sup>[34]</sup> Among the four catalysts mentioned, the NiCo-UMOFNs achieved a very low overpotential of 250 mV at 10 mA cm<sup>-2</sup> and a low Tafel slope (42 mV dec<sup>-1</sup>) in an N<sub>2</sub>-saturated 1 M KOH solution (Figure 1Ae,f). Subsequent density functional theory (DFT) studies confirm that the high electrocatalytic activity is attributed to the coordinatively unsaturated metal center and the coupling effect between Co and Ni. Zhang et al. reported the facile ambient temperature synthesis of a unique trimetallic MOF nanofoam (Figure 1Ba) with controllable molar ratios.<sup>[35]</sup> The transmission electron microscopy (TEM) image of the (Ni<sub>2</sub>Co)<sub>1-x</sub>Fe<sub>x</sub>-MOF-NF and high-resolution TEM (HRTEM) analysis after the OER are illustrated in Figure 1Bb,c. The overpotential values needed for different molar ratios to achieve a current density of 10 mA cm<sup>-2</sup> in 1.0 M KOH are summarized in Figure 1Bd, in which (Ni<sub>2</sub>Co)<sub>1,0.925</sub>Fe<sub>0.075</sub>-MOF-NF has the lowest overpotential (257 mV). The component design of metal nodes is a simple and efficient strategy to purposefully introduce catalytically active metal nodes into MOFs for various types of electrocatalysis and take advantage of the synergistic effect between the multi-metal elements. However, challenges still need to be addressed: 1) it is difficult to introduce multiple metal nodes into

MOFs while retaining the original character of the structure; 2) the real active sites and the catalytic mechanism are difficult to identify.

*Structural Design of Organic Ligands in Pristine MOFs:* Another way to adjust the characteristics of MOFs for electrocatalysts is to modify the chemical composition of the organic ligands. It has been theoretically and experimentally studied that UiO-66 can be functionalized with single- and dual-functionalized linkers (OH, NH<sub>2</sub>, or SH).<sup>[36]</sup> Syzgantseva et al. studied and summarized the impact of the functional groups and scaffolds of ligands in MOFs.<sup>[37]</sup> The influence of F, Cl, Br, I, OH, SH, CN, NH<sub>2</sub>, NO<sub>2</sub>, SO<sub>3</sub>H, PO<sub>3</sub>H<sub>2</sub>, and NMe<sub>2</sub> in MIL-125 were studied systematically. Meanwhile, for UiO-66, F, Cl, Br, I, OH, SH, CN, NH<sub>2</sub>, and NO<sub>2</sub> were considered. The results implied that the electron-donating groups would boost the energy of the ligand-centered states, whereas the electron-withdrawing groups could facilitate the opposite effect. With the increase in the degree of conjugation in the organic ligand, MOFs could have fewer electrons localized on it. These observations support the idea that the component design of organic ligands could adjust the electron structure of MOFs, subsequently optimizing the catalytic performance. Nevertheless, little attention has been paid to the modification of organic ligands by introducing functional groups in the field of electrocatalysis due to the complex and varying effects of the side group.

Structural defects may offer opportunities to tune and optimize the performance of electrocatalysts because of the modulation of the electronic and geometric structures. Recent work on missing linker defects of the UiO-66-type framework unambiguously demonstrated that structural defects mostly affect the local node geometry and, therefore, offer an alternative route to node modification.<sup>[38]</sup> Furthermore, Zheng et al. applied a NaBH<sub>4</sub> treatment to modulate the defect concentration to optimize the electrochemical performance.<sup>[39]</sup> It has been revealed that the defects created in MOFs will lead to redistributed electronic configurations, which may provide defective conducting channels, thus resulting in enhanced OER catalytic activity. Additionally, the coordinatively unsaturated sites associated with organic linker defects could serve as catalytic sites and enhance the intrinsic activity of the catalytic sites. For instance, the missing ligands of Co<sub>2</sub>(OH)<sub>2</sub>(C<sub>8</sub>H<sub>4</sub>O<sub>4</sub>) (CoBDC) modified the local coordination geometry of Co<sup>2+</sup> and generated unsaturated Co<sup>2+</sup> sites, achieving remarkable OER catalytic activity with an extremely low overpotential of 241 mV at 100 mA cm<sup>-2</sup> with Ni foam as the substrate.<sup>[14]</sup> From the above examples, the defect engineering of MOFs with a controllable density of defects is generally followed by electron localization, lattice distortion, and bond breaking and reforming, resulting in a larger number of active sites. Nonetheless, several significant challenges still exist: 1) high densities of defects may reduce electroconductivity, thereby reducing the electrocatalytic activity; 2) it is difficult to define the actual reactive sites due to the various types of defects.

#### 2.1.2. Guests@MOFs

In many cases, due to the inherent defects of MOFs, such as poor conductivity and inferior functionality, pristine MOFs



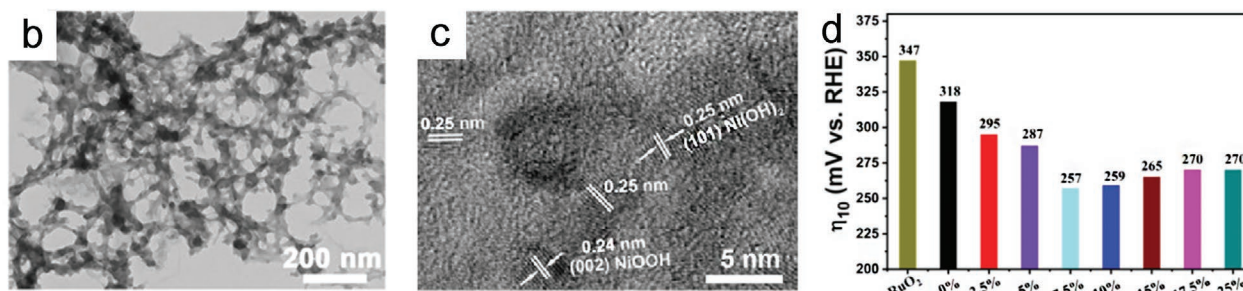
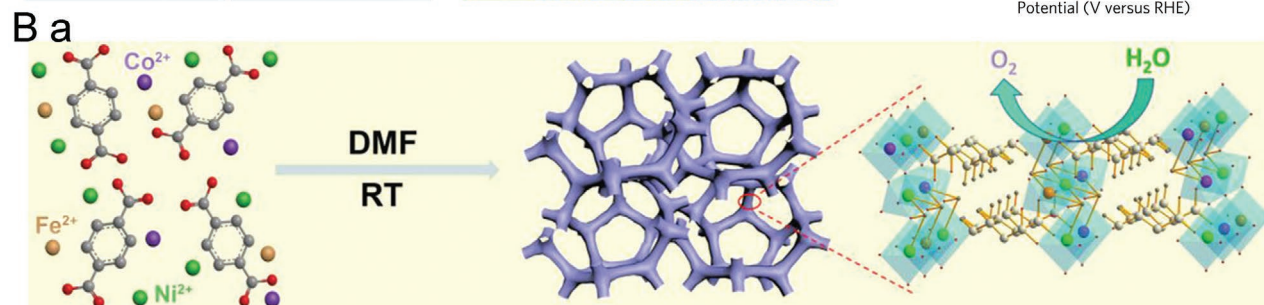
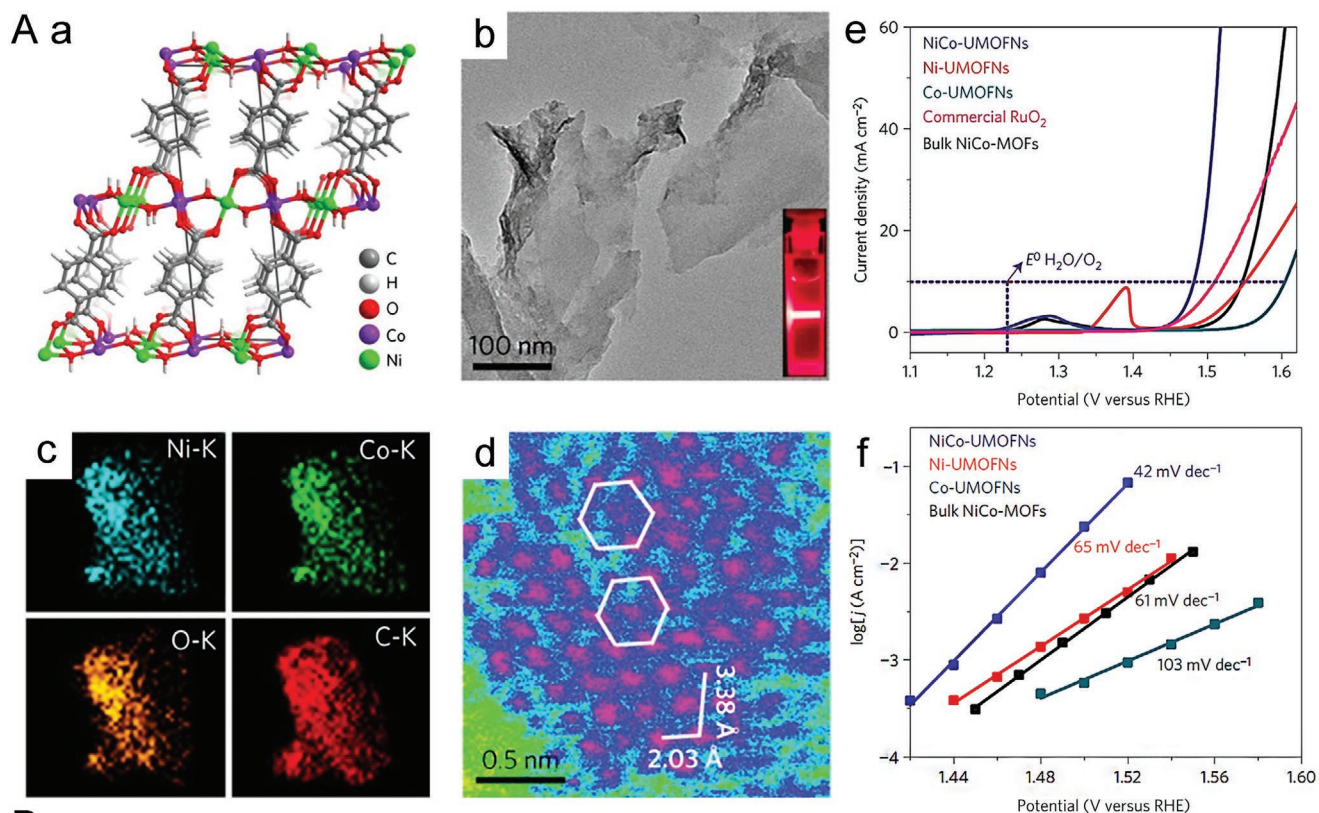


**Figure 1.** A) Crystal structure of NiCo-UMOFNs. b) TEM, c) energy-dispersive X-ray spectroscopy (EDS) mapping, and d) high-angle annular dark-field scanning transmission electron microscopy (HAADF-STEM) images of NiCo-UMOFNs, showing metal atoms (pink), light elements (blue), and background (green). e) Linear sweep voltammetry (LSV) curves and f) Tafel plots of various catalysts. A) Reproduced with permission.<sup>[34]</sup> Copyright 2016, Springer Nature. B) a) Synthesis process and b) TEM image of hierarchical  $(\text{Ni}_2\text{Co}_1)_{0.95}\text{Fe}_{0.05}\text{-MOF-NF}$  (NF: Ni foam) c) HRTEM analysis after the OER. d) The overpotential of different molar ratios at  $10 \text{ mA cm}^{-2}$ . B) Reproduced with permission.<sup>[35]</sup> Copyright 2019, Wiley-VCH.

could not provide an ideal performance to meet the needs of electrocatalysts for practical industrial applications. Owing to their well-defined pore structures and various organic linkers,

MOFs can be regarded as essential materials to introduce active guest species, such as metal nanoparticles,<sup>[20,40]</sup> metal complexes,<sup>[41–43]</sup> and POMs,<sup>[44]</sup> through covalent or noncovalent



bonds (electrostatic,  $\pi$ - $\pi$  interactions, host-guest interactions). In many cases, the synergistic effect between the guests and MOFs could also improve the catalytic activity.

The immobilization of precious metals with functional supports could be an effective strategy to acquire excellent electrocatalysts because of the desirable dispersity and regulated interfaces.<sup>[45,46]</sup> Rui et al. prepared a 2D Ni-MOF@Pt hybrid with well-defined interfaces via in situ deposition of Pt nanoparticles,<sup>[20]</sup>

achieving improved electrochemical HER performance under both acidic and alkaline conditions (Figure 2Aa,b). As shown in Figure 2Ac, X-ray absorption fine structure (XAFS) analysis demonstrated the dominant metallic state of Pt, and the result of the Fourier transformation of the extended XAFS (EXAFS) (Figure 2Ad) indicated the possible strong interaction in the Ni-MOF@Pt. The as-prepared Ni-MOF@Pt exhibited excellent electrocatalysis behavior in 1 M KOH with an overpotential of

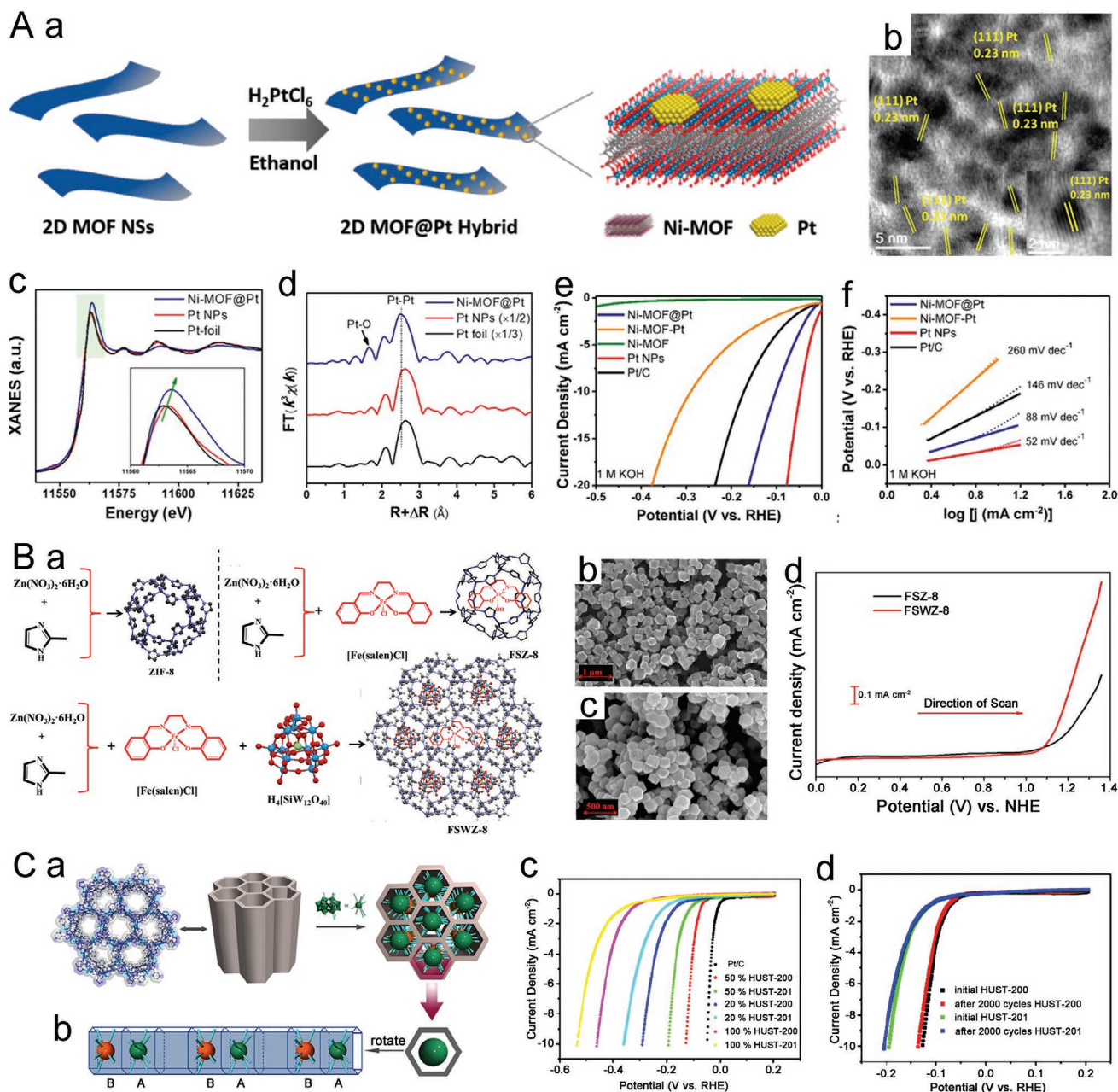


**Figure 2.** A) a) Schematic illustration for the preparation of the 2D MOF@Pt heterostructure. b) HRTEM image of 2D MOF@Pt hybrid nanosheets. c) XANES and d) Fourier transform-EXAFS (FT-EXAFS) profiles of Ni-MOF@Pt, pure Pt nanoparticles, and Pt foil for the Pt  $L_{111}$ -edge. e) LSV curves and f) corresponding Tafel slopes in 1 M KOH. A) Reproduced with permission.<sup>[20]</sup> Copyright 2019, American Chemical Society. B) a) Schematic representations of the syntheses of ZIF-8, FSZ-8, and FSWZ-8. b,c) FESEM images of FSZ-8 (b) and FSWZ-8 (c). d) LSVs of FSWZ-8 and FSZ-8 in 0.1 M KCl. B) Reproduced with permission.<sup>[49]</sup> Copyright 2020, American Chemical Society. C) a) 3D POM-encapsulated metal-organic nanotube. b) Diagram of POM linkage mode in a 1D POM-encapsulated metal-organic nanotube. c) LSV curves of the catalysts. d) Cycling stability tests of the catalysts. HUST-200 (X = P) and HUST-201 (X = As). C) Reproduced with permission.<sup>[44]</sup> Copyright 2018, American Chemical Society.

102 mV at 10 mA cm<sup>-2</sup>, outperforming that of the commercial Pt/C (Figure 2Ae–f). The strong Pt–O covalent bonds in Ni-MOF@Pt are believed to enable ideal interfacial interaction and facilitate the electron transfer of the Pt nanoparticles. This interface engineering method provides a broad prospect for developing new functional MOFs and other 2D nanocomposites with great potential for water-splitting applications.

The incorporation of base metal complexes into MOFs has been investigated to enhance the catalytic properties. Lin et al. reported that UiO-67 doped with [Ru(tpy)(dcbpy)OH<sub>2</sub>]<sup>2+</sup> (tpy = 2,2':6',2'-terpyridine, dcbpy = 5,5'-dicarboxy-2,2'-bipyridine) via coordination bonds for electrochemical water oxidation achieved a high turnover frequency (TOF) and good electrochemical stability in a buffered solution (pH = 7).<sup>[47]</sup> Meanwhile, the strategy to incorporate metal complexes into MOFs, such as porphyrins and phthalocyanines, could further improve the stability under the highly oxidative environment in OER catalysis, thus guaranteeing efficient and stable catalytic performance. For instance, the Co-tetramethoxyphenyl porphyrin has been incorporated into the cavity of ZIF-8 via host/guest interaction and functions as a high-performance bifunctional electrocatalyst for both the OER and oxygen reduction reaction (ORR). The strong interactions between the guest molecule and ZIF-8 host ensure excellent structural and electrochemical stability.<sup>[48]</sup>

Recently, the metal–salen complex, one of the closest analogs to metal porphyrin complexes, has also received increasing attention for OER catalysis. The Fe–salen complex and POM co-loaded ZIF-8 have been reported as electrocatalytically active OER materials. The synthesis of ZIF-8, [Fe(salen)(OH)]@ZIF-8 (FSZ-8), and ([Fe(salen)(OH)]<sup>+</sup>H<sub>4</sub>[SiW<sub>12</sub>O<sub>40</sub>]<sup>-</sup>·HCl)@ZIF-8 (FSWZ-8) is shown in Figure 2Ba.<sup>[49]</sup> Figure 2Bb,c presents the field emission SEM (FESEM) images of FSZ-8 and FSWZ-8, respectively. The LSV of FSWZ-8 and FSZ-8 (Figure 2Bd) demonstrates that FSWZ-8 could achieve a higher water oxidation current than FSZ-8 under the same potential, proving the benefits of the strong interactions between the co-encapsulated Fe–salen and POM.

POMs are highly soluble inorganic nanoclusters composed of polyanion clusters and counter cations, which can be immobilized in the pores of MOFs via covalent or noncovalent bonds to serve as different kinds of active sites for many catalytic reactions.<sup>[50,51]</sup> Mukhopadhyay et al. reported an efficient and robust OER catalyst in neutral pH through the encapsulation of [CoW<sub>12</sub>O<sub>40</sub>]<sup>6-</sup> inside the pores of ZIF-8. Moreover, POM (X<sub>2</sub>W<sub>18</sub>O<sub>62</sub>, X = P/As)-encapsulated metal–organic nanotubes, [Cu<sup>II</sup><sub>6</sub>(pzta)<sub>6</sub>(bpy)<sub>3</sub>(X<sub>2</sub>W<sub>18</sub>O<sub>62</sub>)]·2H<sub>2</sub>O, were synthesized as shown in Figure 2Ca,b.<sup>[44]</sup> These two types of POM-encapsulated MOF with Cu–O covalent bonds show high activity and stability toward the HER under acidic conditions (Figure 2Cc,d). In particular, the best catalyst achieved a relatively low overpotential of 131 mV to reach a current density of 10 mA cm<sup>-2</sup>. It has also been reported that POMs can migrate within MOFs if induced by thermal treatment.<sup>[21]</sup> Additional investigation is required to insert other types of POMs to explore their effects on the HER or OER catalytic activities.

Bimetallic alloys or core–shell nanoparticles on MOF substrates are promising catalysts because they typically present higher catalytic activity than their monometallic counterparts. Ma et al. synthesized MOF-encapsulated bimetallic

nanoparticles with enhanced OER performance and stability via the in situ etching of Cu–Ni nanostructures.<sup>[52]</sup> TEM/STEM images and EDS mapping showed no significant changes in the structure and element distribution after the electrochemical measurements. In particular, Ni-Cu@Cu-Ni-MOF presented the lowest overpotential at a current density of 10 mA cm<sup>-2</sup> and the smallest Tafel slope of 98 mV dec<sup>-1</sup>. Notably, for the strategy to introduce electrocatalytic nanomaterials into MOFs, the locality and loading number of the functional materials must be regulated and controlled meticulously to ensure the maximum utility of the active sites. The uniform dispersion of the guest materials inside the MOF nanocrystals could significantly shorten the charge transfer distance and facilitate the catalytic reaction.

In brief, loading functional materials inside MOFs is a promising strategy to yield heterogeneous catalysts with high activity and stability. The confined materials could serve as the active sites and deliver outstanding catalytic functionality, and uniform dispersion of the guest materials inside the MOF crystals could significantly shorten the charge transfer distance and facilitate the catalytic reaction. However, because organic ligands can partition the metal nodes of MOFs and guest nanoparticles, the interaction between the encapsulated metal nanoparticles and MOFs is weak. Strengthening the interaction between the host and guest (such as the Pt–O and Cu–O covalent bonds mentioned above) is the key to enhancing the structural stability and catalytic activity.

### 2.1.3. MOF/Substrates

Functional materials as substrates to support MOFs are another way of introducing functional materials into pristine MOFs. Quite a few MOFs have been assembled onto various substrates as building blocks; this not only endows more exposure to the active sites of the catalysts but also improves the conductivity of the MOFs. For instance, Duan et al. prepared ultrathin nanosheet arrays of 2D MOFs on various supports through a facile route of one-step chemical bath deposition, showing superior performance for the OER, HER, and overall water splitting.<sup>[53]</sup> An NiFe-MOF with the presence of Ni foam (NF) as substrates demonstrated the best OER performance in a 0.1 M KOH electrolyte, achieving an overpotential of 240 mV at 10 mA cm<sup>-2</sup> and a small Tafel slope of 34 mV dec<sup>-1</sup>.

Recently, Cheng et al. reported a lattice-strained NiFe-MOF nanosheet array with foamed Ni as a substrate synthesized through a low-temperature hydrothermal approach, exhibiting excellent electrocatalytic performance as a bifunctional oxygen electrocatalyst.<sup>[54]</sup> The mechanism of lattice expansion of NiFe-MOF under ultraviolet light is shown in Figure 3Aa. Ultraviolet treatment leads to the enlargement of the interlayer of the lattice-strained NiFe-MOF from 11.6 to 12.1 Å (Figure 3Ab,c). Lattice-strained NiFe-MOFs exhibit extraordinary OER and ORR activities, achieving comparable activity to RuO<sub>2</sub> and Pt/C (Figure 3Ae). Notably, the 4.3%-MOF catalyst shows mass activity of 2000 and 3100 A g<sub>metal</sub><sup>-1</sup> at overpotentials of 300 and 400 mV, respectively, which are significantly higher than those of commercial RuO<sub>2</sub> and pristine NiFe-MOF (Figure 3Af). The catalyst also exhibited superior Faradaic efficiency and desirable stability after 200 h of continuous OER (Figure 3Ag). As illustrated in Figure 3Ad, the improvement



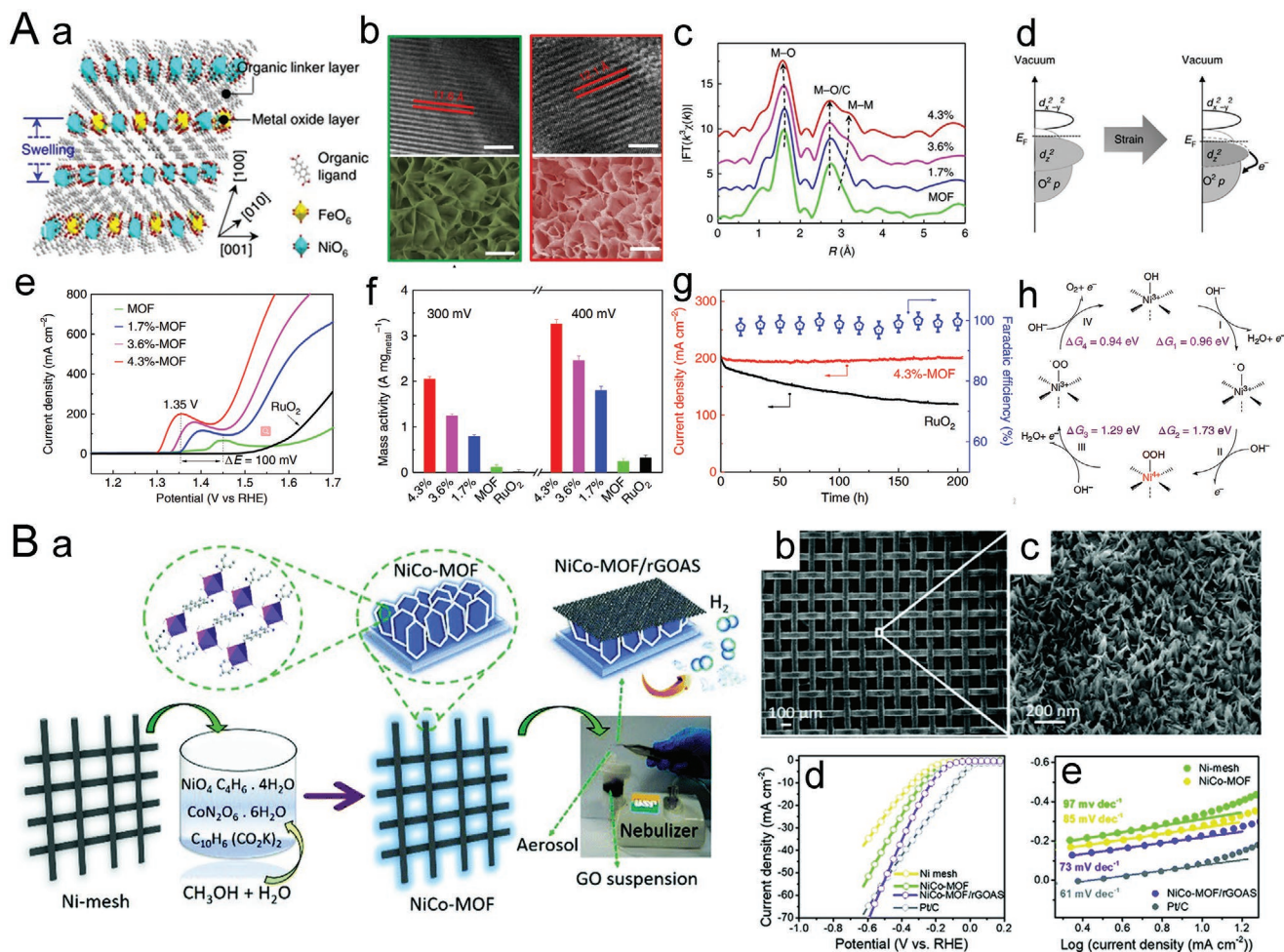


**Figure 3.** A) a) Schematic diagram of the crystal structure change of NiFe-MOF under ultraviolet light. b) HRTEM (top) and SEM (bottom) images of the pristine and 4.3%-MOFs. Scale bars represent 5 nm for HRTEM and 200 nm for SEM. c) Ni K-edge FT-EXAFS spectra of lattice-strained NiFe-MOF. d) Schematic representation of the electron exchange for the lattice-strained MOF. e) LSV curves and f) mass activity of the OER. g) OER stability for RuO<sub>2</sub> and the 4.3%-MOF and OER Faradaic efficiency of the 4.3%-MOF. h) OER catalytic mechanism of the lattice-strained MOFs. B) A) Reproduced with permission.<sup>[54]</sup> Copyright 2019, Springer Nature. B) A schematic illustrating the synthetic procedures for NiCo-MOF/rGOAS. **a**) Schematic diagram of the synthesis of NiCo-MOF on Ni-mesh. **b**) and **c**) SEM images of NiCo-MOF-coated Ni-mesh (**b**) and the nanoflocks of NiCo-MOF (**c**). **d**) HER LSV curves and **e**) Tafel plots in 0.1 M KOH. **B**) Reproduced with permission.<sup>[18]</sup> Copyright 2018, Royal Society of Chemistry.

in the OER and ORR catalytic performance of the NiFe-MOF may be ascribed to the change in the electron structure driven by the tensile lattice strain. The OER catalytic mechanism diagram in Figure 3Ah shows that NiFe-MOF undergoes a quick and efficient four-electron pathway for oxygen electrocatalysis, for either the ORR or OER, as the key intermediates superoxide \*OOH species emerge on the high-valence Ni<sup>4+</sup> active sites.

Khalid et al. reported a bimetallic NiCo-MOF that was directly grown on Ni-mesh and wrapped by a graphene oxide aerosol skeleton, providing a highly available active surface area and showing improved electrocatalytic activity for the HER in an alkaline medium (Figure 3Ba).<sup>[18]</sup> Figure 3Bb,c shows that NiCo-MOF was homogeneously grown on the Ni-mesh. The catalytic performance apparently increased owing to the electronic coupling between NiCo-MOF and rGOAS and the Ni-mesh substrate, ensuring a strong electron transfer within the composite. The LSV curves and Tafel values suggested that the rGOAS-covered nanoflocks led to a profound improvement in

the HER performance (Figure 3Bd,e). The physicochemical interactions between the rGOAS and NiCo-MOF, as well as its unique architecture, guarantee excellent electroconductivity, mass transport of the electrolyte, and high exposure of the active sites, subsequently leading to a superior HER catalyst.

Growing the MOF on the substrate can not only inherit the advantages of pristine MOFs but also provide a flexible and effective strategy to increase the macro- or mesoporosity for mass transport and facilitate the exposure of active sites during electrocatalysis. Moreover, attaching MOFs to high-conductivity substrates may overcome the limited electrical conductivity of pristine MOFs. Nonetheless, MOF/substrates catalysts are still in their infancy, and some underdeveloped issues still need to be resolved: 1) hybridization with substrates may block the intrinsic micropores of the MOFs, resulting in poor mass transport; 2) it is critical to design MOF/substrates catalysts with enhanced stability in aqueous media, particularly in acidic and basic media.



In summary, pristine MOFs can theoretically be employed as electrocatalysts to maximize the electrocatalytic surface area and precisely adjust the active sites straightforwardly by the rational selection and modification of the organic ligands and metal nodes. For example, incorporating nonbridging ligands into the MOF could significantly improve the electrocatalytic performance. Converting bulk MOF crystals into 2D nanosheets could also enable a higher exposure of the active surface sites. Designing bimetallic MOFs may further optimize the electrocatalytic performance for water splitting because of the synergistic effect between the multi-metal elements. Nevertheless, the inferior conductivity, controversial stability, and generally poor activity of MOFs hinder the extensive development of pristine MOFs for electrocatalysis. Synthesizing the  $\pi$ -conjugated structure with transition metal atoms and aromatic organic ligands as precursors could also provide a promising pathway to achieve highly conductive MOF-based electrocatalysts.

Furthermore, benefiting from the tunable pore structures of the MOFs, functional nanomaterials, such as metal nanoparticles, metal complexes, and POMs, can be encapsulated inside MOFs to form guest@MOFs. The resulting MOF nanocomposites can always achieve multifaceted catalytic activity or significantly improved conductivity. In many cases, the synergistic and strong interactions between the guests and MOFs could further enhance the catalytic performance. Meanwhile, the uniform dispersion of the guest materials inside the MOF crystals could improve the stability of the catalysts. For MOF/substrates, the functional materials serve as substrates that generally contribute to the dispersion and stability of the MOFs and may also improve the electrical conductivity in many cases.

## 2.2. MOF-Derived Electrocatalytic Materials

Since the research of MOF-5 calcined into carbons was first reported in 2008,<sup>[55]</sup> carbon-based materials derived from MOFs, featuring high conductivity and well-dispersed catalytic sites, have been increasingly employed as highly efficient electrocatalysts. During the pyrolysis of the MOF synthesis, the organic linkers are converted to a highly porous graphitic carbon matrix, and the metal nodes transform into metal compounds, alloys, or single-atom dopants in carbon materials. Herein, the design strategies of MOF-derived carbon-based catalysts are presented in detail.

### 2.2.1. MOF-Derived Metal-Free Carbon Electrocatalysts

Carbon materials with heteroatomic dopants (e.g., B, N, P, S, etc.) have drawn increasing attention because of their high conductivity, erosion resistance, and excellent catalytic performance. Some reports have proved that metal-free carbon nanomaterials can catalyze the OER<sup>[56,57]</sup> and HER.<sup>[58,59]</sup> Recently, MOFs have been regarded as ideal templates for producing carbon nanomaterials owing to their large surface area, high conductivity, and affordable price. Heteroatom-containing MOFs can be employed as precursors to obtain metal-free carbon-based electrocatalysts by carbonization. Lei et al. demonstrated that MOF-derived N- and O-doped carbon materials could be utilized for the electrochemical splitting of water. This bifunctional catalyst was prepared by calcinating the ZIF-8 precursor, followed by the electrochemical activation of the catalytic sites (Figure 4a).<sup>[60]</sup> As revealed by energy-dispersive X-ray

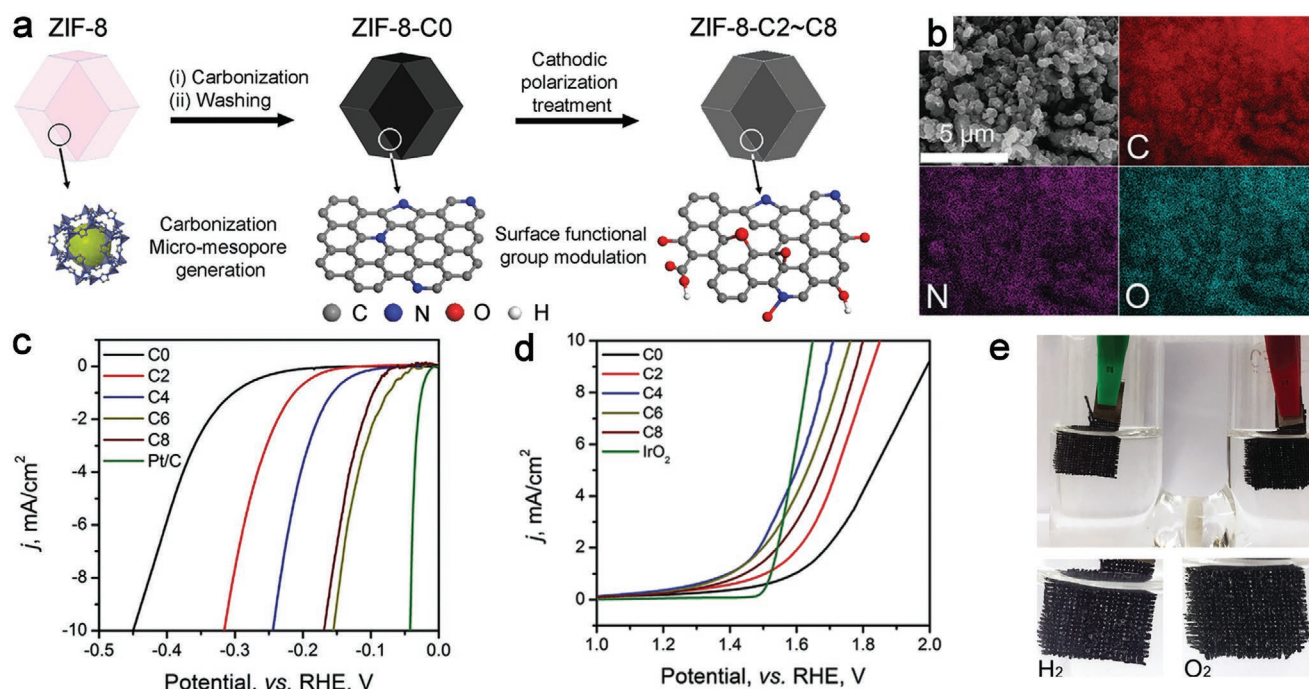


**Figure 4.** a) Schematic of the fabricated carbon electrocatalysts. b) EDX elemental maps of ZIF-8-C<sub>6</sub>. c) HER and d) OER LSV polarization curves. e) Photograph of the electrolyzer using ZIF-8-C<sub>6</sub> as the HER electrocatalyst and ZIF-8-C<sub>4</sub> as the OER electrocatalyst. a–e) Reproduced with permission.<sup>[60]</sup> Copyright 2018, Royal Society of Chemistry.

spectroscopy (EDX), N and O were uniformly dispersed and anchored in the MOF-derived porous carbon matrix (Figure 4b). The excellent electrocatalysis behavior could be attributed to the modulated N- and O-containing surface groups caused by the electrochemical activation (Figure 4c–e). The carbonaceous materials with heteroatomic dopants can also be synthesized by the calcination of MOFs with a highly porous nature and controllable nanostructures under certain atmospheres, like  $\text{NH}_3$ ,  $\text{H}_2\text{S}$ , and  $\text{PH}_3$  gases.<sup>[23,61,62]</sup> For instance, Liu et al. reported an efficient trifunctional electrocatalyst with N- and P-doping synthesized by the calcination of MOF precursors under a  $\text{PH}_3$  atmosphere.<sup>[63]</sup>

For the synthesis of heteroatom-doped carbons with organic ligands containing heteroatoms as precursors, heteroatom doping will be more uniform, but the design of appropriate precursors is more complex. Using certain gas environments (e.g.,  $\text{NH}_3$ ,  $\text{H}_2\text{S}$ , and  $\text{PH}_3$ ) as an external heteroatom source is a feasible and straightforward strategy, but the dispersion of the heteroatoms is relatively poor. To date, MOF-derived carbon materials for electrochemical water splitting have rarely been reported, which may be caused by the limited intrinsic electrocatalytic of these metal-free sites. It is still a great challenge to design MOF-derived metal-free carbon materials with excellent electrochemical water splitting performance.

### 2.2.2. Metal- and Alloy-Doped Carbon Electrocatalysts

In recent years, metals and alloy nanoparticles supported by heteroatom-doped carbon materials have become a thriving topic for designing highly efficient electrocatalysts.<sup>[64,65]</sup> Through the pyrolysis of MOFs in the presence of carbon or external reductive agents, metal ions around organic ligands (e.g., Co, Ni, and Fe ions) could be reduced in situ to metal or alloy nanoparticles encapsulated in a heteroatom-doped carbon frame, which exhibits excellent catalytic performance and stability owing to its highly adjustable metal composition and robust carbon structure.<sup>[66–71]</sup> As representatives of MOFs, there are many reports about zeolite imidazole frameworks (ZIFs) as precursors to prepare metal-nitrogen-carbon electrocatalysts,<sup>[24,72–81]</sup> for instance, the porous cage structure of N-doped carbon nanotubes (NCNTs) synthesized via the simple pyrolysis of polyhedral ZIF-67 particles.<sup>[72]</sup> Thus, enhanced electrocatalytic performance and durability for the ORR and OER were observed, which were mainly attributed to the synergistic effect between the N dopants and restricted Co nanoparticles in the CNTs, the NCNTs structure, and the rugged porous cage structure. Li et al. developed a series of Co/Zn bimetallic zeolitic imidazolate frameworks (BMZIF) that served as precursors to synthesize porous carbon nanomaterials loaded with Co nanoparticles ( $\text{Co@NC-}x/y$ ) and exhibited exceedingly high activity for bifunctional oxygen electrocatalysis.<sup>[73]</sup> Recently, Wang et al. reported a 2D dual-metal (Co/Zn), leaf-like ZIF-pyrolysis routine for scalable preparation to encapsulate Co nanoparticles within N-doped CNTs.<sup>[74]</sup> The resultant Co-N-CNTs were shown to be excellent bifunctional air electrodes for primary and rechargeable Zn–air batteries. Noble-metal electrocatalysts can also be synthesized using MOFs as precursors. Qiu et al. synthesized Ru-based electrocatalysts that exposed massive Ru active

sites (Ru-HPC, Ru-decorated hierarchically porous carbon) with bimetallic CuRu-MOFs serving as templates for highly efficient hydrogen evolution (Figure 5Aa,b).<sup>[70]</sup> As revealed by X-ray diffraction (XRD) patterns (Figure 5Ae), the less active Cu species of CuRu-C were etched by an  $\text{FeCl}_3$  solution to achieve Ru-HPC. Meanwhile, the results of Brunauer–Emmett–Teller (BET) surface areas and TEM images revealed that abundant meso- and macropores were generated in situ (Figure 5Ac,d). Remarkably, Ru-HPC presented desirable catalytic activity for the HER, outperforming the commercial Pt/C by achieving a current density of  $25 \text{ mA cm}^{-2}$  at an overpotential of 22.7 mV (Figure 5Af).

Metal alloy nanomaterials, including FeNi,<sup>[82,83]</sup> FeCo,<sup>[84–86]</sup> IrCo,<sup>[87]</sup> and CoNi alloys,<sup>[88,89]</sup> can also be obtained from MOFs by pyrolysis for application in the field of electrocatalysts. Recently, Zhang et al. reported FeCo bimetallic N-doped porous carbons (FeCo-C/N) obtained from the calcination of yolk–shell-structured ZIFs.<sup>[84]</sup> The obtained FeCo-C/N exhibited excellent ORR performance and good OER activity because of its unique structural and compositional features. Xu et al. reported a self-template approach to preparing open carbon cages with a hydrangea-like superstructure by the morphology-controlled thermal transformation of core@shell MOFs.<sup>[85]</sup> The direct calcination of core@shell Zn@Co-MOFs could be used to construct well-defined open-wall carbon cages. However, the introduction of guest  $\text{Fe}^{3+}$  ions into the Zn@Co-MOF precursor will lead to the self-assembly of open carbon cages into a hydrangea-like 3D superstructure connected by CNTs, which are grown in situ on the Fe–Co alloy nanoparticles formed during the calcination of Fe-doped Zn@Co-MOFs. The as-prepared composite exhibits excellent performance as an air cathode catalyst in a Zn–air battery owing to its unique superstructure.

Xiong et al. reported a group of optimized bimetallic MOF-derived Co–Fe alloys trapped within the carbon nanocomposites via a combination of the typical self-assembly of MOFs and a guest–host method.<sup>[86]</sup> Among them,  $\text{Zn}_6\text{Co}$  has been proven to be a compositionally optimal precursor for synthesizing bimetallic nanoparticle-carbon composite materials with the incorporation of external Fe (Figure 5Ba,b). As revealed by STEM and EDX spectroscopy (Figure 5Bc–f),  $\text{Co}_{0.9}\text{Fe}_{0.1}$  bimetallic nanoparticles, with a uniform distribution of Co and Fe and a Co/Fe ratio of 9:1, were uniformly dispersed and anchored in the MOF-derived porous carbon matrix. The resulting nanocomposite exhibited excellent stability after 30 000 cycles in alkaline solution due to its compositional and structural integrity (Figure 5Bg).

### 2.2.3. Metal-Compound-Doped Carbon Electrocatalysts

**Monometallic-Compound-Doped Carbon Electrocatalysts:** Monometallic compounds, including metal carbides,<sup>[90,91]</sup> oxides,<sup>[92,93]</sup> nitrides,<sup>[94]</sup> phosphides,<sup>[25,95–100]</sup> and chalcogenides,<sup>[101–103]</sup> can be directly synthesized from the pyrolysis of MOFs. Recently, by making use of the unique characteristics of highly and uniformly dispersed metal nodes and the suitable thermostability of MOFs, Deng et al. reported an efficient  $\text{Bi}_2\text{O}_3@\text{C}$  catalyst, which was prepared by an oxidation treatment after the carbonization of Bi-based MOFs.<sup>[93]</sup>



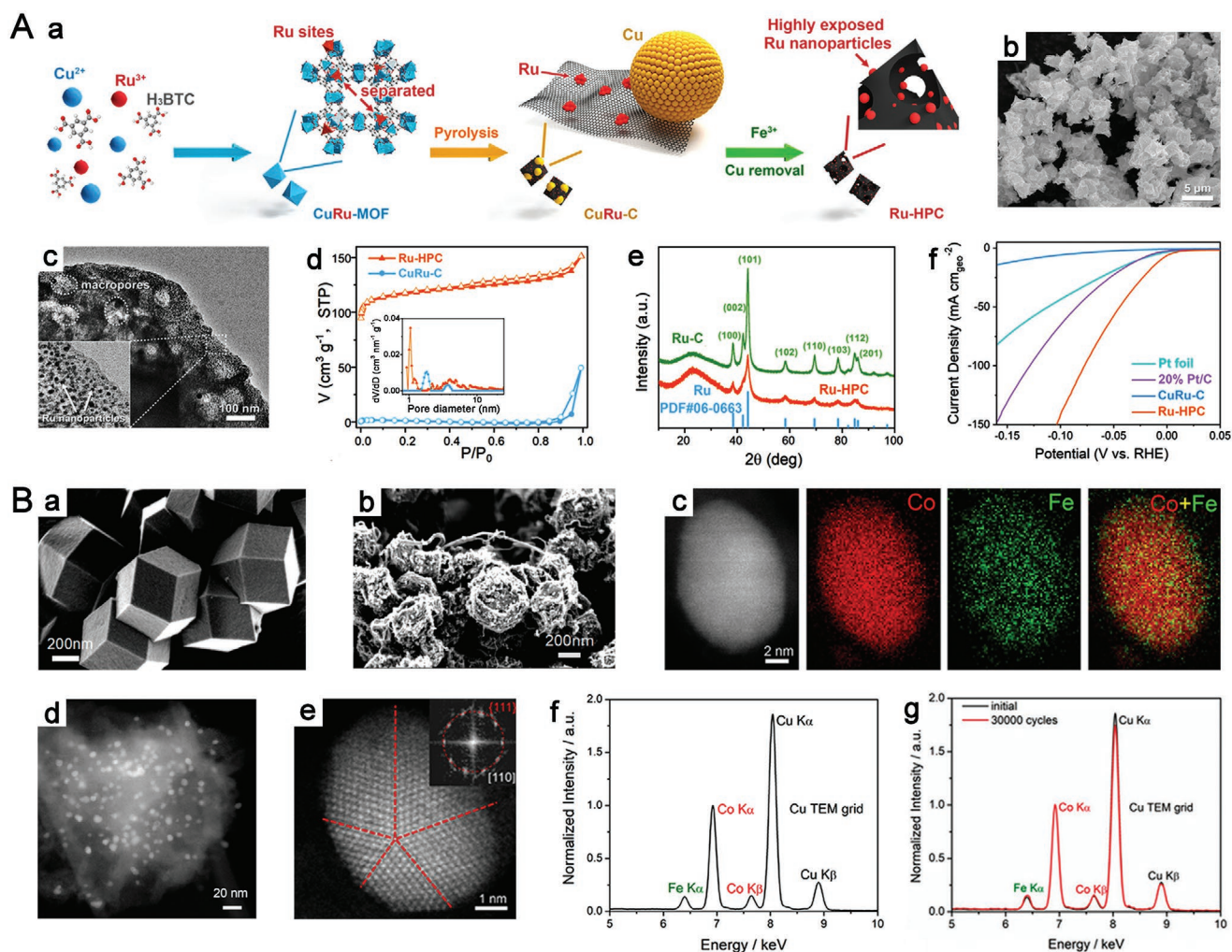


**Figure 5.** A) a) Schematic diagram of the approach to form Ru-HPC. b) SEM and c) TEM images of the Ru-HPC. Inset: ultrafine Ru nanoparticles. d) The  $N_2$  adsorption/desorption isotherms of Ru-HPC and CuRu-C. Inset shows the corresponding pore size distributions for Ru-HPC and CuRu-C. e) XRD patterns of Ru-HPC and Ru-C. f) HER polarization curves of the catalysts in 1 M KOH solution. A) Reproduced with permission.<sup>[70]</sup> Copyright 2019, Elsevier Ltd. B) a,b) SEM images of pyrolyzed BMOF\_Zn<sub>6</sub>Co (a) and Zn<sub>6</sub>Co\_Fe (b). c) STEM image and the corresponding EELS elemental maps of Co (red), Fe (green), and the composite map (Co vs Fe). d) Low-magnification STEM image of BMOF. e) Atomic-scale STEM image of a Co<sub>0.9</sub>Fe<sub>0.1</sub> nanoparticle with five subregions on the [110] zone axis. Inset: the corresponding Fourier transform with five pairs of {111} diffraction spots. f) STEM-EDX spectrum with Fe K $\alpha$  and Co K $\alpha,\beta$  edges. g) EDX patterns of BMOF before and after 30 000 cycles. B) Reproduced with permission.<sup>[86]</sup> Copyright 2019, American Chemical Society.

In addition to the optimal pyrolysis time and temperature, suitable ligands play a critical role in forming metal compounds. For example, Cu<sub>3</sub>P/CNS composites were directly prepared by annealing the MOPF, whose ligand contained the P atom.<sup>[98]</sup> However, additional heteroatom-containing sources are usually necessary to prepare metal phosphides, nitrides, and chalcogenides. Kang et al. fabricated 3D and mesoporous Co<sub>3</sub>N@AN-C nanocubes (NCs) using in situ nitridation and calcination processes under an N<sub>2</sub> (200 sccm)/NH<sub>3</sub> (10–100 sccm) atmosphere via a Prussian blue analog (PBA) of Co<sub>3</sub>[Co(CN)<sub>6</sub>]<sub>2</sub> NC precursors (Figure 6Aa,b).<sup>[94]</sup> The TEM images (Figure 6Ac,d) and X-ray photoelectron spectroscopy (XPS) profiles (Figure 6Ae) illustrate the successful formation of mesoporous Co<sub>3</sub>N@AN-C NCs, which demonstrate excellent OER activity (Figure 6Af).

By pyrolyzing the MOFs with external precursors to provide metal ions, a carbon matrix with encapsulated metal compound

particles can be synthesized. Lou et al. reported the facile synthesis of biphasic carbide nanocrystals composed of MC and M<sub>2</sub>C (M = Mo or W) confined in porous N-doped carbon dodecahedrons (PNCs) by annealing functional ZIF-8 containing molybdate or tungstate, as illustrated in Figure 6Ba.<sup>[90]</sup> The TEM images (Figure 6Bb,c) and XRD pattern (Figure 6Bd) show the presence of ultrafine nanocrystals for MoC-Mo<sub>2</sub>C. Furthermore, the strong coupling interactions between MC and M<sub>2</sub>C afford favorable sites for both water dissociation and hydrogen desorption, which endows dual-phased carbide nanocrystals with much better catalytic activity than that of the single-phase MC or M<sub>2</sub>C (Figure 6Be–g).

*Multiple-Metal-Compound-Doped Carbon Electrocatalysts:* MOF-derived bimetallic compounds may exhibit superior catalytic activities compared to their monometallic counterparts due to the strong synergistic effects that overcome the sluggish



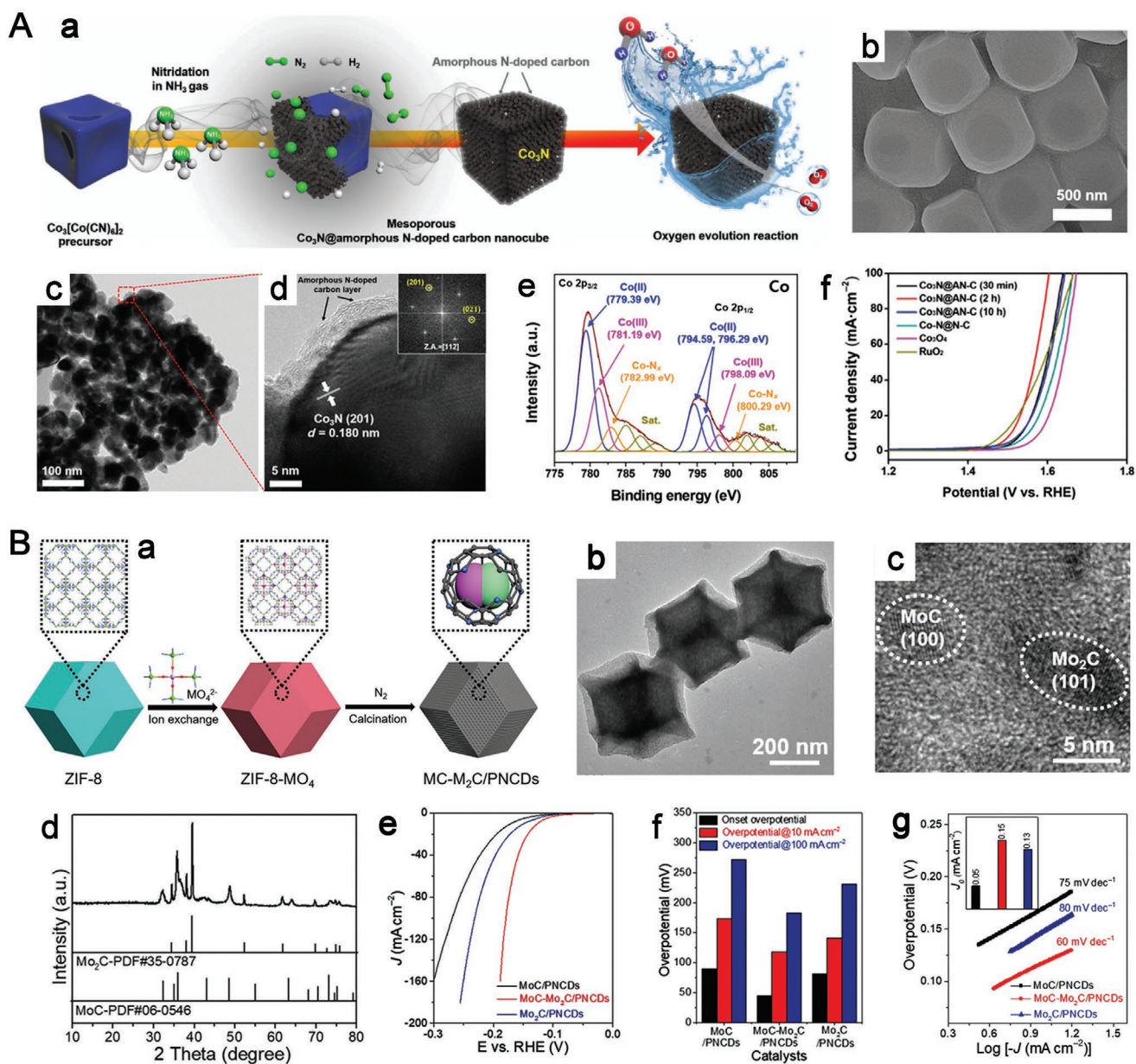


**Figure 6.** A) a) Schematic diagram of the synthesis process for  $\text{Co}_3\text{N}@AN\text{-C}$  NCs. b) SEM images of  $\text{Co}_3[\text{Co}(\text{CN})_6]_2$  PBA. c) Normal- and d) high-magnification TEM images of  $\text{Co}_3\text{N}@AN\text{-C}$  NCs (inset image is the fast Fourier transform patterns). e) Co 2p XPS profiles of the  $\text{Co}_3\text{N}@AN\text{-C}$  NCs. f) IR-corrected OER LSV recorded in 1 M KOH solution. A) Reproduced with permission.<sup>[94]</sup> Copyright 2019, Tsinghua University Press/Springer Nature. B) a) Schematic illustration of the  $\text{MoC-Mo}_2\text{C}/\text{PNCs}$ . b) TEM and c) HRTEM images of  $\text{MoC-Mo}_2\text{C}/\text{PNCs}$ . d) XRD patterns of  $\text{MoC-Mo}_2\text{C}/\text{PNCs}$ . e) LSV curves. f) Comparison of onset overpotential and the overpotentials at 10 and 100  $\text{mA cm}^{-2}$ , and g) Tafel slopes of  $\text{MoC}/\text{PNCs}$ ,  $\text{MoC-Mo}_2\text{C}/\text{PNCs}$ , and  $\text{Mo}_2\text{C}/\text{PNCs}$  (insets: histograms of exchange current density). B) Reproduced with permission.<sup>[90]</sup> Copyright 2019, Wiley-VCH.

kinetics of multiple electron transfer processes. Directly annealing bimetallic MOF precursors is a common approach to prepare bimetallic compounds.<sup>[104–109]</sup> Lou et al. designed Ni-doped FeP/C hollow nanorods with Ni–Fe bimetallic MIL-88A as the template and phytic acid as the etching agent and phosphorus source.<sup>[105]</sup> The optimized hollow nanorods obtained via the pyrolysis process exhibited pH-universal HER activity. XPS and DFT calculations attributed the efficiency to the synergistic modulation of the active components and the structural and electronic properties. Recently, Ouyang et al.

employed CoMo-MOF as the precursor to synthesize a magnetically functionalized  $\text{Co}_2\text{Mo}_3\text{O}_8@\text{NC-800}$  consisting of highly crystallized  $\text{Co}_2\text{Mo}_3\text{O}_8$  and ultrathin N-rich carbon via an NaCl-assisted pyrolysis strategy (Figure 7Aa).<sup>[109]</sup> According to the XRD results,  $\text{Co}_2\text{Mo}_3\text{O}_8@\text{NC-800}$  presents a hexagonal crystal structure with the space group  $\text{P6}_3\text{mc}$  (Figure 7Ab). The successful formation of  $\text{Co}_2\text{Mo}_3\text{O}_8$  with high crystallinity was confirmed by atomic-scale STEM (Figure 7Ac,d). Besides, the magnetic and theoretical calculation results reveal that  $\text{Co}_2\text{Mo}_3\text{O}_8$  with  $T_d$   $\text{Co}^{2+}$  (high spin,  $t_2^3e^4$ ) atoms as

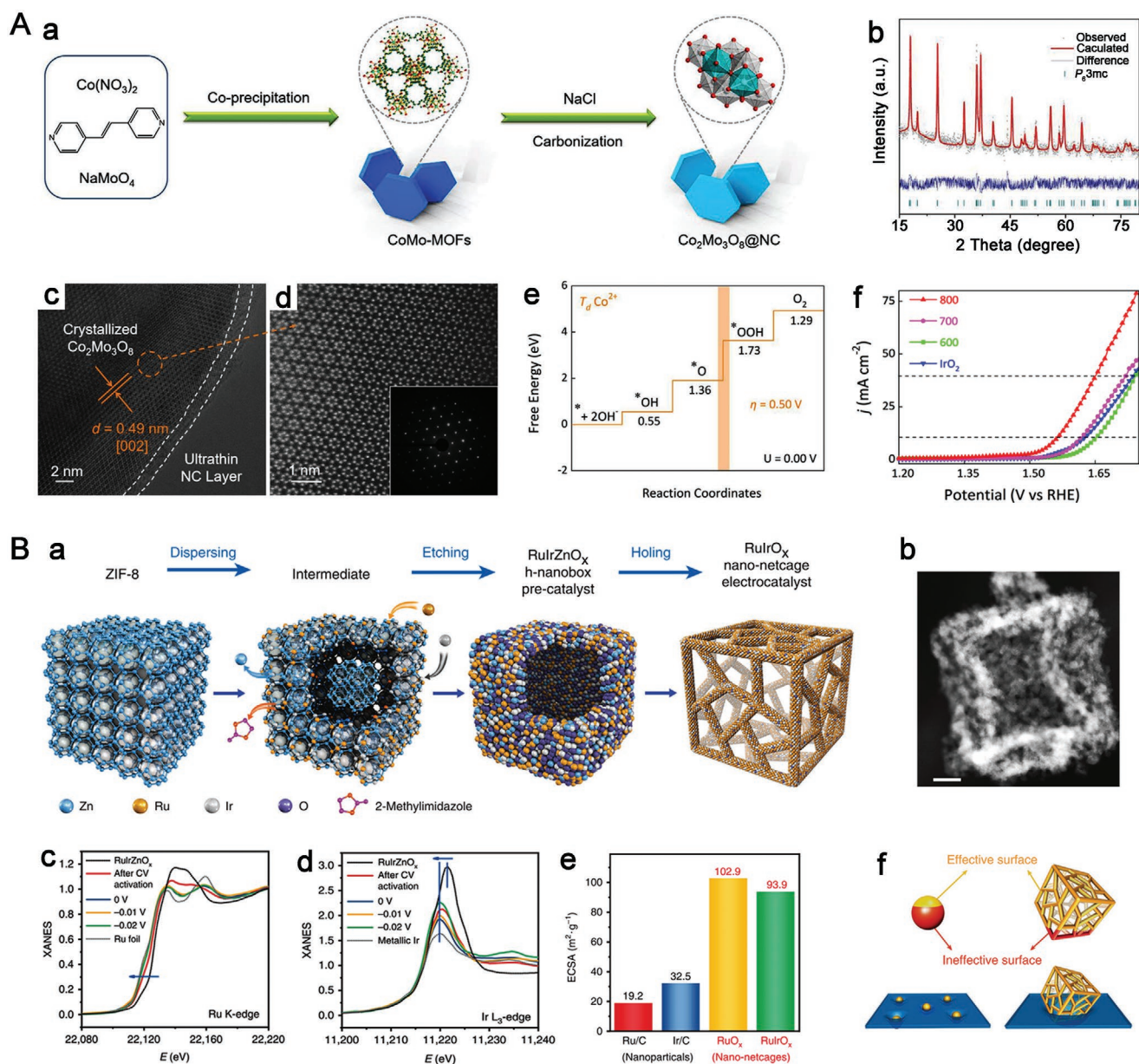


**Figure 7.** A) a) Illustration of fabricated  $\text{Co}_2\text{Mo}_3\text{O}_8@\text{NC}$ . b) Refined XRD profile of  $\text{Co}_2\text{Mo}_3\text{O}_8@\text{NC}$ -800. c, d) HAADF-STEM images of  $\text{Co}_2\text{Mo}_3\text{O}_8@\text{NC}$ -800. Inset of (d): corresponding FFT pattern for  $\text{Co}_2\text{Mo}_3\text{O}_8$ . e) Computed free energy diagram of  $\text{Co}_2\text{Mo}_3\text{O}_8$  with  $T_d \text{Co}^{2+}$  as the active adsorption sites at  $U = 0.00 \text{ V}$ . f) LSV curves in  $1.0 \text{ M KOH}$ . A) Reproduced with permission.<sup>[109]</sup> Copyright 2020, Wiley-VCH. B) a) Schematic representation of the preparation process and b) aberration-corrected HAADF-STEM image for  $\text{RuIrO}_x$  nanonet-cages. Scale bar: 10 nm. c) Normalized Ru K-edge and d) Ir  $L_3$ -edge XANES spectra of  $\text{RuIrO}_x$  were measured at different electrode potentials during the HER process in an alkaline medium. e) ECSA of different catalysts. f) Comparison of the ratios of an effective surface between the loaded nanoparticle and the 3D open nanonet-cage structures. B) Reproduced under the terms of the CC-BY Creative Commons Attribution 4.0 International License (<https://creativecommons.org/licenses/by/4.0>).<sup>[114]</sup> Copyright 2019, The Authors, published by Springer Nature.

the active sites are beneficial to the rate-determining step to form  $^*\text{OOH}$ , consequently enhancing the OER performance (Figure 7Ae,f).

A solvothermal reaction is a facile synthesis strategy for introducing metal ions into the precursor, which is further converted to multimetallic, compound-doped carbons through a post-annealing process.<sup>[26,110–115]</sup> Li et al. reported a novel dispersing-etching-holing (DEH) approach to fabricate the 3D open nanonet-cage electrocatalyst (Figure 7Ba,b).<sup>[114]</sup> The

operando XAS results confirmed that ZnO could be etched in situ during the HER process, while the provided RuIr alloy acted as the active sites (Figure 7Bc,d). The DEH method might significantly enhance the electrochemically active surface area (ECSA) by providing a porous nanocage with a large number of exposed active sites and the 3D availability of substrate molecules, as shown in Figure 7Be,f. Recently, Guo et al. reported a new strongly coupled NiCoN/C hybrid nanocage.<sup>[115]</sup> First, ZIF-67 and  $\text{Ni}(\text{NO}_3)_2$  were used to synthesize NiCo LDH



nanoboxes via a chemical etching method under sonication. Then, the nanoboxes were chemically converted into strongly coupled NiCoN/C hybrid nanocages by a low-temperature thermal ammonolysis treatment. The mass activity of the catalyst in the 1.0 M KOH electrolyte was 0.204 mA  $\mu\text{g}^{-1}$  at an overpotential of 200 mV.

Furthermore, through the pyrolysis of MOF precursors, complex metal compounds with multiple nanostructures and compositions can be obtained.<sup>[116–122]</sup> Liang et al. synthesized bifunctional Co-NC@Mo<sub>2</sub>C complex catalysts that showed excellent catalytic performance for overall water splitting with a low cell voltage of 1.685 V at 10 mA  $\text{cm}^{-2}$ .<sup>[119]</sup> The superior HER and OER performance could be ascribed to the synergistic effects of Mo<sub>2</sub>C and Co-NC. Remarkably, the coating structure of Mo<sub>2</sub>C not only protects the electrolyte erosion of Co nanoparticles but also provides more catalytic sites. A recently reported Ru-modified Co-based electrocatalyst, which was anchored in an N-doped carbon (NC) matrix and presented a rationally designed Mott–Schottky heterostructure (RuO<sub>2</sub>/Co<sub>3</sub>O<sub>4</sub>-RuCo@NC), achieved outstanding activity and stability for overall water splitting under strongly acidic conditions.<sup>[121]</sup> RuO<sub>2</sub>/Co<sub>3</sub>O<sub>4</sub>-RuCo@NC was synthesized via a three-step process: pyrolysis of Co-MOF, galvanic replacement reaction between Co and Ru, and controlled partial oxidation. Notably, the composite with rich metal–semiconductor interfaces obtained by partial oxidation could promote the charge-transfer process; thus, the catalytic performance would be further improved.

In brief, for the design of MOF-derived metal-based electrocatalysts, choosing the appropriate MOF precursors is a commonly adopted strategy. For instance, directly annealing bimetallic MOF precursors is a common approach to prepare bimetallic compounds. The advantages of this strategy are that it is simple to adjust the proportion of the metal elements, and the resulting catalysts can be evenly dispersed on the carbon substrates, resulting in excellent catalytic performance. Manipulating the conversion conditions and the introduction of additional precursors can also be employed to regulate the chemical composition of MOF-derived metal-based electrocatalysts. This strategy is applied widely, but it is difficult to adjust the ratio of the components accurately. Indeed, these strategies are used simultaneously in many cases to obtain excellent electrocatalytic activity and stability.

#### 2.2.4. Metal-Based Single-Atom Catalysts

With high catalytic activity, selectivity, and maximum metal atom utilization efficiency, single-atom catalysts (SACs) have drawn considerable attention in the field of catalysis. However, under realistic reaction conditions, the isolated atoms can easily migrate and aggregate into nanoparticles, owing to the high surface energy of the monatomic catalysts. To overcome this problem, MOFs have become promising precursors to develop SACs owing to their porous structures and precisely designable components. The direct pyrolysis of MOFs is a facile strategy to synthesize SACs.<sup>[123,124]</sup> Recently, other strategies have also been reported.

MOF-derived N-doped carbon is an effective scaffold for the adsorption of metal ions and the subsequent formation of

SACs via thermal treatment.<sup>[125,126]</sup> Li et al. developed a simple method to create atomic-dispersed Fe–N<sub>4</sub> active sites embedded into carbon phases, which are synthesized by the carbonization of ZIF-8 precursors (Figure 8a).<sup>[125]</sup> Benefiting from this method, researchers can fine-tune the Fe–N<sub>4</sub> site structure and density while maintaining the carbon matrix and N doping. Upon pyrolysis and etching, SACs can be obtained using bimetallic MOFs as the precursor.<sup>[127–130]</sup> For a facile adsorption strategy, engineering the structure and composition of the carbon substrates is typically recognized as the focus of future research.

A single-atom Ni electrocatalyst was designed using bimetallic MgNi-MOF-74 as a precursor (Figure 8b).<sup>[127]</sup> It is worth noting that the spatial distance of adjacent Ni atoms can be extended by introducing Mg<sup>2+</sup> ions into MgNi-MOF-74. The N coordination numbers of single-atom Ni catalysts could be adjusted and controlled by regulating the pyrolysis temperature. The pyrolysis-etching strategy is regarded as one of the most facile strategies. However, low metal loading resulting from the activation process and a limited number of precursors are the disadvantages of the strategy.

Another commonly used strategy for synthesizing SACs is the MOF-assisted host–guest strategy.<sup>[27,131–139]</sup> Typically, the extra metal precursor was encapsulated in the cavity or skeleton of the MOF, and the pyrolysis process was performed to obtain the SACs. Recently, Xiong et al. reported single-atom dispersed Rh embedded on N-doped carbon (SA-Rh/CN) with favorable electrocatalytic performance. ZIF-8 with molecular-scale cavities was used as a precursor for the substrate to disperse and anchor Rh(acac)<sub>3</sub> because the size of Rh(acac)<sub>3</sub> (9.36 Å) is between that of the large holes (diameter of 11.6 Å) and small pores (diameter of 3.4 Å) of ZIF-8. Thus, Rh(acac)<sub>3</sub> could be immobilized within the molecular cages of ZIF-8 (denoted Rh/ZIF-8), which was reduced in situ to synthesize SA-Rh/CN by pyrolysis (Figure 8c). The spatial distribution and structure of the Rh species were elucidated by AC HAADF-STEM images and XAFS spectroscopy (Figure 8d–f). The host–guest strategy could effectively restrain the migration of the metal species during calcination. Nevertheless, mononuclear, metal-based guests with appropriate sizes below those of the MOF pores should be considered.

Recently, Fan et al. synthesized Ni-based SACs (A-Ni-C) with graphitized carbon materials.<sup>[140]</sup> The A-Ni-C was produced by the carbonization of a Ni-MOF, followed by HCl etching and electrochemical activation (Figure 9Aa). The presence of single Ni atoms was elucidated by HAADF STEM imaging and XRD (Figure 9Ab,c). The A-Ni-C electrocatalysts exhibited significantly improved HER performance after electrochemical activation, which could remove the Ni nanoparticles protected by graphitic carbons and create single-atom Ni sites (Figure 9Ad). Moreover, the host is crucial to the design of SACs because it influences the space and electronic environment of the metal center.<sup>[141]</sup>

Besides the carbon frameworks, a variety of metal crystals doped with single-metal sites have also been identified as promising SACs for electrochemical water splitting.<sup>[142,143]</sup> Recently, Lou et al. reported a series of metal-atom-doped Co<sub>3</sub>O<sub>4</sub> nanosheets for efficient OER using MOF precursors.<sup>[143]</sup> These novel electrocatalysts were fabricated by a cooperative etching-coordination-reorganization approach with ZIF-67 nanoplates.



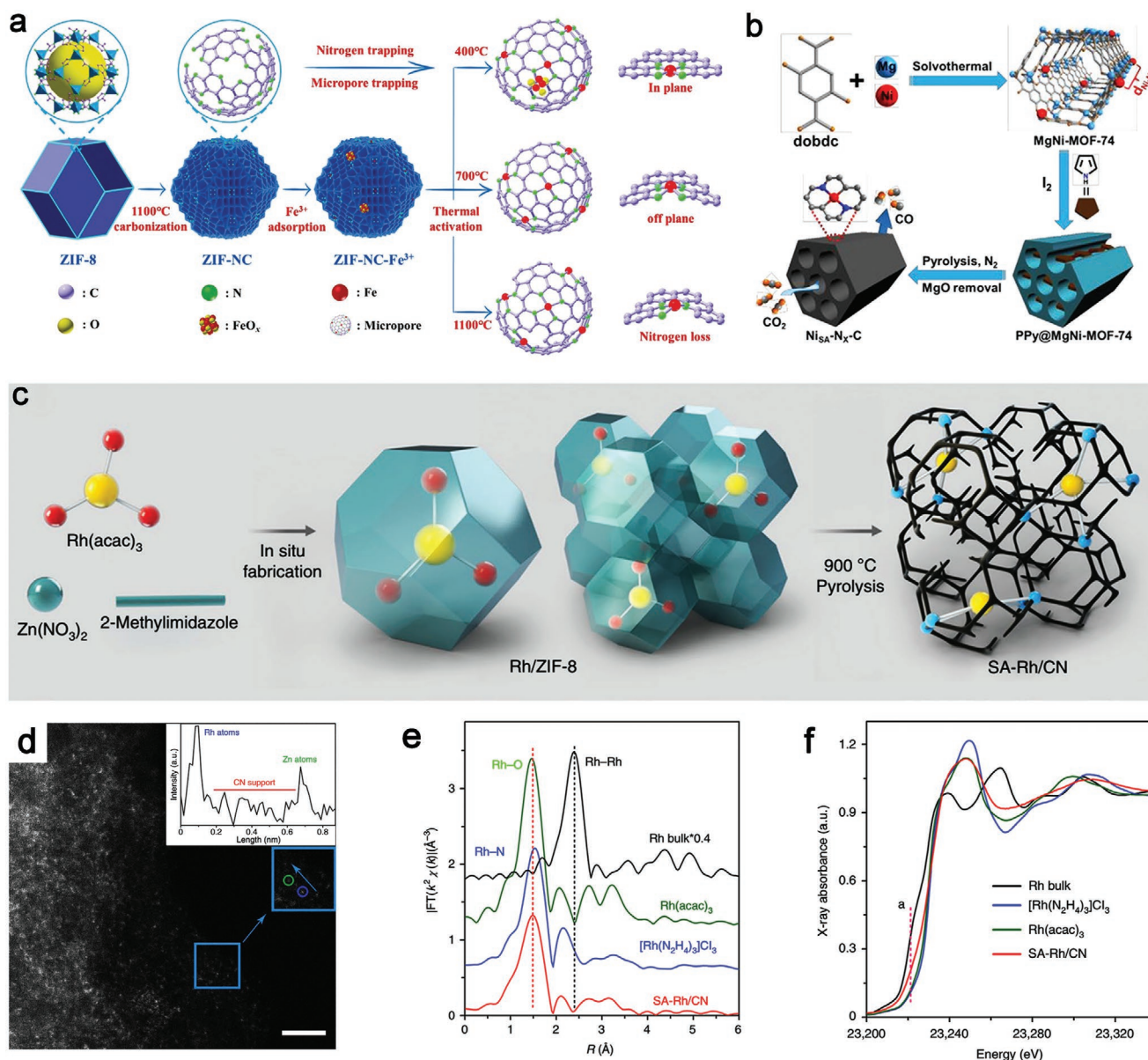


**Figure 8.** a) Schematic diagram of the model systems constructed by adsorbing Fe onto N-doped carbon. b) Diagram illustrating the fabrication of  $\text{Ni}_{\text{SA}}\text{-N}_x\text{-C}$  catalysts. c) Schematic image illustrating the synthesis of SA-Rh/CN. d) AC-HAADF-STEM image and corresponding Z-contrast analysis. e) FT-EXAFS spectra of SA-Rh/CN and reference samples. f) Experimental Rh K-edge XANES spectra of SA-Rh/CN and reference samples. a) Reproduced with permission.<sup>[125]</sup> Copyright 2019, Wiley-VCH. b) Reproduced with permission.<sup>[127]</sup> Copyright 2019, Wiley-VCH. c–f) Reproduced with permission.<sup>[138]</sup> Copyright 2020, The Authors, published by Springer Nature.

Remarkably, the Fe-doped  $\text{Co}_3\text{O}_4$  nanosheets exhibited superior OER activity with an overpotential of 262 mV at  $10 \text{ mA cm}^{-2}$ , which is comparable to that of commercialized noble-metal OER catalysts.

Significant progress has been achieved toward the design of SACs for electrochemical catalysis, as summarized in **Table 1**, including SACs from MOF precursors. However, a relatively limited number of these MOF-derived SACs have been applied to electrochemical water splitting, especially in OER catalysis. Because of the advantages afforded by the use of SACs for scalable production and electrochemical reactions, we believe that much more effort is needed to enhance further the current intrinsic

catalytic activities of MOF-derived SACs in both the HER and OER. For instance, DFT calculations have been extensively used to investigate the coordination environment of catalysts and reaction mechanisms and to analyze and design the active sites for electrochemical reactions. Mohajeri et al. investigated a single transition metal from 3d atoms (TM/ $\text{B}_{36}$ , TM = Sc–Zn) with finite-sized B clusters,  $\text{B}_{36}$ , as the substrate.<sup>[144]</sup> Among the mentioned catalysts, Ni/ $\text{B}_{36}$  was recognized as the most efficient OER electrocatalyst, which could be attributed to the appropriate binding strengths of various adsorbates (Figure 9Ba,b). The Ti/ $\text{B}_{36}$  electrode showed the highest activity for the HER electrocatalyst owing to the lowest  $\Delta G_{\text{H}}$  (0.12 eV) (Figure 9Bc).

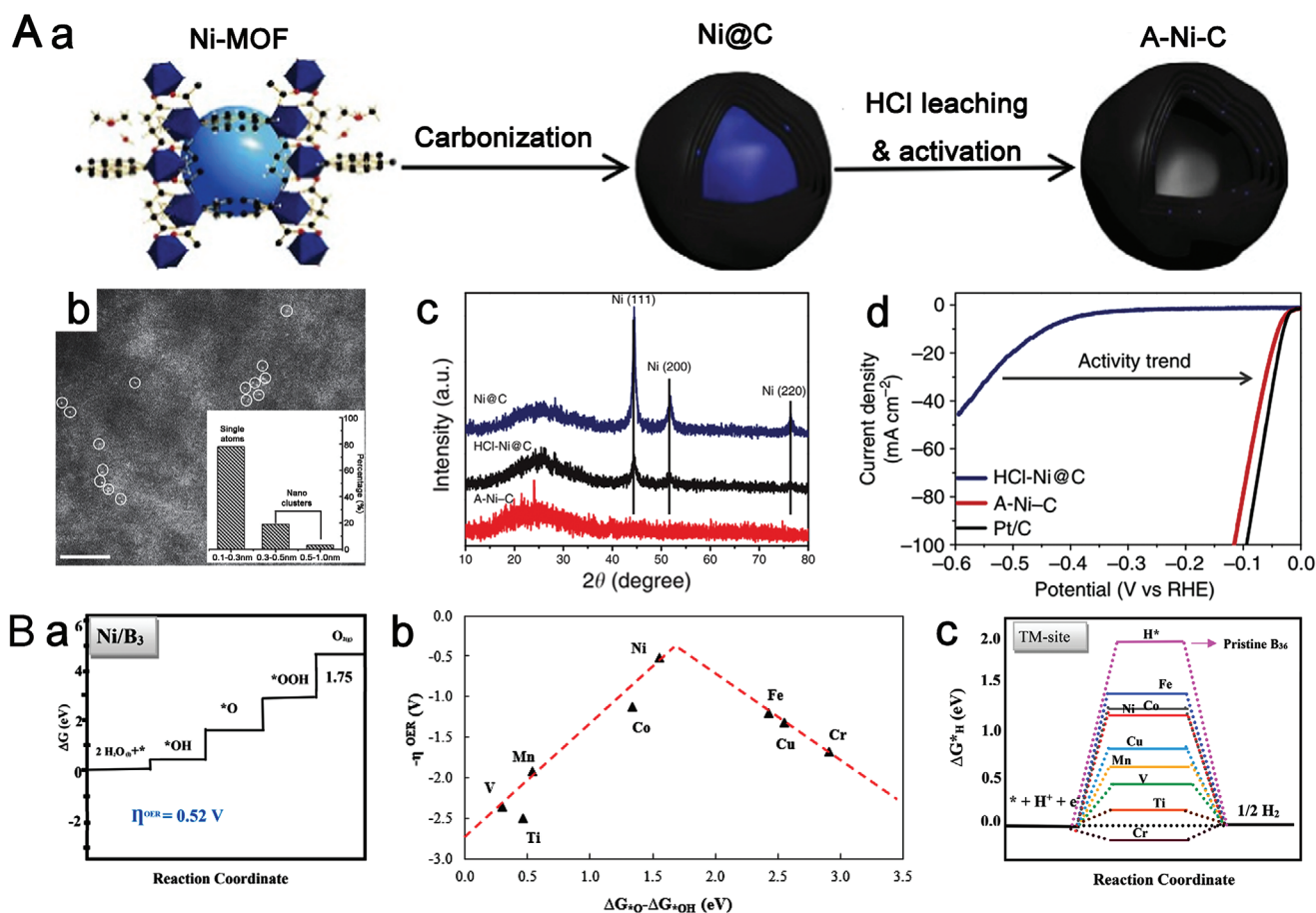


**Figure 9.** A) a) Schematic image illustrating the synthetic route of A-Ni-C. b) HAADF-STEM image of A-Ni-C. c) XRD patterns and d) LSV curves of A-Ni-C and reference samples. A) Reproduced under the terms of the CC-BY Creative Commons Attribution 4.0 International License (<https://creativecommons.org/licenses/by/4.0/>).<sup>[140]</sup> Copyright 2016, The Authors, published by Springer Nature. B) a) Reaction-free energy profile for the OER of Ni/B<sub>36</sub>. b) Activity trends for the OER. c) Free energy profile for the HER at TM-sites of TM/B<sub>36</sub> systems. B) Reproduced with permission.<sup>[144]</sup> Copyright 2019, American Chemical Society.

In brief, we put forward a summarization of the composition and structural design of MOF-derived carbon-based electrocatalysts. MOF-derived carbon materials with heteroatomic dopants (e.g., B, N, P, S, etc.) have drawn increasing attention because of their high conductivity, erosion resistance, and excellent catalytic performance. The improvement of the electrocatalysis behavior is due to charge accumulation and spin polarization caused by heteroatom doping. We believe that carbon substrates with nonmetallic heteroatomic dopants can be considered when designing the MOF-derived electrocatalysts. For metal-based-material-doped carbons derived from MOFs for electrochemical water splitting, more attention should be paid to the chemical and structural composition in the design process. For instance, more Mo- and W-based materials have been widely used to catalyze HER.

Besides the metal oxides and hydroxides commonly employed as OER catalysts, other types of metal compounds (e.g., phosphides, nitrides, and chalcogenides) exhibit outstanding HER performance. A limited number of studies on MOF-derived SACs for electrochemical water splitting have been reported. When the adsorption–calcination method is applied to the design of SACs, the calcination temperature should be carefully considered. The host–guest strategy is

usually employed for the synthesis of MOF-derived SACs, and the regulation of pore size and guest matching has a substantial effect on the successful preparation of SACs. The SACs can also be obtained using bimetallic MOFs as the precursor through a pyrolysis-etching strategy, which is relatively simple but is limited by the formation of a bimetallic MOF precursor.

Furthermore, to control the chemical composition of MOF derivatives, choosing appropriate MOF precursors is a commonly adopted strategy. Manipulating the conversion conditions and introducing additional precursors can also be employed to regulate the chemical composition of the electrocatalysts. Indeed, these strategies are used simultaneously in many cases to obtain excellent electrocatalytic activity and stability.

### 3. Recent Advancements of MOF-Based/Derived Electrocatalysts for Water Splitting

#### 3.1. Catalysts for the Hydrogen Evolution Reaction

Hydrogen is a promising green energy source as a substitute for traditional fossil fuel energy. The HER is a key half-reaction



**Table 1.** Summary of the synthesized MOF precursors and metal catalytic centers of currently reported MOF-derived SACs.

Metal element	MOFs	Metal centers	Metal content	Ref.
Fe	Cd-MOF	Fe-N <sub>4</sub>		[27]
Mn	Mn-BTC	Mn-N <sub>3</sub> O <sub>1</sub>		[123]
Bi	Bi-MOF	Bi-N <sub>4</sub>		[124]
Fe	ZIF-8	Fe-N <sub>4</sub>	1.12 wt%	[125]
Ni	ZIF-8	Ni-N <sub>x</sub> -C		[126]
Ni	PPy@MgNi-MOF-74	NiSA-N <sub>2</sub> -C	0.90 wt%	[127]
Co	ZnCo-ZIFs	Co-N <sub>x</sub>	1.70 wt%	[128]
Co	Bimetallic Zn/Co ZIF	Co-N <sub>2</sub>	0.25 wt%	[129]
Fe	Fe <sub>20</sub> -PCN-222	Fe-N <sub>x</sub>	1.76 wt%	[130]
Ru	ZIF-8	Ru-N	0.18 wt%	[131]
W	UiO-66-NH <sub>2</sub> @WCl <sub>6</sub>	W <sub>1</sub> -N <sub>1</sub> -C <sub>3</sub>	1.21 wt%	[132]
Ru	UiO-66	Ru@Zr <sub>32</sub> O <sub>63</sub> and Ru/NC <sub>2</sub>	0.10 wt%	[133]
Fe, Co	FeCo-ZIF-8	Fe-N <sub>4</sub> , Co-N <sub>4</sub>	0.26 wt% (Fe), 1.06 wt% (Co)	[135]
Ru	ZIF-8	Ru-N <sub>4</sub>	0.42 wt%	[136]
Fe	Fe/ZIF-8@SiO <sub>x</sub>	Fe-N <sub>x</sub>	0.11 wt%	[137]
Rh	ZIF-8	Rh-N <sub>4</sub>	0.92 wt%	[138]
Ir, Rh, Pt, Pd	ZIF-8	PM-N <sub>4</sub> (PM = Ir, Rh, Pd, Pt)	1.20–4.50 wt%	[139]
Ni	Ni-MOF	Ni-N-C	1.5 wt%	[140]
Mn, Fe, Co, Ni, Cu	ZIF-8	M-N <sub>x</sub> (M = Mn, Fe, Co, Ni, and Cu)		[145]
Co	ZIF-8	Co-N <sub>4</sub>	0.70 wt%	[146]

of electrochemical water splitting, which is an efficient strategy for converting electricity into storable hydrogen. The HER reaction proceeds as follows



The evaluation parameters for the HER include the onset potential, the value of the potential at a current density of 10 mA cm<sup>-2</sup> (the overpotential  $\eta_{10}$ ), and the Tafel slope, among others. To concisely describe these concepts, the overpotential ( $\eta$ ) is a measurement of the additional potential needed above the thermodynamic potential ( $E_0$ ) required for an electrocatalytic reaction at a certain current density. The Tafel slope is a parameter of kinetic measurement, which describes the relationship between the overpotential and the base 10 logarithm of the current density. A lower Tafel slope reflects better HER kinetics. During the HER process, hydrogen intermediates (H\*) are adsorbed onto the catalytic sites, so the hydrogen adsorption energy is crucial for the sensible selection of active HER catalysts. According to the HER mechanism, the active site with an H\* adsorption free energy ( $\Delta G_{\text{H}^*}$ ) of 0 could achieve the best HER activity.<sup>[4,5]</sup>

MOFs have been extensively utilized as preferred heterogeneous catalysts for the HER because of their large surface area and controllable structure.<sup>[1,147,148]</sup> In particular, the conductive MOFs exhibit significantly more electron transfer than traditional MOFs. Generally, to improve the intrinsic electrical conductivity, one strategy is to synthesize a  $\pi$ -conjugated structure with transition metal atoms (Ni, Cu, and Co) and aromatic organic ligands (such as

1,3,5-triaminobenzene-2,4,6-trithiol, hexaaminobenzene, and benzenehexathiolate) as precursors.<sup>[17,149–152]</sup> Recently, hexaiminohexaazatrinaphthalene (HAHATN), an analog of hexaazatriphenylene (HATN), was fabricated as an organic ligand to prepare different bimetallic conductive MOFs with in-plane mesoporous structures (2.7 nm) (Figure 10Aa,b).<sup>[17]</sup> The obtained Ni<sub>3</sub>(Ni<sub>3</sub>·HAHAT)<sub>2</sub> bimetallic, conductive MOFs exhibited outstanding HER catalytic activity, achieving a rather low overpotential of 115 mV at 10 mA cm<sup>-2</sup> in an alkaline medium (Figure 10Ac). The DFT calculations suggest that the Ni-N<sub>2</sub> groups have a stronger ability to absorb and bond protons, which can remarkably enhance the HER performance of Ni<sub>3</sub>(Ni<sub>3</sub>·HAHATN)<sub>2</sub> compared to that of the traditional Ni<sub>3</sub>(HITP)<sub>2</sub> conductive MOF (Figure 10Ad–f).

Recent research has revealed that combining MOFs with functional materials is an effective strategy to synthesize MOF composites, which can not only overcome the deficiencies of traditional MOFs, such as poor conductivity and limited functionality but also inherit their strengths.<sup>[153]</sup> In addition, numerous investigations have demonstrated that 2D MOFs could be utilized as promising electrocatalytic materials because of their intrinsic advantages, such as fast mass and electron transfer, tunable structures, and more exposed active sites.<sup>[8,20]</sup> In one study, novel 2D Co-BDC/MoS<sub>2</sub> hybrid nanosheets (Figure 10Ba) were designed and fabricated as efficient electrocatalysts for alkaline HER via a simple sonication-assisted solution strategy.<sup>[154]</sup> As shown in Figure 10Bb, the introduction of Co-BDC in the Co-BDC/MoS<sub>2</sub> resulted in a partial phase transfer from 2H-MoS<sub>2</sub> to 1T-MoS<sub>2</sub>, which contributes significantly to enhanced HER activity. The Co-BDC/MoS<sub>2</sub> required a lower overpotential at -10 mA cm<sup>-2</sup>, lower Tafel slope, and lower charge-transfer resistance than bare

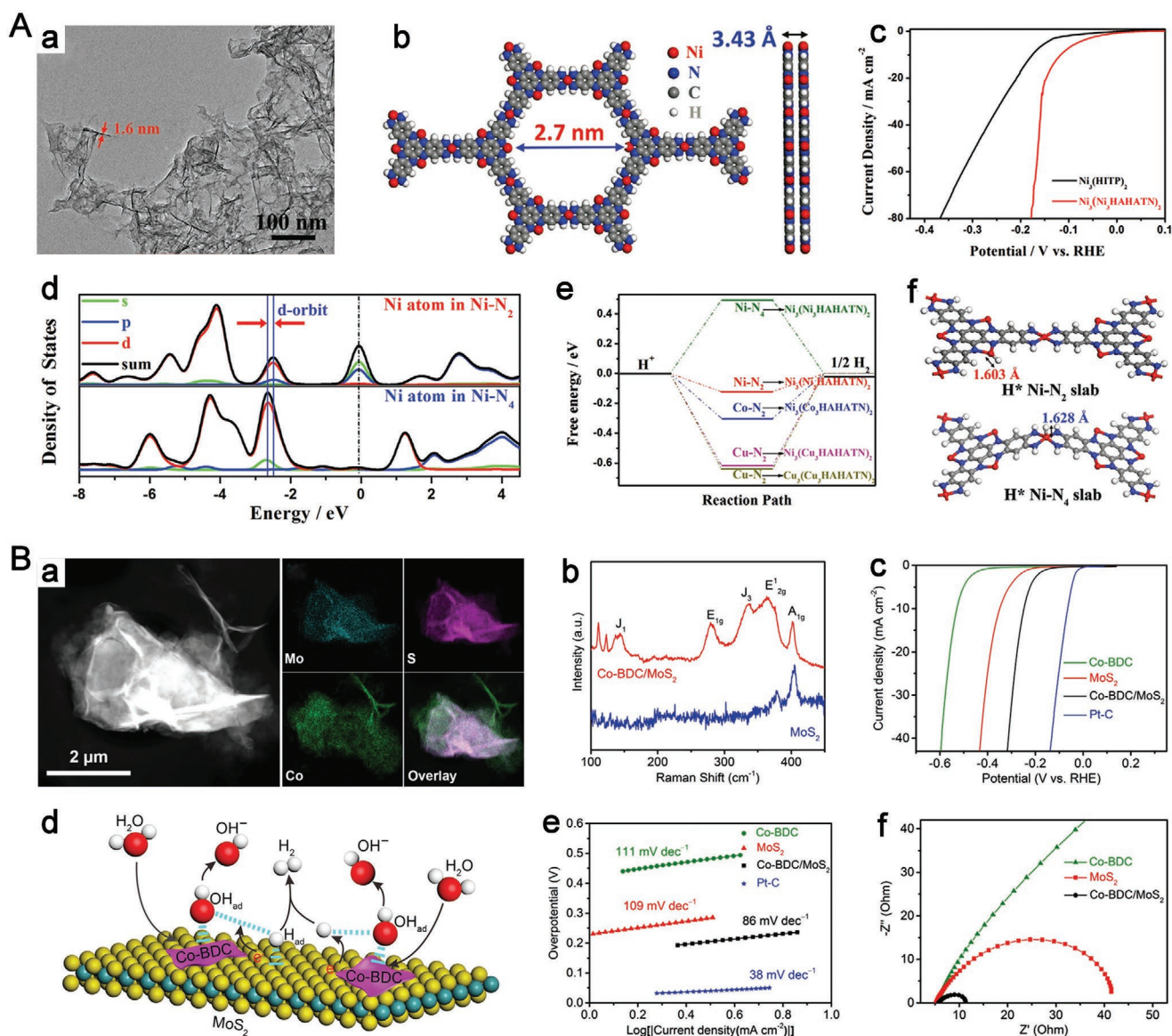


**Figure 10.** A) a) TEM image of  $\text{Ni}_3(\text{Ni}_3\text{-HAHATN})_2$  nanosheets. b) The optimization structure of the  $\text{Ni}_3(\text{Ni}_3\text{-HAHATN})_2$  slab. c) Polarization curves of the  $\text{Ni}_3(\text{HITP})_2$  and  $\text{Ni}_3(\text{Ni}_3\text{-HAHATN})_2$  samples toward the HER. d) PDOS of an Ni atom in  $\text{Ni-N}_2$  and  $\text{Ni-N}_4$  of the  $\text{Ni}_3(\text{Ni}_3\text{-HAHATN})_2$  slab. e) Free-energy diagrams for the HER at different catalytic sites. f) The  $\text{H}_2$  adsorption slabs of  $\text{Ni}_3(\text{Ni}_3\text{-HAHATN})_2$  at the  $\text{Ni-N}_2$  and  $\text{Ni-N}_4$  sites. B) a) HAADF-STEM image of  $\text{Co-BDC}/\text{MoS}_2$  hybrid nanosheets. b) Raman spectra of  $\text{MoS}_2$  and  $\text{Co-BDC}/\text{MoS}_2$ . c) HER LSV curves of  $\text{Co-BDC}$ ,  $\text{MoS}_2$ ,  $\text{Co-BDC}/\text{MoS}_2$ , and  $\text{Pt-C}$  in 1.0 M KOH. d) HER mechanism of the  $\text{Co-BDC}/\text{MoS}_2$  hybrid nanosheets in an alkaline electrolyte. e) Tafel plots and f) Nyquist plots of  $\text{Co-BDC}/\text{MoS}_2$  and corresponding counterparts. B) Reproduced with permission.<sup>[154]</sup> Copyright 2019, Wiley-VCH.

$\text{Co-BDC}$  and  $\text{MoS}_2$  in 1 M KOH (Figure 10Bc,e,f). More importantly, a well-designed  $\text{Co-BDC}/\text{MoS}_2$  interface is highly desirable for the alkaline HER. As shown in Figure 10Bd,  $\text{Co-BDC}$  facilitates the kinetics of the rate-determining water dissociation step of the alkaline HER, while modified  $\text{MoS}_2$  is beneficial for the subsequent  $\text{H}_2$ -generation step. The high conductivity of substrates such as CNTs and rGO can be used to support MOF particles and improve the mechanical stability of pristine MOFs.<sup>[8,18]</sup> Khalid et al. reported nanoflocks of a bimetallic organic framework ( $\text{NiCo-MOF}$ ), which was grown on a Ni mesh and covered with a graphene oxide aerosol skeleton by utilizing a nebulizer

air compressor.<sup>[18]</sup> The obtained composites showed enhanced electrocatalytic behavior for the HER and excellent stability in the alkaline electrolyte compared to the pristine nanoflocks. Moreover, coupling MOFs with conductive materials, such as acetylene black (AB), have been reported to enhance the HER catalytic properties efficiently.<sup>[19,155]</sup> For instance, Li et al. designed and fabricated a series of composites containing  $[\text{Co}_{1.5}(\text{TTAB})_{0.5}(4,4'\text{-bipy})(\text{H}_2\text{O})]$  (CTGU-9) and AB, which demonstrated a distinct electrocatalytic activity for the HER with an overpotential of 128 mV at 10 mA cm<sup>-2</sup>, a small Tafel slope of 87 mV dec<sup>-1</sup>, and excellent long-term stability of no less than 21 h.<sup>[19]</sup>



In situ synthesis of hybrid catalysts combining metal compounds and MOFs for the HER has been considered as an ideal strategy to enhance further the HER activity owing to the strong interaction of the MOF-based composites.<sup>[2,156]</sup> Recently, Liu et al. synthesized CoP-doped MOF-based electrocatalysts for the pH-universal HER via a controllable partial phosphorization strategy.<sup>[156]</sup> The CoP/Co-MOF hybrid also showed excellent electrocatalytic activity for the HER with overpotentials of 27, 49, and 34 mV at a current density of 10 mA cm<sup>-2</sup> in 0.5 M H<sub>2</sub>SO<sub>4</sub>, 1 M phosphate buffer solution (PBS, pH 7.0), and 1 M KOH, respectively. The results of DFT calculations and experiments show that the MOF-based HER electrocatalysts not only possess the optimal adsorption energy of H<sub>2</sub>O ( $\Delta G_{\text{H}_2\text{O}^*}$ ) and hydrogen ( $\Delta G_{\text{H}^*}$ ) but also take advantage of the well-defined channel structure of MOFs. Huang et al. introduced a facile in situ sulfurization strategy to synthesize a hybrid catalyst containing good conductive Fe<sub>3</sub>S<sub>4</sub> ultrasmall nanosheets attached on the surface of 3D MIL-53(Fe) for the HER under acidic solutions.<sup>[2]</sup> The Fe<sub>3</sub>S<sub>4</sub>/MIL-53(Fe) hybrid catalysts maintain the advantages and overcome the deficiencies of the individual components, which contributes to the remarkable HER performance.

Recently, transition metal compounds and composites derived from MOF precursors, featuring their well-defined structure and large surface area, have been applied as excellent electrocatalysts. With MOFs as precursors, Ni-based catalysts, such as Ni<sub>2</sub>P,<sup>[118,157,158]</sup> Ni/NiO,<sup>[159,160]</sup> NiSe,<sup>[161]</sup> and NiFeP,<sup>[105,162]</sup> have been widely used to catalyze the HER.<sup>[105,118,140,157–164]</sup> For instance, Jiao et al. designed and fabricated a Ni/NiO nanoparticle with subtle lattice distortions using Ni-MOF as the precursor and template.<sup>[160]</sup> Notably, the incorporation of Ni<sup>3+</sup> in Ni/NiO heterostructures led to a subtle atomic rearrangement and exposed more electrochemically active reaction sites, which promoted HER activity with a rather low overpotential of 41 mV at 10 mA cm<sup>-2</sup>. Recently, Lou et al. reported a simple method to prepare Ni-doped FeP/C hollow nanorods with adjustable aspect ratios by the etching and coordination reaction between MOFs and phytic acid followed by a pyrolysis process.<sup>[105]</sup> The obtained Ni-doped FeP/C hollow nanorods show outstanding electrocatalytic activity and robust stability in solutions for the HER over a full range of pH values because of their abundant active sites and the shortening of the diffusion distance for both mass and electron transport. The overpotential at 10 mA cm<sup>-2</sup> of the Ni-doped FeP/C hollow nanorods was only 72, 117, and 95 mV in acidic, neutral, and alkaline media, respectively. Moreover, the DFT-calculated electronic structures indicate that Ni doping can further improve charge transfer.

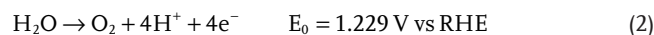
Co-based catalysts derived from MOFs, such as CoSe<sub>2</sub>,<sup>[165]</sup> CoP,<sup>[100,166]</sup> CoPS,<sup>[167]</sup> IrCo nanoalloys,<sup>[87]</sup> Co<sub>x</sub>Ni<sub>y</sub>N,<sup>[168]</sup> CoFeP,<sup>[107]</sup> and CoNiP,<sup>[169]</sup> have also been widely reported to facilitate the HER. Jiang et al. designed a one-step annealing strategy for Ir-doped MOFs to prepare IrCo nanoalloys coated with N-doped graphene shells (IrCo@NC) (Figure 11Aa,b).<sup>[87]</sup> The as-prepared IrCo@NC shows excellent catalytic activity for the HER with an exceedingly low Tafel slope of 23 mV dec<sup>-1</sup> and an overpotential of only 24 mV at a current density of 10 mA cm<sup>-2</sup> under acidic conditions (Figure 11Ac,d). The remarkable HER activity is even more outstanding than that of commercial Pt/C catalysts, which results from the significantly reduced  $\Delta G_{\text{H}^*}$

(Figure 11Ae). Feng et al. fabricated porous, rodlike Co–Ni bimetal nitrides (Co<sub>x</sub>Ni<sub>y</sub>N) as high-efficiency HER electrocatalysts in all pH environments through nitridation from a bimetallic MOF-74 precursor.<sup>[168]</sup> The obtained Co<sub>x</sub>Ni<sub>y</sub>N presents several advantages, such as large specific surface area, abundant mesoporous structure, and perfect active site dispersion, resulting in enhanced HER catalytic activity.

In recent years, MOF-derived SACs have been explored as promising electrocatalysts.<sup>[132,170,171]</sup> Chen et al. designed and synthesized a W-SAC, with W atoms immobilized on a N-doped carbon substrate derived from a MOF for HER applications.<sup>[132]</sup> WCl<sub>5</sub>/UiO-66-NH<sub>2</sub> was annealed at 950 °C and then treated with a hydrofluoric acid solution to etch the zirconic oxide (Figure 11Ba). HAADF-STEM and XAFS analyses reveal the uniform dispersion of the W atoms (Figure 11Bb,c). The W-SAC exhibited a small overpotential of 85 mV at 10 mA cm<sup>-2</sup> and a low Tafel slope of 53 mV dec<sup>-1</sup> in a 0.1 M KOH solution (Figure 11Bd,e). DFT calculations suggested that the  $\Delta G_{\text{H}^*}$  of the W-SAC approached the ideal value of zero, which is closely related to the HER activity of the catalyst (Figure 11Bf). Recently, Li et al. reported novel synthesis tactics utilizing an in situ phosphatizing of triphenylphosphine embedded within MOFs to obtain an atomic Co<sub>1</sub>-P<sub>1</sub>N<sub>3</sub> interfacial structure, where one single Co atom is coordinated with one P atom and three N atoms (denoted as Co-SA/P-in-situ).<sup>[170]</sup> In the acid solution, the as-prepared Co-SA/P-in-situ exhibited excellent HER activity with an overpotential of 98 mV at 10 mA cm<sup>-2</sup> and a Tafel slope of 47 mV dec<sup>-1</sup>, which are better values than those of the catalyst with the Co–N<sub>4</sub> interfacial structure. Moreover, in situ XAFS analysis and DFT calculations supported the explanation that the enhanced HER performance was ascribed to the bond-length-extended, high-valence Co<sub>1</sub>-P<sub>1</sub>N<sub>3</sub> atomic interface structure. The most recently reported MOF-based/derived electrocatalysts with different substrate that are favorable for the HER are systematically summarized in Table 2.

### 3.2. Catalysts for the Oxygen Evolution Reaction

The OER, with an equilibrium potential of 1.229 V versus RHE, is vital for several energy-related applications, including rechargeable metal–air batteries and water electrolysis.<sup>[174]</sup> The reaction equation for the OER is as follows



The parameters commonly utilized to assess the activity of OER electrocatalysts include the onset potential,  $\eta_{10}$ , and the Tafel slope, which resemble those of HER electrocatalysts. The OER is a complicated 4-electron process, in which the oxygen intermediates are adsorbed onto the active sites. In order to further optimize the durability of earth-abundant transition-metal-based OER catalysts, and to improve the kinetics, the OER is usually carried out under extremely alkaline environments (pH = 13 or 14). More details of the MOF-based/derived materials for OER electrocatalysis are discussed in the subsequent sections.

Recent studies have shown that Co-,<sup>[13,175,176]</sup> Mn-,<sup>[177]</sup> Ni-,<sup>[178,179]</sup> and Fe-based MOFs<sup>[180,181]</sup> with enhanced electrocatalytic activity have been widely investigated as novel

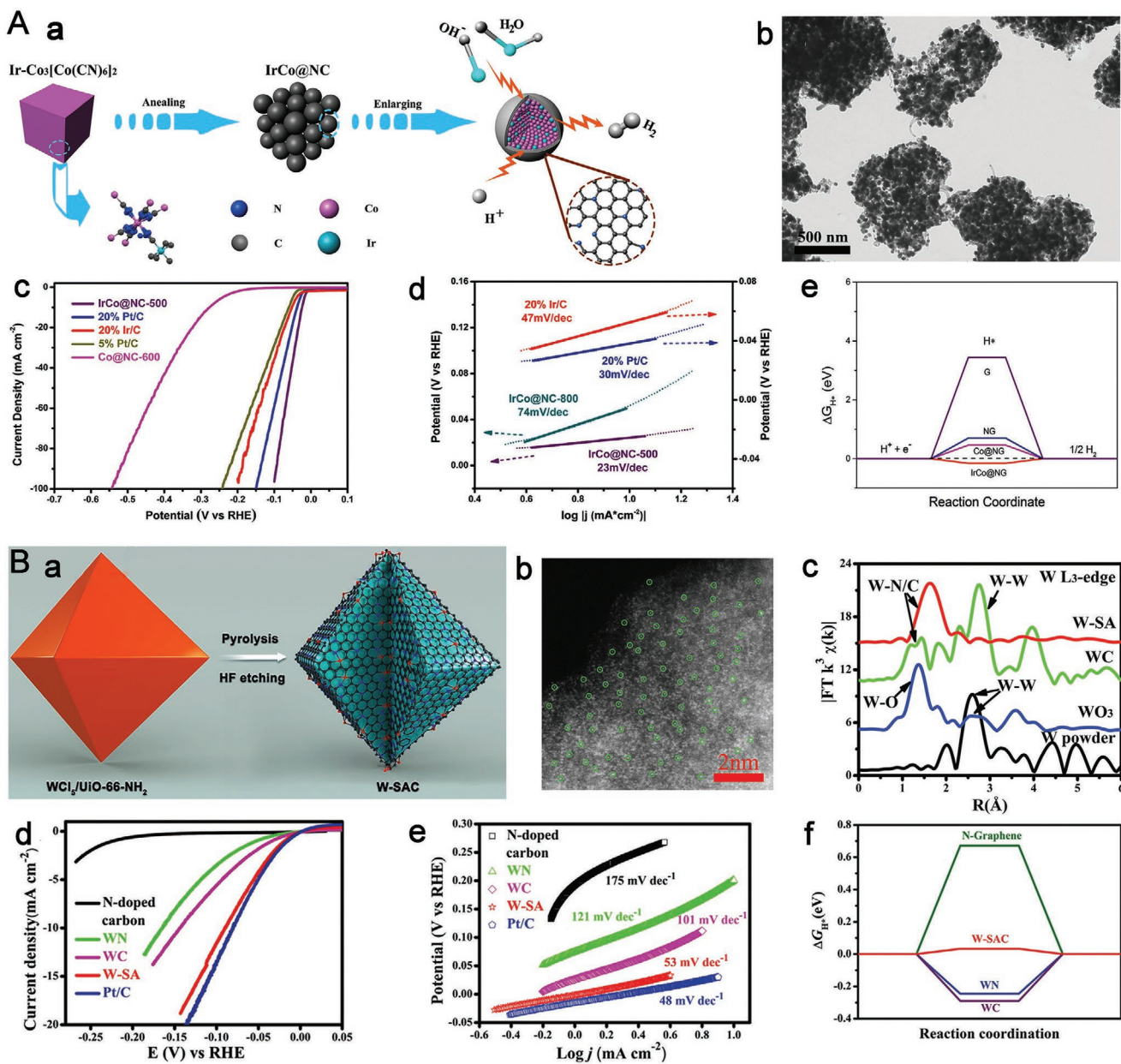


**Figure 11.** A) a) Schematic illustrating the preparation of IrCo@NC hybrid. b) TEM image of IrCo@NC-500. c) HER polarization curves and d) Tafel plot of IrCo@NC-500 and counterparts. e)  $\Delta G_{H^+}$  of the IrCo@NC-500 and counterparts. A) Reproduced with permission.<sup>[87]</sup> Copyright 2018, Wiley-VCH. B) a) Illustration of the formation of W-SAC. b) HAADF-STEM image of the W-SAC. c)  $k^3$ -weight FT-EXAFS curves of the W-SAC and the references at W  $L_3$ -edge. d) HER polarization curves, e) Tafel plots, and f)  $\Delta G_{H^+}$  of the W-SAC and counterparts. B) Reproduced with permission.<sup>[132]</sup> Copyright 2018, Wiley-VCH.

materials for the OER owing to their tunable structures, well-defined pores, and high specific surface areas. For instance, Zhang et al. prepared an Fe-MOF nanosheet array on Ni foam (Fe-MOF/NF) by the hydrothermal treatment, which showed outstanding electrocatalytic performance for the OER with an overpotential of approximately 240 mV at 50 mA cm<sup>-2</sup> and a relatively low Tafel slope of 72 mV dec<sup>-1</sup> in 1.0 M KOH.<sup>[181]</sup> Moreover, Fe-MOF/NF showed robust long-term electrochemical stability with its catalytic activity being maintained for no less than 30 h. Recently, Jiang et al. employed a microwave-induced plasma engraving strategy to achieve a fine regulation

of the coordinatively unsaturated metal sites of Co-MOF-74 with a distinctly improved OER activity and no damage to the integrity of its phase.<sup>[176]</sup> The hydrogen-plasma-engraved Co-MOF-74 exhibited superior OER activity in a 0.1 M KOH electrolyte with a relatively low overpotential of 337 mV at 15 mA cm<sup>-2</sup>, a high TOF of 0.0219 s<sup>-1</sup>, and large mass activity of 54.3 A g<sup>-1</sup>.

However, most MOFs bear intrinsic, low electronic conductivity, limited active sites, and poor chemical stability, which are the major barriers that hinder their electrocatalytic application for the OER. Therefore, many efficient strategies have been reported to strengthen the OER catalytic performance of MOFs.



**Table 2.** HER performances of MOF-based/-derived electrochemical catalysts (GCE: glassy carbon electrode; CC: carbon cloth; CFP: carbon fiber paper; FTO: fluorine-doped tin oxide).

Catalyst	Substrate	Electrolyte	Overpotential [mV] at 10 mA cm <sup>-2</sup>	Tafel slope [mV dec <sup>-1</sup> ]	Mass loading [mg cm <sup>-2</sup> ]
<b>MOF-based catalysts</b>					
Fe <sub>3</sub> S <sub>4</sub> (52.1 wt%)/MIL-53 <sup>[2]</sup>	GCE	0.1 M NaClO <sub>4</sub>	92	60	0.610
Gr (4 wt%) and Co-MOF <sup>[8]</sup>	GCE	0.5 M H <sub>2</sub> SO <sub>4</sub>	125	91	0.283
Ni <sub>3</sub> (Ni <sub>3</sub> -HAHATN) <sub>2</sub> <sup>[17]</sup>	GCE	0.1 M KOH	115	≈46	0.112
NiCo-MOF/rGOAS <sup>[18]</sup>	GCE	0.1 M KOH	210	73	
AB&CTGU-9 (3: 4) <sup>[19]</sup>	GCE	0.5 M H <sub>2</sub> SO <sub>4</sub>	128	87	0.070
2D Ni-MOF@Pt NSS <sup>[20]</sup>	GCE	0.5 M H <sub>2</sub> SO <sub>4</sub>	43	30	0.250
	GCE	1 M KOH	102	88	0.250
AB and CTGU-5 (1:4) <sup>[147]</sup>	GCE	0.5 M H <sub>2</sub> SO <sub>4</sub>	44	45	0.140
Cu-BHT NP <sup>[149]</sup>	GCE	0.5 M H <sub>2</sub> SO <sub>4</sub>	450	95	0.084
CoBHT <sup>[151]</sup>	GCE	pH 1.3 H <sub>2</sub> SO <sub>4</sub>	185	88	
NiBHT <sup>[151]</sup>	GCE	pH 1.3 H <sub>2</sub> SO <sub>4</sub>	331	67	
FeBHT <sup>[151]</sup>	GCE	pH 1.3 H <sub>2</sub> SO <sub>4</sub>	173	119	
2D Co-BDC/MoS <sub>2</sub> <sup>[154]</sup>	GCE	1 M KOH	248	86	0.160
Cu.BTC, 1.7 wt% AB <sup>[155]</sup>	GCE	0.5 M H <sub>2</sub> SO <sub>4</sub>	208	80	0.280
CoP/Co-MOF <sup>[156]</sup>	CC	1 M PBS	49	63	5.000
	CC	1 M KOH	34	56	5.000
	CC	0.5 M H <sub>2</sub> SO <sub>4</sub>	27	43	5.000
<b>MOF-derived catalysts</b>					
IrCo@NC-500 <sup>[87]</sup>	GCE	0.5 M H <sub>2</sub> SO <sub>4</sub>	24	23	0.285
	GCE	1 M KOH	45	80	0.285
CoP/NCNWs <sup>[100]</sup>	CFP	0.5 M H <sub>2</sub> SO <sub>4</sub>	95	50	1.000
	CFP	1 M KOH	154	59	1.000
	CFP	0.5 M H <sub>2</sub> SO <sub>4</sub>	72	54	0.390
NFP/C-3 <sup>[105]</sup>	CFP	1 M PBS	117	70	0.390
	CFP	1 M KOH	95	72	0.390
	CFP	0.5 M H <sub>2</sub> SO <sub>4</sub>	72	54	0.390
Co-Fe-P NTs <sup>[107]</sup>	GCE	0.1 M KOH	86	66	0.285
	GCE	1 M PBS	138	138	0.285
	GCE	0.5 M H <sub>2</sub> SO <sub>4</sub>	66	72	0.285
Ni <sub>2</sub> P/Ni@C <sup>[118]</sup>	GCE	0.5 M H <sub>2</sub> SO <sub>4</sub>	149	≈61	0.354
W <sub>1</sub> N <sub>1</sub> C <sub>3</sub> SAC <sup>[132]</sup>	GCE	0.1 M KOH	85	53	0.204
A-Ni-C <sup>[140]</sup>	GCE	0.5 M H <sub>2</sub> SO <sub>4</sub>	34	41	0.283
Ni <sub>2</sub> P/C <sup>[157]</sup>	GCE	0.5 M H <sub>2</sub> SO <sub>4</sub>	198	≈113	0.566
NHPBAP <sup>[158]</sup>	GCE	0.5 M H <sub>2</sub> SO <sub>4</sub>	70	52	0.285
	GCE	1 M KOH	121	67	0.285
Ni/NiO@C/GR-t-w <sup>[159]</sup>	GCE	0.5 M H <sub>2</sub> SO <sub>4</sub>	108	44	0.205
Ni/NiO-400 <sup>[160]</sup>	CC	1 M KOH	41	59	1.000
NiSe@NC-600 <sup>[161]</sup>	GCE	0.5 M H <sub>2</sub> SO <sub>4</sub>	123	≈53	0.350
	GCE	1 M KOH	250	≈55	0.350
	GCE	1 M PBS	300	≈66	0.350
NiFeP nanorods <sup>[162]</sup>	GCE	1 M KOH	178	69	0.071
Ni/C-1 <sup>[163]</sup>	GCE	1 M KOH	40	77	0.500
Ni@NC-rGO <sup>[164]</sup>	GCE	1 M KOH	218	≈99	1.400
CoSe <sub>2</sub> @NC-NR/CNT <sup>[165]</sup>	GCE	0.5 M H <sub>2</sub> SO <sub>4</sub>		≈50	1.300
CoP/Mo <sub>2</sub> C-NC <sup>[166]</sup>	GCE	0.5 M H <sub>2</sub> SO <sub>4</sub>	55.7	49	0.453
	GCE	1 M KOH	67.2	66	0.453

**Table 2.** Continued.

Catalyst	Substrate	Electrolyte	Overpotential [mV] at 10 mA cm <sup>-2</sup>	Tafel slope [mV dec <sup>-1</sup> ]	Mass loading [mg cm <sup>-2</sup> ]
CoPS/N-C <sup>[167]</sup>	GCE	0.5 M H <sub>2</sub> SO <sub>4</sub>	80	68	0.170
	GCE	1 M KOH	148	78	0.170
Co <sub>2</sub> Ni <sub>1</sub> N <sup>[168]</sup>	GCE	1 M KOH	≈102	≈60	0.240
	GCE	0.5 M H <sub>2</sub> SO <sub>4</sub>	92	≈55	0.240
	GCE	1 M PBS	≈153	≈90	0.240
CoNiP nanoboxes <sup>[169]</sup>	GCE	1 M KOH	138	65	0.517
Co-SA/p <sup>[170]</sup>	GCE	0.5 M H <sub>2</sub> SO <sub>4</sub>	98	47	0.102
Co-SAC <sup>[171]</sup>	GCE	0.5 M H <sub>2</sub> SO <sub>4</sub>	260	80	0.500
Py-ZIF <sup>[171]</sup>	GCE	0.5 M H <sub>2</sub> SO <sub>4</sub>	260	84	0.500
MoS-CoS-Zn <sup>[172]</sup>	GCE	0.5 M H <sub>2</sub> SO <sub>4</sub>	≈73	≈38	0.250
CoS <sub>x</sub> -(0.2-0.02)-12 <sup>[173]</sup>	FTO	1 M PBS	168	76	

For instance, incorporating nonbridging ligands into the MOF could significantly improve OER performance.<sup>[14,182]</sup> Converting bulk MOF crystals into 2D nanosheets could expose more active surface sites.<sup>[15,183–186]</sup> Additionally, multimetallic MOFs present a significant improvement in catalytic activity due to the synergistic effect between different metal sites.<sup>[35,187–194]</sup> Furthermore, MOF-involved hybridization, such as Ni-BDC/Ni(OH)<sub>2</sub>,<sup>[195]</sup> CoFeO<sub>x</sub>/Co-MOF,<sup>[16]</sup> and POM@ZIF-8,<sup>[196]</sup> have also been reported to accelerate the OER.<sup>[16,21,195–198]</sup> These explorations have promoted the further development of MOF-based OER electrocatalysts.

Theoretical calculations suggest that the electron structure of MOFs can be regulated by introducing missing linkers, which enhances the OER activity of the MOF.<sup>[14]</sup> Inspired by this, Xue et al. reported a universal strategy to introduce different missing linkers, such as carboxyferrocene (Fc), to regulate the electronic structure of layered-pillared MOF Co<sub>2</sub>(OH)<sub>2</sub>(C<sub>8</sub>H<sub>4</sub>O<sub>4</sub>) (CoBDC) (Figure 12Aa–c). The calculated density of states (DOS) of CoBDC and CoBDC-Fc revealed that new electronic states near the Fermi level were generated after introducing missing linkers, demonstrating that the CoBDC-Fc has a more conductive structure (Figure 12Ad). The conductive structure plays a critical role in improving the OER activity by introducing missing linkers into the MOF, which could reduce the energy barrier (Figure 12Ae). The self-supported CoBDC nanoarrays with missing linkers of Fc and NF serving as substrate (CoBDC-Fc-NF) exhibited remarkable OER activity with an ultralow overpotential of 241 mV at 100 mA cm<sup>-2</sup> and a small Tafel slope of 51 mV dec<sup>-1</sup> (Figure 12Af,g). More recently, Ji et al. proposed a facile linker scission strategy to induce lattice strain in MOF catalysts by partially replacing binary carboxylic acids with monocarboxylic acids.<sup>[182]</sup> The strained NiFe-MOFs with 6% lattice expansion showed excellent activity for the OER in an alkaline electrolyte with a low overpotential of 230 mV at a current density of 10 mA cm<sup>-2</sup> and a small Tafel slope of 86.6 mV dec<sup>-1</sup>.

A 2D sheet-like nanostructure could facilitate not only mass or electron transfer but also enable higher exposure of the active catalytic sites of unsaturated coordinated metal atoms, which remarkably enhances their intrinsic OER activity. Huang et al. developed a typical self-dissociation-assembly method to

fabricate well-defined, ultrathin CoNi-MOF nanosheet arrays (CoNi-MOFNA), which could be employed as a highly active OER electrode.<sup>[183]</sup> The catalysts achieved an extremely low overpotential of 215 mV at a current density of 10 mA cm<sup>-2</sup>, and its mass activity was 14 times that of commercial RuO<sub>2</sub>. Besides, the current density of CoNi-MOFNA showed no significant degradation even after 300 h of continuous electrolysis. Pang et al. reported a new method for preparing single-layer metal-organic nanosheets from 3D layered-pillared MOFs by capping solvent molecules prepared with sonication in a solvent over a comparatively short period (30 min).<sup>[15]</sup> The as-obtained single-layer metal-organic nanosheets exhibited higher OER activity than other heterogeneous catalysts.

Multimetallic MOFs, such as CoFe-,<sup>[187,190,192]</sup> NiCu-,<sup>[188]</sup> FeNi-,<sup>[189,191,193]</sup> NiCo-,<sup>[194]</sup> and NiCoFe-based MOFs,<sup>[35]</sup> have been reported with the enhanced catalytic performance for the OER relative to their monometallic counterparts. For example, Sun et al. proposed a self-templating approach to growing NiFe-based MOF nanosheets, such as MIL-53(FeNi)/NF, on foamed nickel in situ using a one-step solvothermal synthesis.<sup>[193]</sup> An overpotential of 233 mV at 10 mA cm<sup>-2</sup>, mass activity of 19.02 A g<sup>-1</sup>, Tafel slope of 31.3 mV dec<sup>-1</sup>, and desirable stability was obtained for MIL-53(FeNi)/NF in 1 M KOH electrolyte, demonstrating the superior OER performance of MIL-53(Ni). The encapsulation of the Fe species into MIL-53 could readily facilitate the modulation of the electronic structure, facilitate electron transport, and increase the number of active electrochemical areas to improve the catalytic performance.

MOF-based hybrids have also been reported to accelerate the OER. In a recent study, 2D Ni-BDC/Ni(OH)<sub>2</sub> hybrid nanosheets were fabricated by a simple sonication-assisted solution route.<sup>[195]</sup> Ni-BDC/Ni(OH)<sub>2</sub> showed excellent activity, desirable kinetics, and long-term stability for the OER. Because of the strong electronic interactions between Ni(OH)<sub>2</sub> and Ni-BDC, the electron structure of Ni(OH)<sub>2</sub> was fine-tuned. As a result, Ni(OH)<sub>2</sub> with higher oxidation states could be obtained; thus, the OER catalytic performance could be further improved. Notably, the OER current density of Ni-BDC/Ni(OH)<sub>2</sub> was 82.5 mA cm<sup>-2</sup> at 1.6 V versus RHE, outperforming the benchmark commercial Ir/C catalyst by up to three times. Ultrafine CoFeO<sub>x</sub> nanoparticles were immobilized in the lattice of a poly[Co<sub>2</sub>(benzimidazole)<sub>4</sub>] (PCB) layer. The



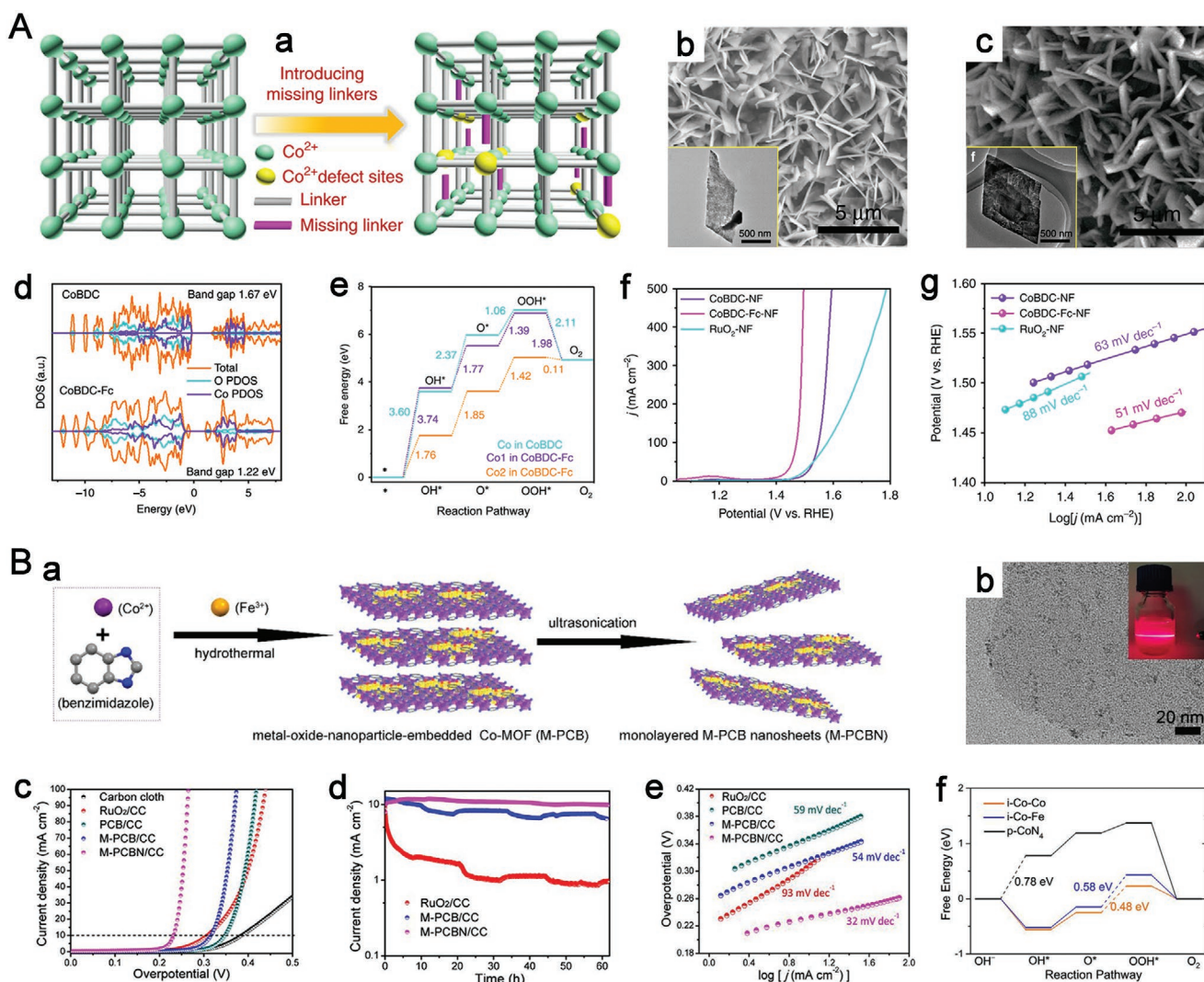


**Figure 12.** A) a) Schematic illustrating the modulation of the electron structure of MOFs by introducing missing linkers. b,c) SEM images of CoBDC-NF (b) and CoBDC-Fc-NF (c); inset: the corresponding TEM images. d) Calculated DOS of CoBDC and CoBDC-Fc in DFT calculations. e) Free energy diagrams toward the OER on CoBDC and CoBDC-Fc. f) OER LSV plots in 1 M KOH. g) Tafel plots of different catalysts. B) a) Reproduced under the terms of the CC-BY Creative Commons Attribution 4.0 International License (<https://creativecommons.org/licenses/by/4.0/>).<sup>[14]</sup> Copyright 2019, The Authors, published by Springer Nature. b) Schematic representation of the approach to fabricate M-PCBN. b) TEM images of M-PCBN. The inset shows the Tyndall effect of M-PCBN under laser irradiation. c) Comparison of the OER performance for all working electrodes. d) Chronoamperometry testing and e) Tafel plots for different catalysts. f) Calculated the free energy diagram of the OER on i-Co-Co, i-Co-Fe, and p-CoN<sub>4</sub> at the equilibrium potential (1.23 V). The dashed lines represent the potential-limiting steps. B) Reproduced with permission.<sup>[16]</sup> Copyright 2020, American Chemical Society.

metal-oxide-nanoparticle-embedded PCB (M-PCB) bulk microcrystals were further exfoliated into a layered heterostructure to obtain monolayered M-PCBN nanosheets (M-PCBN) by ultrasonication (Figure 12Ba).<sup>[16]</sup> The TEM image reveals the formation of M-PCBN with an ultrathin heterogeneous nanosheet structure (Figure 12Bb). Structural characterization and analysis suggested a changed 3d electronic configuration and a higher valence for the interfacial Co sites between the metal oxide nanoparticle and monolayered MOF, resulting in an enhanced OER activity, which was consistent with the theoretical calculations and electrochemistry measurements (Figure 12Bc–f). Electrochemical tests indicated the excellent OER activity and durability of the M-PCBN with an overpotential of 232 mV at 10 mA cm<sup>-2</sup> and a Tafel slope of 32 mV dec<sup>-1</sup>.

Over the past few years, MOF-derived transition metal (Fe, Ni, Co, Mo, Cu, etc.)-based compounds, including oxides,<sup>[113,199–202]</sup> hydroxides,<sup>[203]</sup> phosphides,<sup>[104,204]</sup> selenides,<sup>[205]</sup> nitrides,<sup>[94]</sup> borates, and chalcogenides,<sup>[103,206,207]</sup> have been employed extensively as electrocatalysts for the OER. Among these, Co-based transition metal oxides and (oxy)hydroxides, particularly cobalt-based polymetallic compounds,<sup>[112,208–213]</sup> are prominent owing to their unique 3d electronic configurations. Zhou et al. reported a facile strategy in which layered 2D MOFs were used as precursors to fabricate metal oxide/carbon (MO<sub>x</sub>/C, M = Co, Ni, and Cu) nanosheet arrays for the OER.<sup>[202]</sup> Owing to the enhanced conductivity and higher exposure of the active sites, these MO<sub>x</sub>/C arrays showed excellent electrocatalytic performance and good stability. In particular, Co<sub>3</sub>O<sub>4</sub>/C<sub>BDC</sub> exhibited ultralow

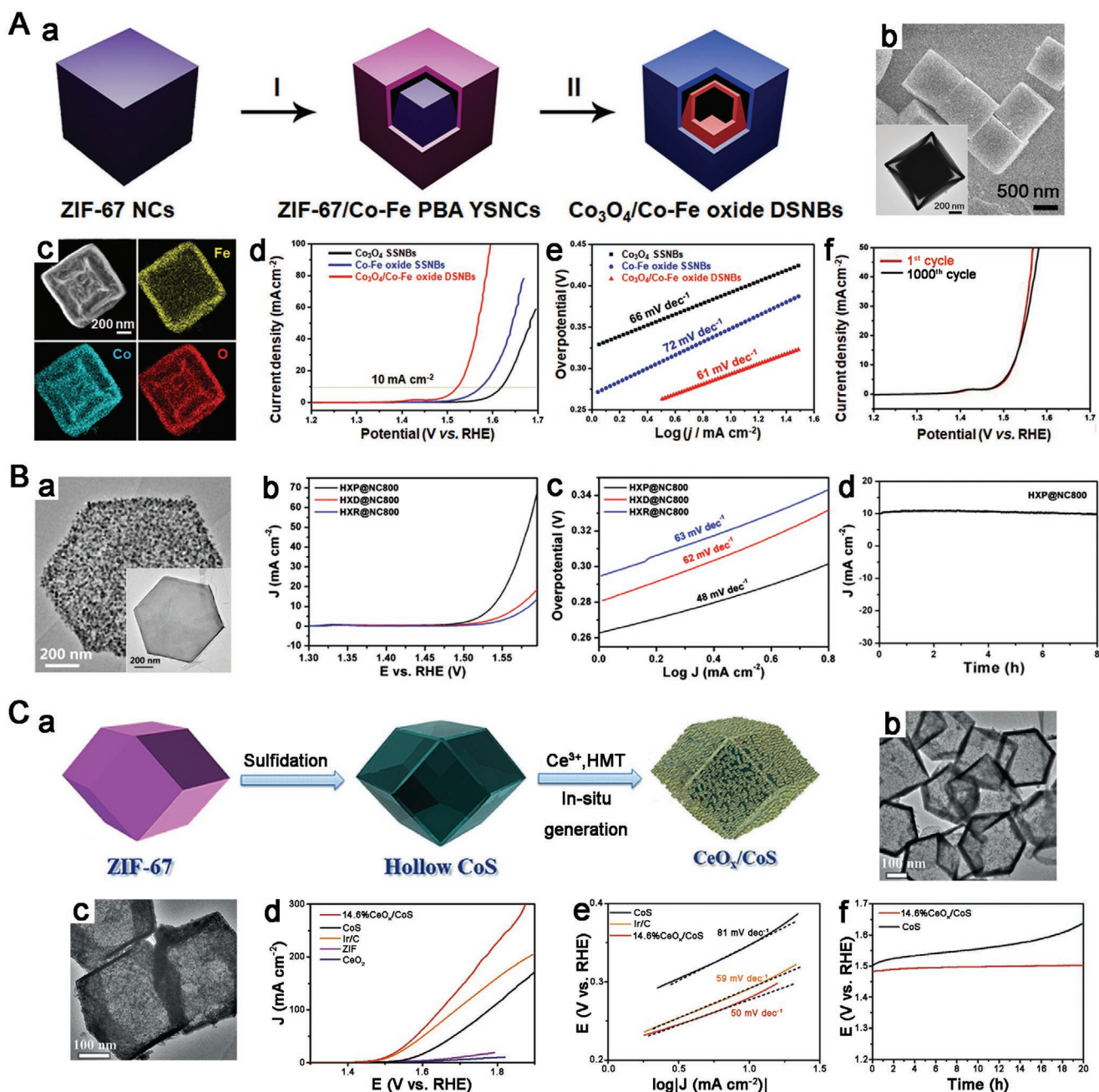


**Figure 13.** A) a) Schematic illustration of the route to synthesize  $\text{Co}_3\text{O}_4/\text{Co-Fe}$  oxide DSNBs. b) FESEM images of ZIF-67/Co-Fe PBA YSNCs (inset is the corresponding TEM image). c) HAADF-STEM and elemental mapping images of a  $\text{Co}_3\text{O}_4/\text{Co-Fe}$  oxide DSNB. d) LSV curves and e) Tafel plots of different electrocatalysts. f) LSV curves were obtained after continuous CV sweeps at  $5 \text{ mV s}^{-1}$  after the stability test. A) Reproduced with permission.<sup>[213]</sup> Copyright 2018, Wiley-VCH. B) a) TEM image of an individual HXP@NC800 nanoplate (inset is the corresponding HXP image). b) LSV curves, c) corresponding Tafel plots, and d) chronoamperometry curve of HXP@NC800 measured on graphite foil. B) Reproduced with permission.<sup>[218]</sup> Copyright 2020, American Chemical Society. C) a) Illustration of the preparation approach of the hybrid nanostructure  $\text{CeO}_x/\text{CoS}$ . b, c) TEM images for CoS (b) and for 14.6%  $\text{CeO}_x/\text{CoS}$  (c). d) LSV curves and e) Tafel plots of various catalysts for the OER. f) Chronopotentiometric curves of water electrolysis for CoS and 14.6%  $\text{CeO}_x/\text{CoS}$ . C) Reproduced with permission.<sup>[223]</sup> Copyright 2018, Wiley-VCH.

overpotentials of 208 mV at a current density of  $10 \text{ mA cm}^{-2}$ . Lou et al. fabricated unique  $\text{Co}_3\text{O}_4/\text{Co-Fe}$  oxide double-shelled nanoboxes (DSNBs) by a successive anion-exchange and pyrolysis strategy (Figure 13Aa).<sup>[213]</sup> In the first step, an anion-exchange process between the ZIF-67 NCs and  $[\text{Fe}(\text{CN})_6]^{3-}$  ions was performed to transform the ZIF-67 NCs into ZIF-67/Co-Fe

PBA yolk-shell nanocubes (YSNCs) (Figure 13Ab).  $\text{Co}_3\text{O}_4/\text{Co-Fe}$  DSNBs were synthesized by a subsequent annealing treatment (Figure 13Ac). The as-obtained hybrids exhibited superior electrocatalytic activity and stability for the OER compared to Co-Fe oxides and  $\text{Co}_3\text{O}_4$  single-shelled nanoboxes owing to their structural and compositional advantages (Figure 13Ad–f).



Many researchers have also found that MOFs can act as attractive templates or precursors to prepare porous carbon-encapsulated metal (M@C) materials via a pyrolysis method.<sup>[79,214–220]</sup> The M@C materials retain not only the large surface area of their parental MOFs but also show excellent conductivity and catalytic activity. Meanwhile, the metal nodes around organic ligands can be reduced in situ to single atomic sites<sup>[221]</sup> or bimetal alloy<sup>[82,88,89,222]</sup> cores encapsulated in a heteroatom-doped carbon frame after pyrolysis under an inert gas atmosphere. The resulting materials possess a unique electronic effect and extra synergistic effect, resulting in the acceleration of the catalytic reaction kinetics for the OER. Recently, Lin et al. reported a topology-guided synthetic procedure for a novel 2D Ni-based MOF hexagonal nanoplate (HXP).<sup>[218]</sup> Under the inhibition and modulation of pyridine in the substitution-suppression process, the morphology could be changed from hexagonal nanorods (HXR) to nanodisks (HXD) and nanoplates with controllable thickness by regulating the amount of pyridine. Moreover, a subsequent calcination process transformed the nanoplates into nitrogen-doped Ni@carbon nanocomposites (Figure 13Ba), which showed a low overpotential of 307 mV at a current density of 10 mA cm<sup>-2</sup>, Tafel slope as low as 48 mV dec<sup>-1</sup>, and satisfactory durability in the OER (Figure 13Bb–d). Bu et al. developed a versatile, ultrafast microwave-assisted chemical vapor deposition (CVD)-like route to synthesize a variety of uniformly dispersed mono- or few-layer N-doped graphene shell immobilized metal nanocrystals (M@NC) within 10 s using MOFs on graphene as the precursors in the presence of carbon cloth (CC).<sup>[82]</sup> Among the M@NCs, the as-synthesized FeNi@NC/graphene exhibited the best electrocatalytic activity toward the OER with the lowest overpotential (261 mV) at 10 mA cm<sup>-2</sup> in 1 M KOH, the smallest Tafel slope of 40 mV dec<sup>-1</sup>, and robust stability for no less than 120 h.

Studies have demonstrated that MOF-derived materials without high-temperature treatment were also employed as OER catalysts. For instance, Xu et al. proposed a new hybrid nanostructure CeO<sub>x</sub>/CoS consisting of hollow CoS derived from ZIF-67, which was decorated with CeO<sub>x</sub> nanoparticles grown in situ (Figure 13Ca).<sup>[223]</sup> The TEM images of the precursor CoS and 14.6% CeO<sub>x</sub>/CoS are displayed in Figure 13Cb,c, respectively. The obtained CeO<sub>x</sub>/CoS hybrid exhibited outstanding OER performance by regulating the surface electron states and producing defective sites, which is related to the increase in the Co<sup>2+</sup>/Co<sup>3+</sup> molar ratio and defect number. Additionally, the deposition of CeO<sub>x</sub> in situ on the surface of the CoS hollow structures can avoid the corrosion of CoS. As expected, the CeO<sub>x</sub>/CoS exhibited a low overpotential of 269 mV at 10 mA cm<sup>-2</sup>, a low Tafel slope of 50 mV dec<sup>-1</sup>, and significant operational stability in an alkaline electrolyte (Figure 13Cd–f). Hollow (Ni, Co)Se<sub>2</sub> arrays immobilized on flexible CC originating from cobalt-MOF via an ion-exchange/etching reaction, and following solvothermal selenization exhibited excellent OER performance, as reported by Song et al.<sup>[224]</sup> Similarly, Li et al. successfully synthesized a hierarchical hollow (Co, Ni)Se<sub>2</sub>@NiFe layered double hydroxide (LDH) nanocage originating from ZIF-67 for efficient OER with a facile ion-exchanged method and then decorated the nanocage with NiFe LDH to enhance the electrocatalytic kinetics further.<sup>[225]</sup> Qiu et al. reported a universal and straightforward approach to preparing a boundary defect-rich, ultrathin

Co(OH)<sub>2</sub> (D-U-Co(OH)<sub>2</sub>) nanoarray under room temperature for the OER by in situ etching of a Co-MOF (ZIF-L-Co).<sup>[226]</sup> Here, the remarkable OER performances of recently reported MOF-based/derived electrocatalysts are summarized (Table 3).

### 3.3. Bifunctional Electrochemical Catalysts (HER + OER)

Electrochemical water splitting consists of two half-reactions: the HER occurs at the cathode and the OER occurs at the anode. The cell voltage to afford a specific current density (generally 10 mA cm<sup>-2</sup>) in an electrolysis cell is generally applied to assess the HER/OER bifunctional performance of the electrocatalyst. In this section, MOF-based/derived catalytic materials with activities for both OER and HER will be discussed.

A small number of MOF-based materials have emerged as electrocatalysts for water splitting, mainly due to their low electrical conductivity and stability.<sup>[12,227,228]</sup> 2D MOFs have been demonstrated to have enhanced conductivity and more exposure to active sites. For instance, Duan et al. developed a 2D bimetallic MOF on conductive substrates for high-efficiency water electrolysis via a dissolution–crystallization process.<sup>[53]</sup> Recently, Xu et al. reported another 2D MOF-based catalyst (ultrathin Ni-ZIF/Ni-B NSs with massive crystalline–amorphous phase interfaces), which was derived from Ni-ZIF nanorods through a facile and room-temperature boronization strategy.<sup>[229]</sup> Remarkably, the Ni-ZIF/Ni-B@NF required an extremely low cell voltage of 1.54 V for overall water splitting to achieve a current density of 10 mA cm<sup>-2</sup>. By hybridizing the 2D Ni-MOF and noble Pt nanocrystals into one heterostructure, an interfacial-bond-induced charge transfer takes place and electronically optimizes the active sites further to modify intermediate adsorption (Figure 14Aa), providing significant electrocatalysis behavior.<sup>[230]</sup> The aberration-corrected TEM image reveals the interfacial structures of the Pt-NC/Ni-MOF at the atomic scale (Figure 14Ab). The positive shift of A<sub>1</sub> and A<sub>2</sub> is attributed to the electronic state transition from low-energy Ni 2p<sub>3/2</sub> to high-energy Ni 3d, optimizing the adsorption of OH\* (Figure 14Ac). The as-prepared Pt-NC/Ni-MOF presented outstanding electrocatalytic performance for both the HER and OER (Figure 14Ae) and outstanding stability toward the HER (Figure 14Ad).

Lu et al. synthesized a Ni- and Fe-based bimetallic MOF on a conducting Ni foam, NFN-MOF/NF, which is an efficient and stable electrocatalyst with double function for water splitting (Figure 14Ba).<sup>[231]</sup> These NFN-MOF/NF materials are nanosheets with thicknesses of approximately 15 nm and are bundled into micrometer-sized clusters (Figure 14Bb). The NFN-MOF/NF catalyst can provide a current density of 10 mA cm<sup>-2</sup> at a low cell voltage of 1.56 V, which is better than the performance of the Pt-C/NF//IrO<sub>2</sub>/NF couple, the accepted benchmark catalysts (Figure 14Bc). The Tafel slope of 143 mV dec<sup>-1</sup> obtained for the NFN-MOF/NF//NFN-MOF/NF couple is also considerably lower than that of the benchmark couple (160 mV dec<sup>-1</sup>) (Figure 14Bd). Moreover, the NFN-MOF/NF catalysts possess remarkable durability, presenting negligible chronopotentiometry decay of 7.8% at 500 mA cm<sup>-2</sup> after 30 h (Figure 14Be). Recently, Lu et al. further developed well-blended Fe- and Ni-MOFs<sup>[232]</sup> and modulated Fe-rich FeNi(BDC)(DMF,F) and



**Table 3.** OER performance of MOF-based/derived catalysts (NF: Ni foam; CP: carbon paper).

Catalyst	Substrate	Electrolyte	Overpotential [mV] at 10 mA cm <sup>-2</sup>	Tafel slope [mV dec <sup>-1</sup> ]	Mass loading [mg cm <sup>-2</sup> ]
<b>MOF-based catalysts</b>					
CoBDC-Fc-NF <sup>[14]</sup>	NF	1 M KOH	178	51	2.000
M-PCBN <sup>[16]</sup>	CC	1 M KOH	232	32	0.928
Co-MOF NS/CC <sup>[175]</sup>	CC	1 M KOH	$\eta_{20} = 330$	$\approx 107$	7.195
Co-MOF-74 <sup>[176]</sup>	GCE	0.1 M KOH	$\eta_{15} = 337$		0.396
Mn(TCNQ) <sub>2</sub> <sup>[177]</sup>	Copper foam	1 M KOH	$\eta_{20} = 306$	166	3.100
Ni MOF (BTC) <sup>[178]</sup>	CP	1 M KOH	346	64	0.480
Ni-MOF NSs <sup>[179]</sup>	NF	1 M KOH	320	123	4.500
Fe(TCNQ) <sub>2</sub> <sup>[180]</sup>	Fe	1 M KOH	340	110	0.490
Fe-MOF <sup>[181]</sup>	NF	1 M KOH	$\eta_{50} = 370$	72	5.900
LS-6%-NiFe-MOFs <sup>[182]</sup>	GCE	1 M KOH	230	$\approx 87$	0.343
CoNi-MOFNA <sup>[183]</sup>		1 M KOH	215	$\approx 52$	
2D Co-MOF NSs <sup>[184]</sup>	GCE	1 M KOH	263	74	0.250
Fe:2D-Co-NS@Ni <sup>[185]</sup>	GCE	0.1 M KOH	211	46	0.210
NiPc-MOF <sup>[186]</sup>	FTO	1 M KOH		74	$\approx 0.008$
Co <sub>0.6</sub> Fe <sub>0.4</sub> -MOF-74 <sup>[187]</sup>	GCE	1 M KOH	280	56	
NiCu-MOF NSs <sup>[188]</sup>	NF	1 M KOH	$\eta_{100} = 290$	$\approx 107$	4.200
NNU-22 <sup>[189]</sup>	CC	0.1 M KOH	376	$\approx 77$	
A <sub>2.7</sub> B-MOF-FeCo <sub>1.6</sub> <sup>[190]</sup>	GCE	1 M KOH	288	39	0.350
NiFe-MOF-74 <sup>[191]</sup>	NF	1 M KOH	223	$\approx 72$	1.000
CoFe-MOF <sup>[192]</sup>	GCE	1 M KOH	263	44	0.212
MIL-53(FeNi)/NF <sup>[193]</sup>	NF	1 M KOH	$\eta_{50} = 233$	$\approx 31$	2.630
CTGU-10c2 <sup>[194]</sup>		1 M KOH	240	58	
2D Ni-BDC/Ni(OH) <sub>2</sub> <sup>[195]</sup>	GCE	1 M KOH	320	41	0.159
POM@ZIF-8 <sup>[196]</sup>	GCE	0.1 M Na <sub>2</sub> SO <sub>4</sub>	$\eta_1 = 784.19$	$\approx 784$	0.057
Fe-MOFs@Ni-MOFs <sup>[197]</sup>	Carbon Paper	1 M KOH	275	$\approx 57$	1.000
Ni-MOF@Fe-MOF <sup>[198]</sup>	GCE	1 M KOH	256	82	0.200
<b>MOF-derived catalysts</b>					
CoNC-CNF-1000 <sup>[29]</sup>	GCE	0.1 M KOH	450	94	0.132
FeNi@NC/RGO <sup>[82]</sup>	GCE	1 M KOH	261	40	0.510
CoDNI-N/C p <sup>[89]</sup>	GCE	0.1 M KOH	360	72	0.300
Co <sub>9</sub> S <sub>8</sub> /NSCNFs-850 <sup>[103]</sup>	GCE	1 M KOH	302	54	0.212
Fe <sub>1</sub> Co <sub>2</sub> -P/C <sup>[104]</sup>	GCE	1 M KOH	362	$\approx 50$	0.170
ZnCo-Fe-20 <sup>[112]</sup>	GCE	1 M KOH	176	$\approx 69$	0.255
Mg-RuO <sub>2</sub> (350) <sup>[113]</sup>	GCE	0.5 M H <sub>2</sub> SO <sub>4</sub>	228	$\approx 49$	
Cu@CuO-C <sup>[199]</sup>	Carbon fiber cloth	1 M KOH	340	156	1.100
M-Co <sub>3</sub> O <sub>4</sub> <sup>[200]</sup>	NF	1 M KOH	230	74	
Co@Co <sub>3</sub> O <sub>4</sub> <sup>[201]</sup>	GCE	1 M KOH	333	69	0.204
Co <sub>3</sub> O <sub>4</sub> /CBDC <sup>[202]</sup>		1 M KOH	208	$\approx 50$	
CoTFBDC/EG_250 <sup>[203]</sup>	GCE	1 M KOH		$\approx 40$	0.100
CNTs@NiCoP/C <sup>[204]</sup>	GCE	1 M KOH	297	$\approx 57$	0.354
Co-Fe-P-Se/NC <sup>[205]</sup>	GCE	1 M KOH	270	42	0.350
Co <sub>9</sub> S <sub>8</sub> @CT-800 <sup>[206]</sup>	GCE	0.1 M KOH	390	72	0.200
NiCoS/Ti <sub>3</sub> C <sub>2</sub> T <sub>x</sub> <sup>[207]</sup>	GCE	1 M KOH	365	$\approx 58$	0.210
Co <sub>3</sub> O <sub>4</sub> /CoMoO <sub>4</sub> -50 <sup>[209]</sup>	GCE	1 M KOH	318	63	0.255
MoO <sub>2</sub> -Co <sub>2</sub> Mo <sub>3</sub> O <sub>8</sub> @C NRs <sup>[210]</sup>	GCE	1 M KOH	320	88	0.200
NiCo@NiCoO <sub>2</sub> /C PMRAs <sup>[212]</sup>	CFC	1 M KOH	$\eta_{20} = 366$	$\approx 84$	3.200

Table 3. Continued.

Catalyst	Substrate	Electrolyte	Overpotential [mV] at 10 mA cm <sup>-2</sup>	Tafel slope [mV dec <sup>-1</sup> ]	Mass loading [mg cm <sup>-2</sup> ]
Co <sub>3</sub> O <sub>4</sub> /Co-Fe oxide DSNBs <sup>[213]</sup>	GCE	1 M KOH	297	61	0.255
Co-N <sub>x</sub> /C NRA <sup>[214]</sup>	GCE	6 M KOH	300	≈62	0.510
MnO@Co-N/C <sup>[215]</sup>	GCE	0.1 M KOH	450	112	0.255
Co-N/PC@CNT <sup>[216]</sup>	GCE	0.1 M KOH	400	89	0.255
CoTIB-C/C <sup>[217]</sup>	GCE	0.1 M KOH	509	≈165	0.400
HXP@NC800 <sup>[218]</sup>	GCE	1 M KOH	307	48	0.200
P-Co-NC-4 <sup>[220]</sup>	GCE	1 M KOH	315	≈76	0.400
CoSAs@CNTs <sup>[221]</sup>	GCE	0.1 M KOH	410	85	0.300
CeO <sub>x</sub> /CoS <sup>[223]</sup>	GCE	1 M KOH	269	50	0.200
(Ni <sub>1</sub> Co) <sub>2</sub> Se <sub>2</sub> /CC <sup>[224]</sup>	CC	1 M KOH	256	74	
Co(OH) <sub>2</sub> (D-U-Co(OH) <sub>2</sub> ) <sup>[226]</sup>	GCE	1 M KOH	223	131	0.620

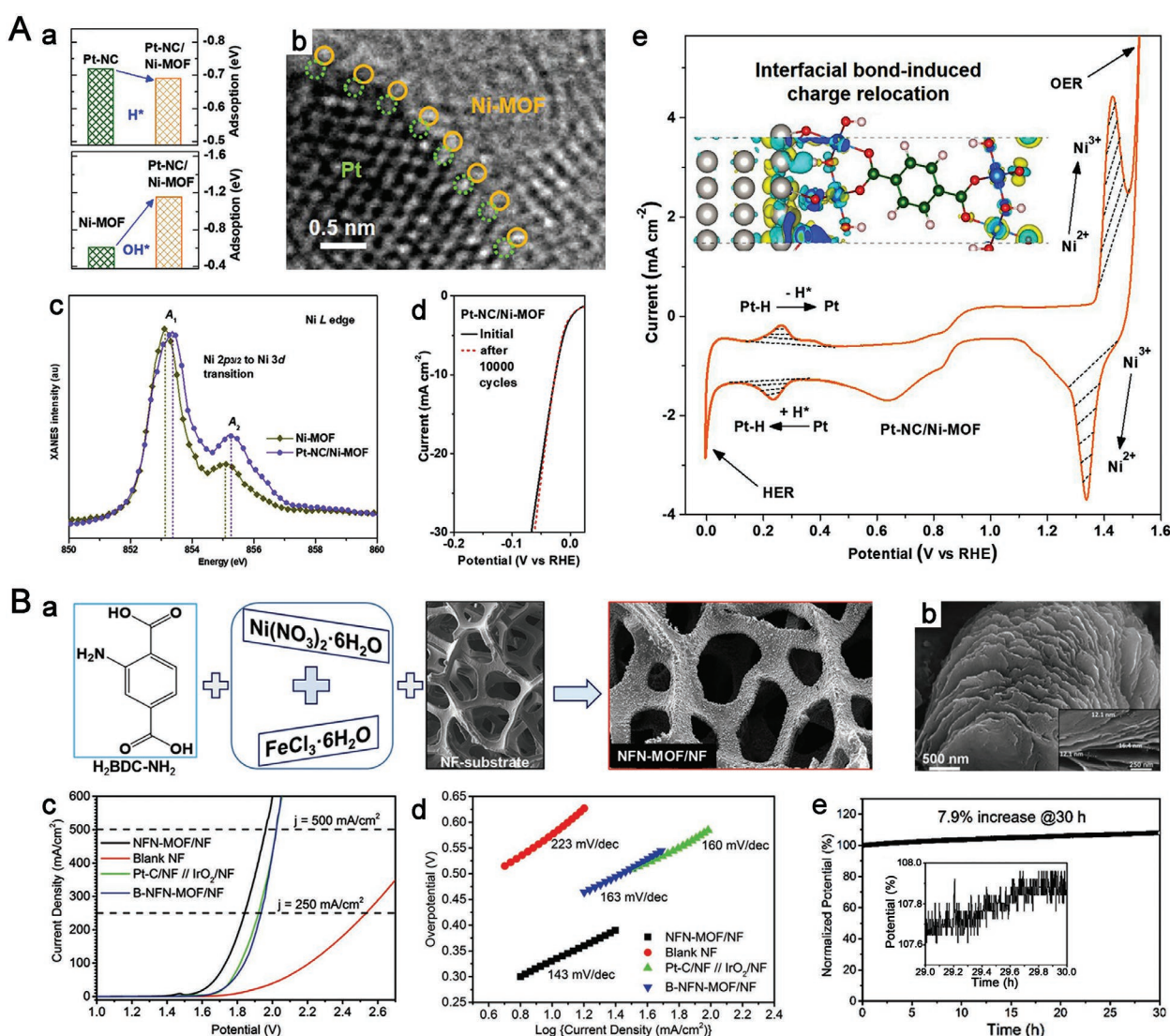


**Figure 14.** A) a) H\* and OH\* adsorption energy comparison and b) morphology of the Pt-NC/Ni-MOF. c) Synchrotron-based XANES Ni L<sub>3</sub> edge spectra of the materials investigated. d) Durability test by recording LSV curves. e) CV curves for Pt-NC/Ni-MOF. B) a) Schematic illustration of the synthetic process of NFN-MOF/NF. b) SEM image of NFN-MOF/NF. c) LSV curves and d) corresponding Tafel plots for couples with different components. e) Stability test of NFN-MOF/NF. B) Reproduced with permission.<sup>[230]</sup> Copyright 2019, Elsevier Ltd. B) a) Schematic illustration of the synthetic process of NFN-MOF/NF. b) SEM image of NFN-MOF/NF. c) LSV curves and d) corresponding Tafel plots for couples with different components. e) Stability test of NFN-MOF/NF. B) Reproduced with permission.<sup>[231]</sup> Copyright 2018, Wiley-VCH.

Ni-rich FeNi(BDC)(F),<sup>[233]</sup> grown in situ on NF, to obtain MOF/NF composite electrodes, which showed remarkable electrocatalytic activity for water splitting as well as outstanding durability at a high current density.

In recent years, to reduce the overpotential ( $\eta$ ) resulting from the OER on the anode and the HER on the cathode, a wide variety of MOF-derived carbon-based materials have been thoroughly explored (e.g., noble metals,<sup>[70]</sup> non-noble metals/alloys,<sup>[64,65,76,234–236]</sup> metal carbides,<sup>[237]</sup> oxides,<sup>[238]</sup> chalcogenides,<sup>[239–241]</sup> phosphides,<sup>[242–252]</sup> etc.<sup>[253–255]</sup>). Among them, transition metal phosphides (Fe<sub>2</sub>P,<sup>[243]</sup> CoP,<sup>[246]</sup> Ni<sub>2</sub>P,<sup>[251,252]</sup> etc.) are promising for overall water splitting because of their remarkable activity, excellent stability, and low fabrication cost. In particular, bimetallic phosphides can further enhance the electrocatalytic activity by adjusting the atomic coordination and electronic structure.<sup>[242,245,247–250]</sup> Recently, Sun et al. reported that an Fe-doped Ni(BDC) MOF (BDC = 1,4-benzenedicarboxylate) was utilized as the precursor to synthesize Fe-doped Ni<sub>2</sub>P/C toward highly efficient water splitting (Figure 15Aa).<sup>[249]</sup> As shown in Figure 15Ab, Fe-doped Ni<sub>2</sub>P nanoparticles were encapsulated in the CNTs after the phosphorization process. More importantly, Sun et al. employed

DFT calculations and a series of experiments to systematically analyze and evaluate the effect of phosphorization and Fe doping (Figure 15Ac,d). The results show that while phosphorization is more beneficial for the OER than the HER, Fe doping is not only able to tune the micromorphology of the catalyst but also modulate the electronic structure, synergistically resulting in enhanced HER and OER. Consequently, the hybrid displayed outstanding electrocatalytic performance for overall water splitting with a cell voltage of 1.66 V at 500 mA cm<sup>-2</sup>, which is far better than the standard electrode couple consisting of Pt/C and RuO<sub>2</sub> (Figure 15Ae). Cao et al. designed a 3D bifunctional porous Fe-CoP electrocatalyst formed by directly growing a Co-Fe PBA on Ni foam with further phosphorization, showing excellent performance toward large current density OER and overall water splitting.<sup>[250]</sup> The obtained Fe-CoP/NF catalyst with meso- and macropores presented high electrocatalytic efficiency and excellent stability for the OER and HER, reaching a current density of 10 mA cm<sup>-2</sup> with a rather low cell voltage of 1.49 V in 1.0 M KOH, which far outperforms that of the electrolyzer with IrO<sub>2</sub>-Pt/C as the electrode couple. Notably, the catalyst showed remarkable electrocatalytic performance for the OER and provided high

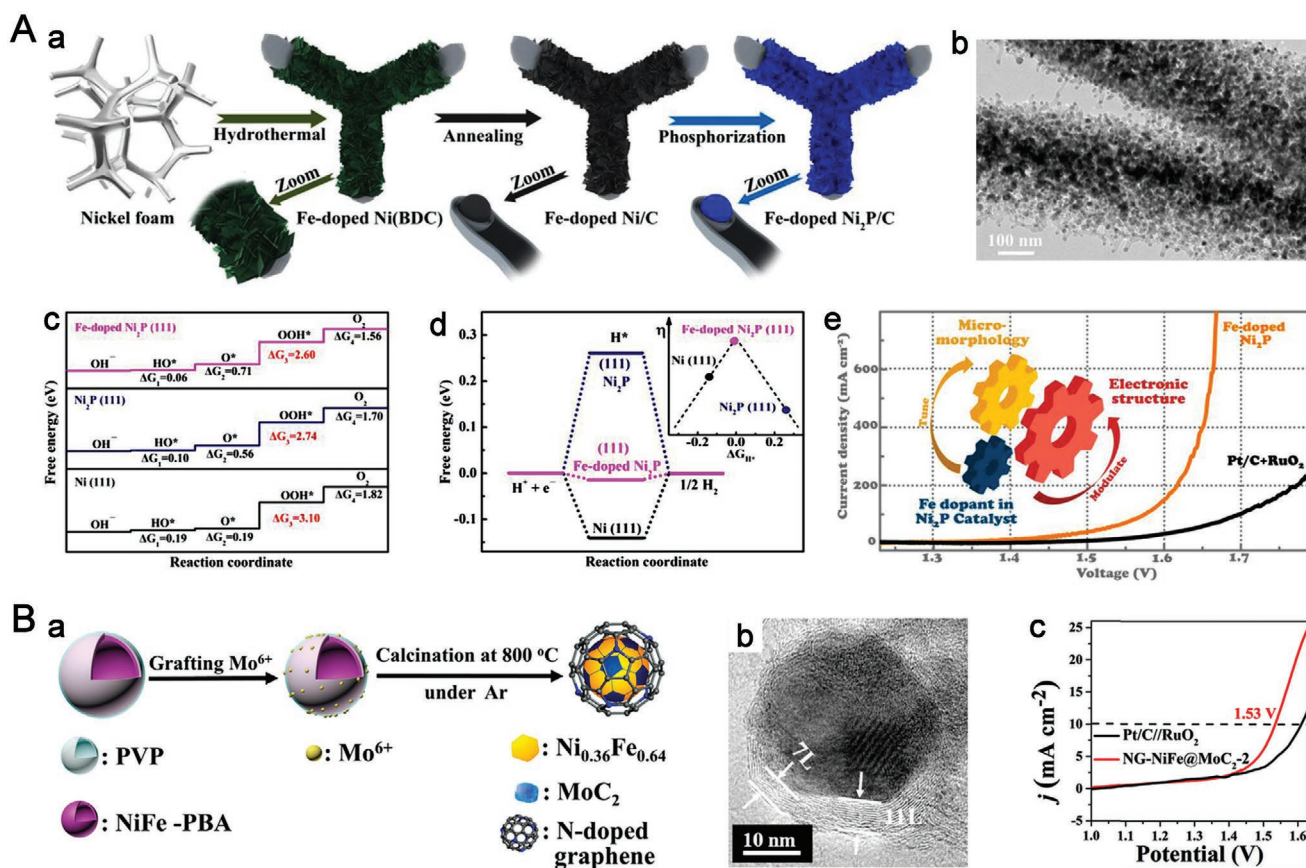


**Figure 15.** A) a) Schematic illustration of Fe-doped Ni<sub>2</sub>P/C catalyst preparation. b) TEM image of Fe<sub>2</sub>-Ni<sub>2</sub>P/C. c) Free-energy diagrams of the intermediates on different modeled surfaces for the OER. d)  $\Delta G_{\text{H}^*}$  for the HER. Inset: Volcano plot depicting the HER overpotentials as a function of  $\Delta G_{\text{H}^*}$ . e) Polarization curves of overall water splitting in a water electrolyzer. A) Reproduced with permission.<sup>[249]</sup> Copyright 2019, American Chemical Society. B) a) Schematic illustration of the synthetic procedure for NG-NiFe@MoC<sub>2</sub>. b) HRTEM image of NG-NiFe@MoC<sub>2</sub>. c) LSV of water electrolysis with non-noble NG-NiFe@MoC<sub>2</sub> and a noble couple of Pt/C//RuO<sub>2</sub> in 1 M KOH condition. Inset: stability testing of the electrolyzer at 10 mA cm<sup>-2</sup>. B) Reproduced with permission.<sup>[256]</sup> Copyright 2018, Elsevier Ltd.



current densities of 500 and 1000 mA cm<sup>-2</sup>, only requiring ultralow overpotentials of 295 and 428 mV, respectively, to satisfy the rigorous criteria for practical industrial applications.

In recent times, a versatile strategy for designing high-performance electrocatalysts has been to controllably introduce two different metal species into a single nanostructure, namely Co-NC@Mo<sub>2</sub>C,<sup>[119]</sup> Co<sub>3</sub>O<sub>4</sub>-RuCo@NC,<sup>[121]</sup> NG-NiFe@MoC<sub>2</sub>,<sup>[256]</sup> Co/Co<sub>9</sub>S<sub>8</sub>@NSOC,<sup>[122]</sup> NiO/Co<sub>3</sub>O<sub>4</sub>,<sup>[120]</sup> Co@Ir/NC,<sup>[257]</sup> Ni<sub>2</sub>P/CoN-PCP,<sup>[258]</sup> among others,<sup>[92,259–264]</sup> to further facilitate and accelerate the activation process of the reactants. For instance, Hu et al. synthesized MoC<sub>2</sub>-doped NiFe alloy nanoparticles (NPs) embedded within several-layer-thick N-doped graphene (NG-NiFe@MoC<sub>2</sub>) using one-step calcination of hybrid precursors composed of PVP-encapsulating NiFe-PBA and grafted Mo<sup>6+</sup> cations (Figure 15Ba).<sup>[256]</sup> The HRTEM image of NG-NiFe@MoC<sub>2</sub> (Figure 15Bb) demonstrated that the majority of NPs were embedded within several layers of the graphene shell. An NG-NiFe@MoC<sub>2</sub>-based water electrolyzer required a potential of 1.53 V to reach a current density of 10 mA cm<sup>-2</sup> in 1.0 M KOH with impressive durability of 10 h, exceeding the noble Pt/C//RuO<sub>2</sub>-based electrolyzer (Figure 15Bc). Recently, Du et al.<sup>[122]</sup> proposed a facile route to fabricate Co/Co<sub>9</sub>S<sub>8</sub> nanoparticles incorporated into an N, S, and O ternary-doped carbon support with a Co-based MOF (Co-NSOMOF) as a single precursor. The optimized Co/Co<sub>9</sub>S<sub>8</sub>@NSOC exhibited impressive performance for overall water splitting, resulting from the synergistic effects and protection of the ternary-doped carbon shell, requiring a rather low cell voltage of 1.56 V at 10 mA cm<sup>-2</sup>. The electrochemical performances of recent MOF-based/derived catalysts for water splitting considered in this review are listed in **Table 4**.

To briefly conclude, MOF-based/derived materials exhibit a prospect of widespread application as water-splitting electrocatalysts. For the HER under alkaline conditions, the reacting species are H<sub>2</sub>O or OH<sup>-</sup>, which possess much lower conversion kinetics to H\* than the conversion from H<sup>+</sup> to H\* under acidic conditions. As a result, the HER performance under acidic conditions is generally superior to that under alkaline conditions, as identified with the works reviewed above. In contrast to the OER electrocatalysts, Mo- and W-based materials have been widely used to catalyze the HER. Rather than metal oxides and hydroxides commonly employed as OER catalysts, other types of metal compounds (e.g., phosphides, nitrides, and chalcogenides) exhibit outstanding HER performance. As shown in **Figure 16a,b**, a MOF-based/derived catalyst with an overpotential of 150 mV at a current density of 10 mA cm<sup>-2</sup> can be considered as an excellent catalyst for the HER.

Various kinds of MOF-based electrocatalysts with remarkable OER electrocatalysis behavior have been reported (Figure 16c). Apart from the catalytic performance, electrocatalysts for the OER need excellent stability under harsh alkaline environments. Thus, for MOF-derived OER catalysts, a high extent of graphitization of the carbon substrate and the existence of metal-based constituents are favored. Moreover, a limited number of studies on MOF-derived SACs for water oxidation have been reported, resulting from the SACs migrating and aggregating into NPs under harsh reaction conditions. Figure 16d shows, through appropriate design of the composition and structure, some MOF-derived electrocatalysts can attain high OER activity with an overpotential of no more than 300 mV at 10 mA cm<sup>-2</sup>.

Water electrolysis is the main application of HER/OER bifunctional catalysts, which can effectively optimize the energy utilization of the water electrolyzer. The cell voltage to afford a particular current density (generally 10 mA cm<sup>-2</sup>) in an electrolysis cell is commonly applied to estimate the activity of an HER/OER bifunctional electrocatalyst. A large variety of MOF-based materials and MOF-derived carbon-based materials (e.g., metal NPs, metal carbides, phosphides, and complicated metal compounds) have been explored for efficient water splitting (Figure 16e,f). The MOF-based/derived catalyst with a cell voltage of less than 1.6 V at 10 mA cm<sup>-2</sup> can be regarded as an excellent catalyst for water splitting.

## 4. Conclusions and Perspectives

We have reviewed pivotal advances and provided commentary on recent research on engineering MOF nanoarchitectures for efficient electrochemical water splitting. Benefiting from the large surface area, adjustable chemical components, tunable pore structure, controllable topology, and well-defined surface functionality, various MOF-based/derived materials with excellent water splitting performance have been developed. A range of new synthetic strategies for chemical composition optimization and structural functionalization to improve the electrocatalytic performance of catalytic sites are highlighted herein, especially at the molecular and atomic scales and for tailored nanoarchitectures and configurations. Meanwhile, the fast-growing breakthroughs in catalytic activity, identification of highly active sites, fundamental mechanisms, and recent designs of electrolyzers to promote the commercialization of electrochemical hydrogen production are also fully discussed and summarized. Although abundant efforts have been devoted to this newly emerging area, and rapid and promising progress has been achieved in recent years, there are several challenges for the future engineering of high-efficiency and durable MOF-based/derived electrocatalysts for water splitting. The general comments are summarized below.

- 1) For MOF-based materials, poor electron conductivity is the biggest obstacle for electrochemical applications and needs to be further enhanced by adjusting the chemical properties and structure of the ligands to increase the electron transport and electrocatalytic reaction rate, especially for pristine MOFs. In addition to the poor conductivity, the controversial stability should also be overcome to satisfy the requirements of actual water splitting. The characterization and regulation of the synergistic effects between the functional components and MOFs remain challenges for guest@MOF and MOFs/substrates.
- 2) The high cost of ligands, harsh synthetic conditions, and limited synthetic strategies comprise the major impediment to the large-scale preparation of MOFs, which is crucial for the development of cost-effective water splitting electrocatalysts.
- 3) For MOF-derived materials, high-temperature calcination usually causes severe structural damage and the collapse of porous frameworks, which hamper the rationally controlled design of MOF derivatives and decrease the accessibility of catalytic centers and their intrinsic electrocatalytic performance.

**Table 4.** Overall water splitting performances of MOF-based/derived electrochemical catalysts.

Catalyst	HER overpotential [mV] at 10 mA cm <sup>-2</sup>	OER overpotential [mV] at 10 mA cm <sup>-2</sup>	Cell voltage [V] at 10 mA cm <sup>-2</sup>	Electrolyte
<b>MOF-based catalysts</b>				
Fe <sub>2</sub> M-MOF <sup>[12]</sup>	221 (Zn)	339 (Co)		0.1 M KOH
NiFe-MOF <sup>[53]</sup>	134	240	1.550	0.1 M KOH
PBA@PANI <sup>[227]</sup>	170	330	1.730	1.0 M KOH
Ni-ZIF/Ni-B@NF <sup>[229]</sup>	67	234	1.540	1.0 M KOH
Fe <sub>2</sub> Ni-MIL-88B/NF <sup>[231]</sup>	87	240	1.560	1.0 M KOH
MFN-MOFs (2:1)/NF <sup>[232]</sup>	79	235	1.495	1.0 M KOH
<b>MOF-derived catalysts</b>				
Co/NBC-900 <sup>[65]</sup>	117	302	1.680	1.0 M KOH
Co@N-CS/N-HCP@CC <sup>[76]</sup>	66	248	1.545	1.0 M KOH
Co-NC@Mo <sub>2</sub> C <sup>[119]</sup>	99	347	1.685	1.0 M KOH
NiO/Co <sub>3</sub> O <sub>4</sub> NCMC <sup>[120]</sup>	≈169	290	1.630	1.0 M KOH
RuO <sub>2</sub> /Co <sub>3</sub> O <sub>4</sub> -RuCo@NC <sup>[121]</sup>	141	247	1.660	0.5 M H <sub>2</sub> SO <sub>4</sub>
Co/Co <sub>9</sub> S <sub>8</sub> @NSOC-800 <sup>[122]</sup>	216	373	1.560	1.0 M KOH
Co-NCNTFs//NF <sup>[234]</sup>	140	230	1.620	1.0 M KOH
CNT network <sup>[235]</sup>	133	286	1.690	1.0 M KOH
Co <sub>0.75</sub> Fe <sub>0.25</sub> -NC <sup>[236]</sup>	202	303	1.680	1.0 M KOH
PMo/ZIF-67-6-6N <sup>[237]</sup>	83	295		1.0 M KOH
CoS <sub>2</sub> <sup>[240]</sup>	196	298	1.650	1.0 M KOH
FeNiP/NCH <sup>[242]</sup>	216	250	1.590	1.0 M KOH
NiCoFeP/C <sup>[244]</sup>	149	270	1.600	1.0 M KOH
Mn-CoP NSs <sup>[245]</sup>	195	290		1.0 M KOH
CoP/NCNHP <sup>[246]</sup>	115	310	1.640	1.0 M KOH
CC-NC-NiFeP <sup>[247]</sup>	94	145	1.540	1.0 M KOH
Fe-CoP HTPAs <sup>[248]</sup>	98	230	1.590	1.0 M KOH
Fe-CoP/NF <sup>[250]</sup>	78	190	1.490	1.0 M KOH
Ni <sub>2</sub> P-NPCM-900-2 <sup>[251]</sup>	125	255	1.620	1.0 M KOH
Ni <sub>2</sub> P/rGO <sup>[252]</sup>	142	260	1.610	1.0 M KOH
Ru-CoNi@NC-2 <sup>[253]</sup>	268	240		1.0 M KOH
Co <sub>2</sub> P/Mo <sub>2</sub> C/Mo <sub>3</sub> Co <sub>3</sub> C@C <sup>[254]</sup>	182	362	1.740	1.0 M KOH
CoPS@NPS-C (4 wt%) <sup>[255]</sup>	191	320	1.620	1.0 M KOH
NG-NiFe@MoC <sub>2</sub> -2 <sup>[256]</sup>	150	320	1.530	1.0 M KOH
Co@Ir/NC-10% <sup>[257]</sup>	121	280		1.0 M KOH
Ni <sub>2</sub> P/CoN-PCP <sup>[258]</sup>	94	270	1.580	1.0 M KOH
Co-MOF/H <sub>2</sub> <sup>[260]</sup>	30	312	1.619	1.0 M KOH
Co <sub>3</sub> ZnC/Co-NCCP <sup>[261]</sup>	188	295	1.650	1.0 M KOH
Co <sub>9</sub> S <sub>8</sub> -NSC@Mo <sub>2</sub> C <sup>[262]</sup>	89	293	1.610	1.0 M KOH
Ni@Ru/CNS-10% <sup>[263]</sup>	≈20	356	1.612	1.0 M KOH
Co-Mo <sub>2</sub> N <sup>[264]</sup>	76	302	1.576	1.0 M KOH

- 4) Although other single-atom electrocatalytic systems have been used in applications for the HER and OER, MOF-derived SACs with efficient catalytic activity and stability for water splitting are rarely reported. Considering the maximum atom-utilization efficiency and low cost, the development of MOF-derived SACs is urgently required for water electrolysis.
- 5) Research on the synthetic mechanisms and characterizations of intrinsic active sites for MOF-based/derived electrocatalysts are still in the initial stage. More comprehensive

- and thorough mechanistic studies are urgently needed to guide the future rational synthesis of MOF-based/derived electrocatalysts with well-defined catalytic structures and durable activity.
- 6) For the industrialization of water splitting, numerous challenges still exist, such as the formation of explosive H<sub>2</sub>/O<sub>2</sub> gas mixtures and reactive oxygen species, the limited HER rate due to the more sluggish kinetics of the OER, as well as the lack of cost-efficient H<sub>2</sub> storage and transport systems.

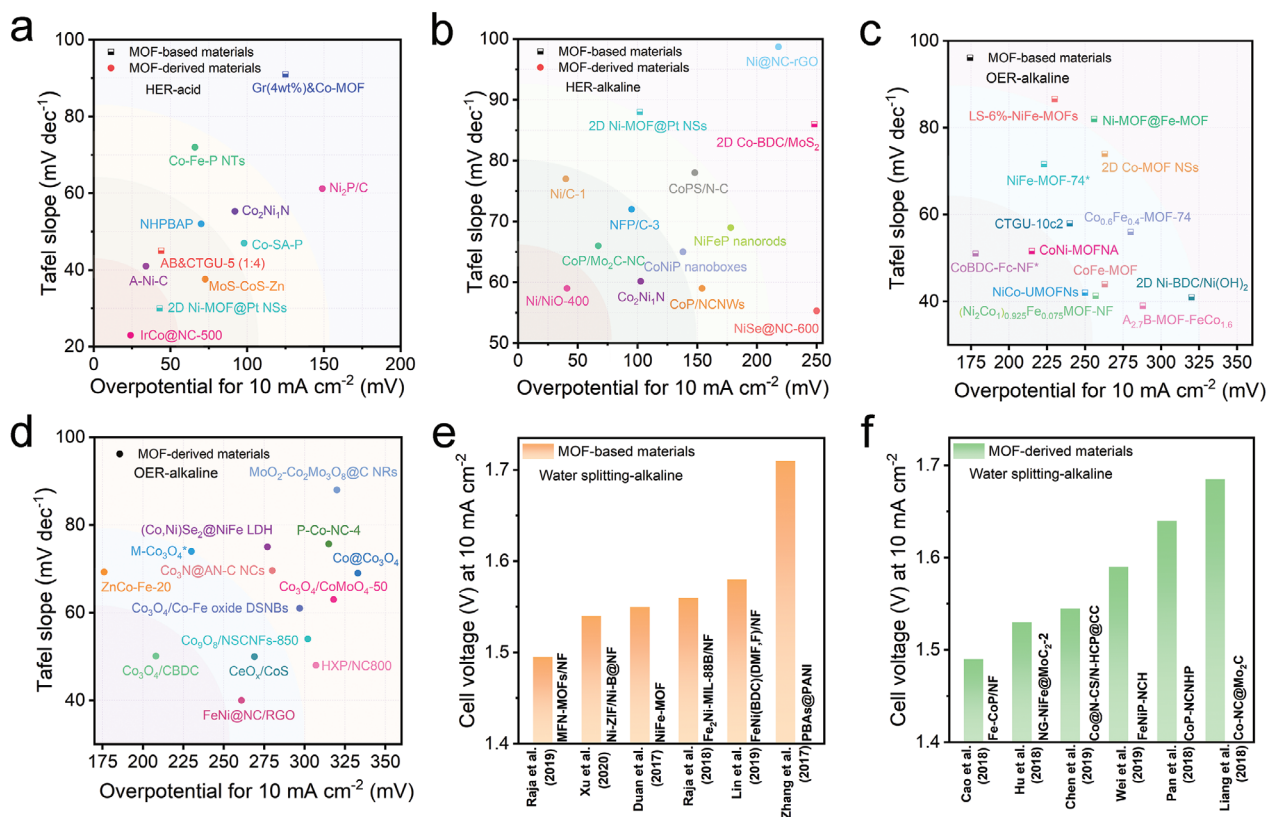


**Figure 16.** Summary and comparison of activity for water splitting. a,b) MOF-based/derived electrocatalysts for the HER in 0.5 M H<sub>2</sub>SO<sub>4</sub> (a) and 1 M KOH (b). c) MOF-based and d) MOF-derived electrocatalysts for the OER in 1 M KOH. e) MOF-based and f) MOF-derived electrocatalysts for overall water splitting in 1 M KOH.

To address the above challenges, some strategies and perspectives are detailed below.

- 1) Numerous efficient and versatile strategies have been proven to strengthen the electrocatalytic activity of pristine MOFs. For instance, incorporating nonbridging ligands into the MOF could significantly improve the electrocatalytic performance. Synthesizing the  $\pi$ -conjugated structure with transition metal atoms and aromatic organic ligands as precursors could enhance the conductivity. Converting bulk MOF crystals into 2D nanosheets could also enable the higher exposure of the active surface sites. Designing bimetallic MOFs may further optimize the electrocatalytic performance for water splitting because of the synergistic effect between the multi-metal element. Furthermore, MOFs could be combined with various functional materials (e.g., metal NPs, molecule complexes, and graphene) to achieve more exposure of the active catalytic sites, thus significantly improving the conductivity for the resulting MOF composites.
- 2) Solvothermal reactions with extra salt solutions and the synthesis of bimetallic MOFs are commonly employed strategies to introduce the second metal component into MOFs, followed by pyrolysis, to realize heteroatom doping, more accessible active sites, well-controlled nanostructures, well-designed synergistic effects, and robust structural stability. During the calcination process, the low-boiling-point metals

in the frameworks evaporate, causing the formation of additional porous structures for the MOF-derived materials.

- 3) Under porous conditions for water splitting, carbons are usually not chemically or thermodynamically stable; thus, a carbon matrix with a high level of graphitization is preferred to maintain the high conductivity of the catalysts.
- 4) With the advances in characterization techniques (e.g., XAFS, HAADF-STEM, and Raman spectroscopy) and theoretical calculations, systematic studies will provide a new perspective to identify the intrinsic catalytic active sites and many new possibilities for the rational design and performance breakthroughs in state-of-the-art water-splitting electrocatalysts.
- 5) Low-cost and high-performance non-precious electrocatalysts for overall water splitting are urgently needed to promote the development of affordable water-splitting electrolyzers, thus accelerating future industrialization. Meanwhile, new techniques to fabricate electrodes or electrolyzers are required for the rational assembly of water splitting devices for scalable and safe production or utilization of hydrogen. For instance, decoupled water electrolyzers have recently been developed to separate the HER and OER processes to avoid the formation of explosive H<sub>2</sub>/O<sub>2</sub> gas mixtures, which is usually achieved by redox mediators (Figure 17a). Due to the lack of cost-efficient hydrogen storage and transport systems, tandem water electrolysis has been developed; as shown in Figure 17b, the produced hydrogen can be converted in situ to valuable chemicals (e.g., NH<sub>3</sub>, CH<sub>4</sub>, etc.).<sup>[265]</sup>



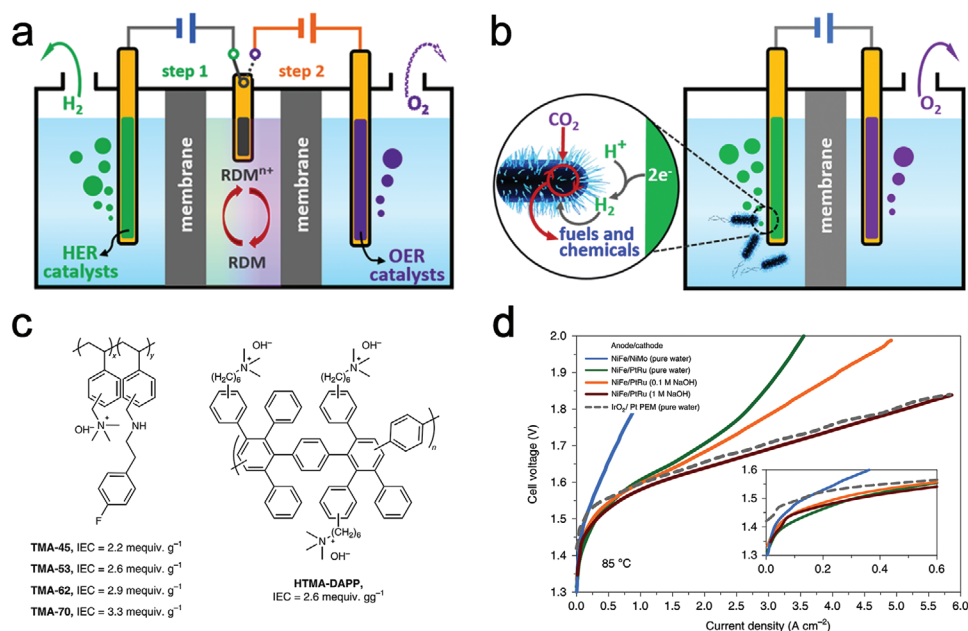


**Figure 17.** a) Decoupled water electrolyzer system. b) Tandem water electrolyzer system. a,b) Reproduced with permission.<sup>[265]</sup> Copyright 2018, American Chemical Society. c) The chemical structures of the AEM electrolytes. TMA: trimethyl ammonium functionalized polystyrenes. HTMA-DAPP: hexamethyl trimethyl ammonium-functionalized Diels–Alder polyphenylene. d) AEM electrolyzer performance that equipped with the HTMA-DAPP. c,d) Reproduced with permission.<sup>[266]</sup> Copyright 2020, Springer Nature.

6) Low-temperature water electrolyzer systems can use either a proton exchange membrane (PEM) or alkaline anion exchange membrane (AEM) as the electrolyte. Nevertheless, the high capital cost of the cell stack and the large noble metal loading amount required for the electrodes are notable disadvantages for the PEM-based electrolyzer. It has been found that alkaline AEM electrolysis can offer the possibility of replacing the PEM-based electrolyzer, including the possible use of noble metal-free catalysts, without significant loss of catalytic performance. For instance, Li et al. recently reported several quaternized polystyrene electrode binders, which show excellent activity for the HER and OER in AEM electrolyzers.<sup>[266]</sup> The electrolyzer of the NiFe-anode-catalyzed device showed excellent operational performance comparable to that of a state-of-the-art PEM electrolyzer using noble metals (Figure 17c,d).

In summary, from a practical standpoint, the development of low-cost and high-efficiency electrocatalysts is crucial to address the challenges, both in water splitting and other energy devices, for overcoming the ever-growing energy crisis and environmental concerns. We hope that this review will advance the rapid exploration of MOF-based/derived electrocatalysts for water splitting. Furthermore, we anticipate that, with the development of inexpensive and efficient electrocatalysts, a new technological revolution will take place in the field of electrochemical hydrogen production in the not-too-distant future.

## Acknowledgements

B.Z. and Y.J.Z. contributed equally to this paper. This work was financially supported by the National Key R&D Program of China (2019YFA0110600

and 2019YFA0110601), National Natural Science Foundation of China (Nos. 82071938, 82001824, 51903178, 81971622, 51803134, and 51703141), the Science and Technology Project of Sichuan Province (Nos. 2020YFH0087, 2020YJ0055, 2019YFS0219, and 18YYJC1417), Special Funds for Prevention and Control of COVID-19 of Sichuan University (2020scunCoV-YJ-20005) and SKLFPM, Donghua University (YJ202005), and the Post-Doctor Research Project, West China Hospital, Sichuan University (No. 2018HXBH077). C.C. acknowledges the support of the State Key Laboratory of Polymer Materials Engineering (No. sklpm2019-2-03), Fundamental Research Funds for the Central Universities, Thousand Youth Talents Plan, and Alexander von Humboldt Fellowship. The authors thank their laboratory members for their generous help, and gratefully acknowledge Dr. Chao He for the analytical support, Sichuan University.

Open access funding enabled and organized by Projekt DEAL.

## Conflict of Interest

The authors declare no conflict of interest.

## Keywords

electrocatalytic nanostructures and electrocatalysts, hydrogen evolution reaction, metal–organic frameworks, oxygen evolution reaction, water splitting

Received: September 4, 2020  
Revised: October 18, 2020  
Published online: March 22, 2021

- [1] S. Roy, Z. Huang, A. Bhunia, A. Castner, A. K. Gupta, X. Zou, S. Ott, *J. Am. Chem. Soc.* **2019**, *141*, 15942.
- [2] D. D. Huang, S. Li, Y. P. Wu, J. H. Wei, J. W. Yi, H. M. Ma, Q. C. Zhang, Y. L. Liu, D. S. Li, *Chem. Commun.* **2019**, *55*, 4570.
- [3] J. Yin, J. Jin, H. Lin, Z. Yin, J. Li, M. Lu, L. Guo, P. Xi, Y. Tang, C. H. Yan, *Adv. Sci.* **2020**, *7*, 1903070.

- [4] B. You, M. T. Tang, C. Tsai, F. A. Pedersen, X. Zheng, H. Li, *Adv. Mater.* **2019**, *31*, 1807001.
- [5] J. Zhang, Q. Zhang, X. Feng, *Adv. Mater.* **2019**, *31*, 1808167.
- [6] H. Sun, Z. Yan, F. Liu, W. Xu, F. Cheng, J. Chen, *Adv. Mater.* **2020**, *32*, 1806326.
- [7] J. Yu, Q. He, G. Yang, W. Zhou, Z. Shao, M. Ni, *ACS Catal.* **2019**, *9*, 9973.
- [8] J. W. Tian, M. X. Fu, D. D. Huang, X. K. Wang, Y. P. Wu, J. Y. Lu, D.-S. Li, *Inorg. Chem. Commun.* **2018**, *95*, 73.
- [9] Y. Li, Y. Sun, Y. Qin, W. Zhang, L. Wang, M. Luo, H. Yang, S. Guo, *Adv. Energy Mater.* **2020**, *10*, 1903120.
- [10] W.-T. Koo, J.-S. Jang, I.-D. Kim, *Chem* **2019**, *5*, 1938.
- [11] Y. Yang, X. Wu, C. He, J. Huang, S. Yin, M. Zhou, L. Ma, W. Zhao, L. Qiu, C. Cheng, C. Zhao, *ACS Appl. Mater. Interfaces* **2020**, *12*, 13698.
- [12] M. Gu, S. C. Wang, C. Chen, D. Xiong, F. Y. Yi, *Inorg. Chem.* **2020**, *59*, 6078.
- [13] S. G. Tarrino, J. L. O. Sariego, J. J. Calvente, M. Palomino, G. M. Espallargas, J. L. Jorda, F. Rey, P. O. Burgos, *ACS Appl. Mater. Interfaces* **2019**, *11*, 46658.
- [14] Z. Xue, K. Liu, Q. Liu, Y. Li, M. Li, C.-Y. Su, N. Ogiwara, H. Kobayashi, H. Kitagawa, M. Liu, G. Li, *Nat. Commun.* **2019**, *10*, 5048.
- [15] W. Pang, B. Shao, X.-Q. Tan, C. Tang, Z. Zhang, J. Huang, *Nanoscale* **2020**, *12*, 3623.
- [16] W. Zhang, Y. Wang, H. Zheng, R. Li, Y. Tang, B. Li, C. Zhu, L. You, M. R. Gao, Z. Liu, S. H. Yu, K. Zhou, *ACS Nano* **2020**, *14*, 1971.
- [17] H. Huang, Y. Zhao, Y. Bai, F. Li, Y. Zhang, Y. Chen, *Adv. Sci.* **2020**, *7*, 2000012.
- [18] M. Khalid, A. Hassan, A. M. B. Honorato, F. N. Crespilho, H. Varela, *Chem. Commun.* **2018**, *54*, 11048.
- [19] W. Zhou, Y. P. Wu, X. Wang, J. W. Tian, D. D. Huang, J. Zhao, Y. Q. Lan, D. S. Li, *CrystEngComm* **2018**, *20*, 4804.
- [20] K. Rui, G. Zhao, M. Lao, P. Cui, X. Zheng, X. Zheng, J. Zhu, W. Huang, S. X. Dou, W. Sun, *Nano Lett.* **2019**, *19*, 8447.
- [21] C. Cao, D.-D. Ma, Q. Xu, X.-T. Wu, Q.-L. Zhu, *Adv. Funct. Mater.* **2019**, *29*, 1807418.
- [22] W. Shao, C. He, M. Zhou, C. Yang, Y. Gao, S. Li, L. Ma, L. Qiu, C. Cheng, C. Zhao, *J. Mater. Chem. A* **2020**, *8*, 3168.
- [23] L. Ye, Y. Ying, D. Sun, Z. Zhang, L. Fei, Z. Wen, J. Qiao, H. Huang, *Angew. Chem., Int. Ed.* **2020**, *59*, 3244.
- [24] B. Li, K. Igawa, J. Chai, Y. Chen, Y. Wang, D. W. Fam, N. N. Tham, T. An, T. Konno, A. Sng, Z. Liu, H. Zhang, Y. Zong, *Energy Storage Mater.* **2020**, *25*, 137.
- [25] Y. Hao, Y. Xu, W. Liu, X. Sun, *Mater. Horiz.* **2018**, *5*, 108.
- [26] L. Qin, Z. Xu, Y. Zheng, C. Li, J. Mao, G. Zhang, *Adv. Funct. Mater.* **2020**, *30*, 1910257.
- [27] T. Al-Zoubi, Y. Zhou, X. Yin, B. Janicek, C. Sun, C. E. Schulz, X. Zhang, A. A. Gewirth, P. Huang, P. Zelenay, H. Yang, *J. Am. Chem. Soc.* **2020**, *142*, 5477.
- [28] Y. Yang, Y. Deng, J. Huang, X. Fan, C. Cheng, C. Nie, L. Ma, W. Zhao, C. Zhao, *Adv. Funct. Mater.* **2019**, *29*, 1900143.
- [29] C. Yang, M. Zhou, C. He, Y. Gao, S. Li, X. Fan, Y. Lin, F. Cheng, P. Zhu, C. Cheng, *Nano-Micro Lett.* **2019**, *11*, 87.
- [30] S. Li, C. Cheng, A. Sagaltchik, P. Pachfule, C. Zhao, A. Thomas, *Adv. Funct. Mater.* **2019**, *29*, 1807419.
- [31] E. A. Flugel, V. W. Lau, H. Schlomberg, R. Glaum, B. V. Lotsch, *Chem. - Eur. J.* **2016**, *22*, 3676.
- [32] M. Jahan, Z. Liu, K. P. Loh, *Adv. Funct. Mater.* **2013**, *23*, 5363.
- [33] X. Dai, M. Liu, Z. Li, A. Jin, Y. Ma, X. Huang, H. Sun, H. Wang, X. Zhang, *J. Phys. Chem. C* **2016**, *120*, 12539.
- [34] S. Zhao, Y. Wang, J. Dong, C.-T. He, H. Yin, P. An, K. Zhao, X. Zhang, C. Gao, L. Zhang, J. Lv, J. Wang, J. Zhang, A. M. Khattak, N. A. Khan, Z. Wei, J. Zhang, S. Liu, H. Zhao, Z. Tang, *Nat. Energy* **2016**, *1*, 16184.
- [35] Q. Qian, Y. Li, Y. Liu, L. Yu, G. Zhang, *Adv. Mater.* **2019**, *31*, 1901139.
- [36] K. Hendrickx, D. E. Vanpoucke, K. Leus, K. Lejaeghere, A. van Yperen-De Deyne, V. van Speybroeck, P. van der Voort, K. Hemelsoet, *Inorg. Chem.* **2015**, *54*, 10701.
- [37] M. A. Syzgantseva, N. F. Stepanov, O. A. Syzgantseva, *ACS Appl. Mater. Interfaces* **2020**, *12*, 17611.
- [38] A. de Vos, K. Hendrickx, P. van der Voort, V. van Speybroeck, K. Lejaeghere, *Chem. Mater.* **2017**, *29*, 3006.
- [39] X. Zheng, G. Jia, G. Fan, W. Luo, Z. Li, Z. Zou, *Small* **2020**, *16*, 2003630.
- [40] N. Tsumori, L. Chen, Q. Wang, Q. L. Zhu, M. Kitta, Q. Xu, *Chem* **2018**, *4*, 845.
- [41] D. Huo, F. Lin, S. Chen, Y. Ni, R. Wang, H. Chen, L. Duan, Y. Ji, A. Zhou, L. Tong, *Inorg. Chem.* **2020**, *59*, 2379.
- [42] B. An, L. Zeng, M. Jia, Z. Li, Z. Lin, Y. Song, Y. Zhou, J. Cheng, C. Wang, W. Lin, *J. Am. Chem. Soc.* **2017**, *139*, 17747.
- [43] T. Wang, L. Gao, J. Hou, S. J. A. Herou, J. T. Griffiths, W. Li, J. Dong, S. Gao, M. M. Titirici, R. V. Kumar, A. K. Cheetham, X. Bao, Q. Fu, S. K. Smoukov, *Nat. Commun.* **2019**, *10*, 1340.
- [44] L. Zhang, S. Li, C. J. G. Garcia, H. Ma, C. Zhang, H. Pang, B. Li, *ACS Appl. Mater. Interfaces* **2018**, *10*, 31498.
- [45] G. Zhan, H. C. Zeng, *Adv. Funct. Mater.* **2016**, *26*, 3268.
- [46] H. Yin, S. Zhao, K. Zhao, A. Muqsit, H. Tang, L. Chang, H. Zhao, Y. Gao, Z. Tang, *Nat. Commun.* **2015**, *6*, 6430.
- [47] S. Lin, Y. Pineda-Galvan, W. A. Maza, C. C. Epley, J. Zhu, M. C. Kessinger, Y. Pushkar, A. J. Morris, *ChemSusChem* **2017**, *10*, 514.
- [48] S. Mukhopadhyay, O. Basu, S. K. Das, *ChemCatChem* **2020**, *12*, 5430.
- [49] S. Mukhopadhyay, O. Basu, A. Kar, S. K. Das, *Inorg. Chem.* **2020**, *59*, 472.
- [50] G. Paille, M. G. Mingot, C. R. Marchal, B. Lassalle Kaiser, P. Mialane, M. Fontecave, C. M. Draznieks, A. Dolbecq, *J. Am. Chem. Soc.* **2018**, *140*, 3613.
- [51] C. T. Buru, A. E. P. Prats, D. G. Chica, M. G. Kanatzidis, K. W. Chapman, O. K. Farha, *J. Mater. Chem. A* **2018**, *6*, 7389.
- [52] X. Ma, K. Qi, S. Wei, L. Zhang, X. Cui, *J. Alloys Compd.* **2019**, *770*, 236.
- [53] J. Duan, S. Chen, C. Zhao, *Nat. Commun.* **2017**, *8*, 1.
- [54] W. Cheng, X. Zhao, H. Su, F. Tang, W. Che, H. Zhang, Q. Liu, *Nat. Energy* **2019**, *4*, 115.
- [55] B. Liu, H. Shioyama, T. Akita, Q. Xu, *J. Am. Chem. Soc.* **2008**, *130*, 5390.
- [56] Y. Zhao, R. Nakamura, K. Kamiya, S. Nakanishi, K. Hashimoto, *Nat. Commun.* **2013**, *4*, 2390.
- [57] J. Zhang, Z. Zhao, Z. Xia, L. Dai, *Nat. Nanotechnol.* **2015**, *10*, 444.
- [58] H. Jiang, J. Gu, X. Zheng, M. Liu, X. Qiu, L. Wang, W. Li, Z. Chen, X. Ji, J. Li, *Energy Environ. Sci.* **2019**, *12*, 322.
- [59] Y. Zheng, Y. Jiao, Y. Zhu, L. H. Li, Y. Han, Y. Chen, A. Du, M. Jaroniec, S. Z. Qiao, *Nat. Commun.* **2014**, *5*, 3783.
- [60] Y. Lei, L. Wei, S. Zhai, Y. Wang, H. E. Karahan, X. Chen, Z. Zhou, C. Wang, X. Sui, Y. Chen, *Mater. Chem. Front.* **2018**, *2*, 102.
- [61] N. Cheng, L. Ren, X. Xu, Y. Du, S. X. Dou, *Adv. Energy Mater.* **2018**, *8*, 1801257.
- [62] X. Fan, F. Yang, J. Huang, Y. Yang, C. Nie, W. Zhao, L. Ma, C. Cheng, C. Zhao, R. Haag, *Nano Lett.* **2019**, *19*, 5885.
- [63] H. Liu, J. Guan, S. Yang, Y. Yu, R. Shao, Z. Zhang, M. Dou, F. Wang, Q. Xu, *Adv. Mater.* **2020**, *32*, 2003649.
- [64] H. Sun, Y. Lian, C. Yang, L. Xiong, P. Qi, Q. Mu, X. Zhao, J. Guo, Z. Deng, Y. Peng, *Energy Environ. Sci.* **2018**, *11*, 2363.
- [65] M. R. Liu, Q. L. Hong, Q. H. Li, Y. Du, H. X. Zhang, S. Chen, T. Zhou, J. Zhang, *Adv. Funct. Mater.* **2018**, *28*, 1801136.
- [66] A. Shivantham, P. Ganesan, L. Estevez, B. P. McGrail, R. K. Motkuri, S. Shanmugam, *Adv. Energy Mater.* **2018**, *8*, 1702838.
- [67] X. Zhang, J. Luo, H. F. Lin, P. Tang, J. R. Morante, J. Arbiol, K. Wan, B. W. Mao, L. M. Liu, J. Fransaer, *Energy Storage Mater.* **2019**, *17*, 46.

- [68] M. Zhang, Q. Dai, H. Zheng, M. Chen, L. Dai, *Adv. Mater.* **2018**, 30, 1705431.
- [69] X. Wu, G. Meng, W. Liu, T. Li, Q. Yang, X. Sun, J. Liu, *Nano Res.* **2017**, 11, 163.
- [70] T. Qiu, Z. Liang, W. Guo, S. Gao, C. Qu, H. Tabassum, H. Zhang, B. Zhu, R. Zou, Y. Shao-Horn, *Nano Energy* **2019**, 58, 1.
- [71] Z. Chen, R. Wu, Y. Liu, Y. Ha, Y. Guo, D. Sun, M. Liu, F. Fang, *Adv. Mater.* **2018**, 30, 1802011.
- [72] Y. Wu, X. Qiu, F. Liang, Q. Zhang, A. Koo, Y. Dai, Y. Lei, X. Sun, *Appl. Catal., B* **2019**, 241, 407.
- [73] Y. Li, B. Jia, Y. Fan, K. Zhu, G. Li, C.-Y. Su, *Adv. Energy Mater.* **2018**, 8, 1702048.
- [74] T. Wang, Z. Kou, S. Mu, J. Liu, D. He, I. S. Amiinu, W. Meng, K. Zhou, Z. Luo, S. Chaemchuen, F. Verpoort, *Adv. Funct. Mater.* **2018**, 28, 1705048.
- [75] X. Huang, Y. Zhang, H. Shen, W. Li, T. Shen, Z. Ali, T. Tang, S. Guo, Q. Sun, Y. Hou, *ACS Energy Lett.* **2018**, 3, 2914.
- [76] Z. Chen, Y. Ha, H. Jia, X. Yan, M. Chen, M. Liu, R. Wu, *Adv. Energy Mater.* **2019**, 9, 1803918.
- [77] J. Wu, L. Hu, N. Wang, Y. Li, D. Zhao, L. Li, X. Peng, Z. Cui, L. J. Ma, Y. Tian, X. Wang, *Appl. Catal., B* **2019**, 254, 55.
- [78] C. Guan, A. Sumboja, W. Zang, Y. Qian, H. Zhang, X. Liu, Z. Liu, D. Zhao, S. J. Pennycook, J. Wang, *Energy Storage Mater.* **2019**, 16, 243.
- [79] W. Zhang, X. Yao, S. Zhou, X. Li, L. Li, Z. Yu, L. Gu, *Small* **2018**, 14, 1800423.
- [80] Y. Zhao, Q. Lai, J. Zhu, J. Zhong, Z. Tang, Y. Luo, Y. Liang, *Small* **2018**, 14, 1704207.
- [81] H. Chen, K. Shen, Y. Tan, Y. Li, *ACS Nano* **2019**, 13, 7800.
- [82] F. Bu, W. Chen, J. Gu, P. O. Agboola, N. F. Al-Khalli, I. Shakir, Y. Xu, *Chem. Sci.* **2018**, 9, 7009.
- [83] C. Wang, H. Yang, Y. Zhang, Q. Wang, *Angew. Chem., Int. Ed.* **2019**, 58, 6099.
- [84] C. Zhang, H. Yang, D. Zhong, Y. Xu, Y. Wang, Q. Yuan, Z. Liang, B. Wang, W. Zhang, H. Zheng, T. Cheng, R. Cao, *J. Mater. Chem. A* **2020**, 8, 9536.
- [85] C. C. Hou, L. Zou, Q. Xu, *Adv. Mater.* **2019**, 31, 1904689.
- [86] Y. Xiong, Y. Yang, F. J. DiSalvo, H. D. Abruna, *J. Am. Chem. Soc.* **2019**, 141, 10744.
- [87] P. Jiang, J. Chen, C. Wang, K. Yang, S. Gong, S. Liu, Z. Lin, M. Li, G. Xia, Y. Yang, J. Su, Q. Chen, *Adv. Mater.* **2018**, 30, 1705324.
- [88] H. Ning, G. Li, Y. Chen, K. Zhang, Z. Gong, R. Nie, W. Hu, Q. Xia, *ACS Appl. Mater. Interfaces* **2019**, 11, 1957.
- [89] Z. Li, H. He, H. Cao, S. Sun, W. Diao, D. Gao, P. Lu, S. Zhang, Z. Guo, M. Li, R. Liu, D. Ren, C. Liu, Y. Zhang, Z. Yang, J. Jiang, G. Zhang, *Appl. Catal., B* **2019**, 240, 112.
- [90] X. F. Lu, L. Yu, J. Zhang, X. W. D. Lou, *Adv. Mater.* **2019**, 31, 1900699.
- [91] C. Song, S. Wu, X. Shen, X. Miao, Z. Ji, A. Yuan, K. Xu, M. Liu, X. Xie, L. Kong, *J. Colloid Interface Sci.* **2018**, 524, 93.
- [92] M. Khalid, A. M. B. Honorato, H. Varela, L. Dai, *Nano Energy* **2018**, 45, 127.
- [93] P. Deng, F. Yang, Z. Wang, S. Chen, Y. Zhou, S. Zaman, B. Y. Xia, *Angew. Chem., Int. Ed.* **2020**, 59, 10807.
- [94] B. K. Kang, S. Y. Im, J. Lee, S. H. Kwag, S. B. Kwon, S. Tiruneh, M.-J. Kim, J. H. Kim, W. S. Yang, B. Lim, D. H. Yoon, *Nano Res.* **2019**, 12, 1605.
- [95] J. S. Li, S. Zhang, J. Q. Sha, H. Wang, M. Z. Liu, L. X. Kong, G. D. Liu, *ACS Appl. Mater. Interfaces* **2018**, 10, 17140.
- [96] K. Wang, C. Wu, F. Wang, G. Jiang, *ACS Appl. Nano Mater.* **2018**, 1, 5843.
- [97] J. S. Li, J. Y. Li, X. R. Wang, S. Zhang, J. Q. Sha, G. D. Liu, *ACS Sustainable Chem. Eng.* **2018**, 6, 10252.
- [98] M. Kong, H. Song, J. Zhou, *Adv. Energy Mater.* **2018**, 8, 1801489.
- [99] R. Wang, X. Y. Dong, J. Du, J. Y. Zhao, S. Q. Zang, *Adv. Mater.* **2018**, 30, 1703711.
- [100] Y. Yu, X. Qiu, X. Zhang, Z. Wu, H. Wang, W. Wang, Z. Wang, H. Tan, Z. Peng, X. Guo, H. Liu, *Electrochim. Acta* **2019**, 299, 423.
- [101] Y. Ma, Y. Ma, D. Bresser, Y. Ji, D. Geiger, U. Kaiser, C. Streb, A. Varzi, S. Passerini, *ACS Nano* **2018**, 12, 7220.
- [102] W. Li, B. Yu, Y. Hu, X. Wang, D. Yang, Y. Chen, *ACS Sustainable Chem. Eng.* **2019**, 7, 4351.
- [103] L. L. Wu, Q. S. Wang, J. Li, Y. Long, Y. Liu, S. Y. Song, H. J. Zhang, *Small* **2018**, 14, 1704035.
- [104] W. Hong, M. Kitta, Q. Xu, *Small Methods* **2018**, 2, 1800214.
- [105] X. F. Lu, L. Yu, X. W. D. Lou, *Sci. Adv.* **2019**, 5, eaav6009.
- [106] H. Jin, J. Chen, S. Mao, Y. Wang, *ACS Appl. Mater. Interfaces* **2018**, 10, 22094.
- [107] J. Chen, J. Liu, J. Q. Xie, H. Ye, X. Z. Fu, R. Sun, C. P. Wong, *Nano Energy* **2019**, 56, 225.
- [108] S. Luo, X. Li, M. Wang, X. Zhang, W. Gao, S. Su, G. Liu, M. Luo, *J. Mater. Chem. A* **2020**, 8, 5647.
- [109] Z. Q. Liu, T. Ouyang, X. T. Wang, X. Q. Mai, A. N. Chen, Z. Y. Tang, *Angew. Chem., Int. Ed.* **2020**, 59, 11948.
- [110] Z. Bai, S. Li, J. Fu, Q. Zhang, F. Chang, L. Yang, J. Lu, Z. Chen, *Nano Energy* **2019**, 58, 680.
- [111] P. Zhang, X. F. Lu, D. Luan, X. W. Lou, *Angew. Chem., Int. Ed.* **2020**, 132, 8025.
- [112] Y. Fu, W. Wang, J. Wang, X. Li, R. Shi, O. Peng, B. N. Chandrashekar, K. Liu, A. Amini, C. Cheng, *J. Mater. Chem. A* **2019**, 7, 17299.
- [113] Z. Li, S. Wang, Y. Tian, B. Li, H. J. Yan, S. Zhang, Z. Liu, Q. Zhang, Y. Lin, L. Chen, *Chem. Commun.* **2020**, 56, 1749.
- [114] Z. Zhuang, Y. Wang, C. Q. Xu, S. Liu, C. Chen, Q. Peng, Z. Zhuang, H. Xiao, Y. Pan, S. Lu, R. Yu, W. C. Cheong, X. Cao, K. Wu, K. Sun, Y. Wang, D. Wang, J. Li, Y. Li, *Nat. Commun.* **2019**, 10, 4875.
- [115] J. Lai, B. Huang, Y. Chao, X. Chen, S. Guo, *Adv. Mater.* **2019**, 31, 1805541.
- [116] Y. Jiang, Y.-P. Deng, J. Fu, D. U. Lee, R. Liang, Z. P. Cano, Y. Liu, Z. Bai, S. Hwang, L. Yang, D. Su, W. Chu, Z. Chen, *Adv. Energy Mater.* **2018**, 8, 1702900.
- [117] X. Zhao, P. Pachfule, S. Li, J. R. J. Simke, J. Schmidt, A. Thomas, *Angew. Chem., Int. Ed.* **2018**, 57, 8921.
- [118] X. Liu, W. Li, X. Zhao, Y. Liu, C. W. Nan, L. Z. Fan, *Adv. Funct. Mater.* **2019**, 29, 1901510.
- [119] Q. Liang, H. Jin, Z. Wang, Y. Xiong, S. Yuan, X. Zeng, D. He, S. Mu, *Nano Energy* **2019**, 57, 746.
- [120] X. Wei, Y. Zhang, H. He, D. Gao, J. Hu, H. Peng, L. Peng, S. Xiao, P. Xiao, *Chem. Commun.* **2019**, 55, 6515.
- [121] Z. Fan, J. Jiang, L. Ai, Z. Shao, S. Liu, *ACS Appl. Mater. Interfaces* **2019**, 11, 47894.
- [122] J. Du, R. Wang, Y. R. Lv, Y. L. Wei, S.-Q. Zang, *Chem. Commun.* **2019**, 55, 3203.
- [123] Y. Yang, K. Mao, S. Gao, H. Huang, G. Xia, Z. Lin, P. Jiang, C. Wang, H. Wang, Q. Chen, *Adv. Mater.* **2018**, 30, 1801732.
- [124] E. Zhang, T. Wang, K. Yu, J. Liu, W. Chen, A. Li, H. Rong, R. Lin, S. Ji, X. Zheng, Y. Wang, L. Zheng, C. Chen, D. Wang, J. Zhang, Y. Li, *J. Am. Chem. Soc.* **2019**, 141, 16569.
- [125] J. Li, H. Zhang, W. Samarakoon, W. Shan, D. A. Cullen, S. Karakalos, M. Chen, D. Gu, K. L. More, G. Wang, Z. Feng, Z. Wang, G. Wu, *Angew. Chem., Int. Ed.* **2019**, 58, 18971.
- [126] J. Yang, Z. Qiu, C. Zhao, W. Wei, W. Chen, Z. Li, Y. Qu, J. Dong, J. Luo, Z. Li, Y. Wu, *Angew. Chem., Int. Ed.* **2018**, 57, 14095.
- [127] Y. N. Gong, L. Jiao, Y. Qian, C. Y. Pan, L. Zheng, X. Cai, B. Liu, S. H. Yu, H. L. Jiang, *Angew. Chem., Int. Ed.* **2020**, 59, 2705.
- [128] X. Han, X. Ling, Y. Wang, T. Ma, C. Zhong, W. Hu, Y. Deng, *Angew. Chem., Int. Ed.* **2019**, 58, 5359.
- [129] X. Wang, Z. Chen, X. Zhao, Z. Yao, W. Chen, R. You, C. Zhao, G. Wu, J. Wang, W. Huang, J. Yang, X. Hong, S. Wei, Y. Wu, Y. Li, *Angew. Chem., Int. Ed.* **2018**, 57, 1944.
- [130] L. Jiao, G. Wan, R. Zhang, H. Zhou, S. H. Yu, H. L. Jiang, *Angew. Chem., Int. Ed.* **2018**, 57, 8525.



- [131] Z. Geng, Y. Liu, X. Kong, P. Li, K. Li, Z. Liu, J. Du, M. Shu, R. Si, J. Zeng, *Adv. Mater.* **2018**, *30*, 1803498.
- [132] W. Chen, J. Pei, C. T. He, J. Wan, H. Ren, Y. Wang, J. Dong, K. Wu, W. C. Cheong, J. Mao, X. Zheng, W. Yan, Z. Zhuang, C. Chen, Q. Peng, D. Wang, Y. Li, *Adv. Mater.* **2018**, *30*, 1800396.
- [133] H. Tao, C. Choi, L.-X. Ding, Z. Jiang, Z. Han, M. Jia, Q. Fan, Y. Gao, H. Wang, A. W. Robertson, S. Hong, Y. Jung, S. Liu, Z. Sun, *Chem* **2019**, *5*, 204.
- [134] W. Ye, S. Chen, Y. Lin, L. Yang, S. Chen, X. Zheng, Z. Qi, C. Wang, R. Long, M. Chen, *Chem* **2019**, *5*, 2865.
- [135] L. Chen, Y. Zhang, L. Dong, W. Yang, X. Liu, L. Long, C. Liu, S. Dong, J. Jia, *J. Mater. Chem. A* **2020**, *8*, 4369.
- [136] M. Xiao, L. Gao, Y. Wang, X. Wang, J. Zhu, Z. Jin, C. Liu, H. Chen, G. Li, J. Ge, Q. He, Z. Wu, Z. Chen, W. Xing, *J. Am. Chem. Soc.* **2019**, *141*, 19800.
- [137] C. C. Hou, L. Zou, L. Sun, K. Zhang, Z. Liu, Y. Li, C. Li, R. Zou, J. Yu, Q. Xu, *Angew. Chem., Int. Ed.* **2020**, *59*, 7384.
- [138] Y. Xiong, J. Dong, Z. Q. Huang, P. Xin, W. Chen, Y. Wang, Z. Li, Z. Jin, W. Xing, Z. Zhuang, J. Ye, X. Wei, R. Cao, L. Gu, S. Sun, L. Zhuang, X. Chen, H. Yang, C. Chen, Q. Peng, C. R. Chang, D. Wang, Y. Li, *Nat. Nanotechnol.* **2020**, *15*, 390.
- [139] Q. Liu, Y. Li, L. Zheng, J. Shang, X. Liu, R. Yu, J. Shui, *Adv. Energy Mater.* **2020**, *10*, 2000689.
- [140] L. Fan, P. F. Liu, X. Yan, L. Gu, Z. Z. Yang, H. G. Yang, S. Qiu, X. Yao, *Nat. Commun.* **2016**, *7*, 10667.
- [141] S. Mitchell, E. Vorobyeva, J. Perez-Ramirez, *Angew. Chem., Int. Ed.* **2018**, *57*, 15316.
- [142] Y. Wu, X. Tao, Y. Qing, H. Xu, F. Yang, S. Luo, C. Tian, M. Liu, X. Lu, *Adv. Mater.* **2019**, *31*, 1900178.
- [143] S. L. Zhang, B. Y. Guan, X. F. Lu, S. Xi, Y. Du, X. W. D. Lou, *Adv. Mater.* **2020**, *32*, 2002235.
- [144] A. Mohajeri, N. L. Dashti, *J. Phys. Chem. C* **2019**, *123*, 30972.
- [145] Y. Sun, L. Silvioli, N. R. Sahrarie, W. Ju, J. Li, A. Zitolo, S. Li, A. Bagger, L. Arnarson, X. Wang, *J. Am. Chem. Soc.* **2019**, *141*, 12372.
- [146] H. Yang, Q. Lin, Y. Wu, G. Li, Q. Hu, X. Chai, X. Ren, Q. Zhang, J. Liu, C. He, *Nano Energy* **2020**, *70*, 104454.
- [147] Y. P. Wu, W. Zhou, J. Zhao, W. W. Dong, Y. Q. Lan, D. S. Li, C. Sun, X. Bu, *Angew. Chem., Int. Ed.* **2017**, *56*, 13001.
- [148] Z. Ji, C. Trickett, X. Pei, O. M. Yaghi, *J. Am. Chem. Soc.* **2018**, *140*, 13618.
- [149] X. Huang, H. Yao, Y. Cui, W. Hao, J. Zhu, W. Xu, D. Zhu, *ACS Appl. Mater. Interfaces* **2017**, *9*, 40752.
- [150] Y. Ji, H. Dong, C. Liu, Y. Li, *Nanoscale* **2019**, *11*, 454.
- [151] C. A. Downes, A. J. Clough, K. Chen, J. W. Yoo, S. C. Marinescu, *ACS Appl. Mater. Interfaces* **2018**, *10*, 1719.
- [152] X. Sun, K.-H. Wu, R. Sakamoto, T. Kusamoto, H. Maeda, X. Ni, W. Jiang, F. Liu, S. Sasaki, H. Masunaga, H. Nishihara, *Chem. Sci.* **2017**, *8*, 8078.
- [153] T. Qiu, Z. Liang, W. Guo, H. Tabassum, S. Gao, R. Zou, *ACS Energy Lett.* **2020**, *5*, 520.
- [154] D. Zhu, J. Liu, Y. Zhao, Y. Zheng, S.-Z. Qiao, *Small* **2019**, *15*, 1805511.
- [155] X. Wang, W. Zhou, Y. P. Wu, J. W. Tian, X. K. Wang, D. D. Huang, J. Zhao, D. S. Li, *J. Alloys Compd.* **2018**, *753*, 228.
- [156] T. Liu, P. Li, N. Yao, G. Cheng, S. Chen, W. Luo, Y. Yin, *Angew. Chem., Int. Ed.* **2019**, *58*, 4679.
- [157] S. He, S. He, X. Bo, Q. Wang, F. Zhan, Q. Wang, C. Zhao, *Mater. Lett.* **2018**, *231*, 94.
- [158] Y. Ge, P. Dong, S. R. Craig, P. M. Ajayan, M. Ye, J. Shen, *Adv. Energy Mater.* **2018**, *8*, 1800484.
- [159] M. Chu, L. Wang, X. Li, M. Hou, N. Li, Y. Dong, X. Li, Z. Xie, Y. Lin, W. Cai, C. Zhang, *Electrochim. Acta* **2018**, *264*, 284.
- [160] Y. Jiao, W. Hong, P. Li, L. Wang, G. Chen, *Appl. Catal., B* **2019**, *244*, 732.
- [161] Z. Huang, J. Liu, Z. Xiao, H. Fu, W. Fan, B. Xu, B. Dong, D. Liu, F. Dai, D. Sun, *Nanoscale* **2018**, *10*, 22758.
- [162] Y. Du, Z. Li, Y. Liu, Y. Yang, L. Wang, *Appl. Surf. Sci.* **2018**, *457*, 1081.
- [163] L. Wang, L. Ren, X. Wang, X. Feng, J. Zhou, B. Wang, *ACS Appl. Mater. Interfaces* **2018**, *10*, 4750.
- [164] Y. Cao, Y. Lu, E. H. Ang, H. Geng, X. Cao, J. Zheng, H. Gu, *Nanoscale* **2019**, *11*, 15112.
- [165] S. K. Park, Y. C. Kang, *ACS Appl. Mater. Interfaces* **2018**, *10*, 17203.
- [166] X. H. Luo, Q. Zhou, S. Du, J. Li, L. Zhang, K. Lin, H. Li, B. Chen, T. Wu, D. Chen, M. Chang, Y. Liu, *ACS Appl. Mater. Interfaces* **2018**, *10*, 42335.
- [167] Y. Li, S. Niu, D. Rakov, Y. Wang, M. Caban Acevedo, S. Zheng, B. Song, P. Xu, *Nanoscale* **2018**, *10*, 7291.
- [168] X. Feng, H. Wang, X. Bo, L. Guo, *ACS Appl. Mater. Interfaces* **2019**, *11*, 8018.
- [169] Y. Lu, Y. Deng, S. Lu, Y. Liu, J. Lang, X. Cao, H. Gu, *Nanoscale* **2019**, *11*, 21259.
- [170] J. Wan, Z. Zhao, H. Shang, B. Peng, W. Chen, J. Pei, L. Zheng, J. Dong, R. Cao, R. Sarangi, Z. Jiang, D. Zhou, Z. Zhuang, J. Zhang, D. Wang, Y. Li, *J. Am. Chem. Soc.* **2020**, *142*, 8431.
- [171] W. Zhao, G. Wan, C. Peng, H. Sheng, J. Wen, H. Chen, *ChemSusChem* **2018**, *11*, 3473.
- [172] G. Yilmaz, T. Yang, Y. Du, X. Yu, Y. P. Feng, L. Shen, G. W. Ho, *Adv. Sci.* **2019**, *6*, 19000140.
- [173] W. He, R. Ifraemov, A. Raslin, I. Hod, *Adv. Funct. Mater.* **2018**, *28*, 1707244.
- [174] S. Li, C. Cheng, X. J. Zhao, J. Schmidt, A. Thomas, *Angew. Chem., Int. Ed.* **2018**, *57*, 1856.
- [175] Z. Wei, W. Zhu, Y. Li, Y. Ma, J. Wang, N. Hu, Y. Suo, J. Wang, *Inorg. Chem.* **2018**, *57*, 8422.
- [176] Z. Jiang, L. Ge, L. Zhuang, M. Li, Z. Wang, Z. Zhu, *ACS Appl. Mater. Interfaces* **2019**, *11*, 44300.
- [177] L. Liu, Q. Wu, H. Guo, L. Li, M. Liu, D. Li, H. Wang, L. Chen, *Mater. Lett.* **2018**, *230*, 53.
- [178] V. Maruthapandian, S. Kumaraguru, S. Mohan, V. Saraswathy, S. Muralidharan, *ChemElectroChem* **2018**, *5*, 2795.
- [179] Q. Liu, L. Xie, X. Shi, G. Du, A. M. Asiri, Y. Luo, X. Sun, *Inorg. Chem. Front.* **2018**, *5*, 1570.
- [180] M. Xie, X. Xiong, L. Yang, X. Shi, A. M. Asiri, X. Sun, *Chem. Commun.* **2018**, *54*, 2300.
- [181] X. Zhang, Q. Liu, X. Shi, A. M. Asiri, X. Sun, *Inorg. Chem. Front.* **2018**, *5*, 1405.
- [182] Q. Ji, Y. Kong, C. Wang, H. Tan, H. Duan, W. Hu, G. Li, Y. Lu, N. Li, Y. Wang, J. Tian, Z. Qi, Z. Sun, F. Hu, W. Yan, *ACS Catal.* **2020**, *10*, 5691.
- [183] L. Huang, G. Gao, H. Zhang, J. Chen, Y. Fang, S. Dong, *Nano Energy* **2020**, *68*, 104296.
- [184] Y. Xu, B. Li, S. Zheng, P. Wu, J. Zhan, H. Xue, Q. Xu, H. Pang, *J. Mater. Chem. A* **2018**, *6*, 22070.
- [185] J. Huang, Y. Li, R. K. Huang, C. T. He, L. Gong, Q. Hu, L. Wang, Y. T. Xu, X. Y. Tian, S. Y. Liu, Z. M. Ye, F. Wang, D. D. Zhou, W. X. Zhang, J. P. Zhang, *Angew. Chem., Int. Ed.* **2018**, *57*, 4632.
- [186] H. Jia, Y. Yao, J. Zhao, Y. Gao, Z. Luo, P. Du, *J. Mater. Chem. A* **2018**, *6*, 1188.
- [187] X. Zhao, B. Pattengale, D. Fan, Z. Zou, Y. Zhao, J. Du, J. Huang, C. Xu, *ACS Energy Lett.* **2018**, *3*, 2520.
- [188] X. Zheng, X. Song, X. Wang, Z. Zhang, Z. Sun, Y. Guo, *New J. Chem.* **2018**, *42*, 8346.
- [189] X. L. Wang, L. Z. Dong, M. Qiao, Y. J. Tang, J. Liu, Y. Li, S. L. Li, J. X. Su, Y. Q. Lan, *Angew. Chem., Int. Ed.* **2018**, *57*, 9660.
- [190] Z. Xue, Y. Li, Y. Zhang, W. Geng, B. Jia, J. Tang, S. Bao, H.-P. Wang, Y. Fan, Z.-w. Wei, Z. Zhang, Z. Ke, G. Li, C.-Y. Su, *Adv. Energy Mater.* **2018**, *8*, 1801564.
- [191] J. Xing, K. Guo, Z. Zou, M. Cai, J. Du, C. Xu, *Chem. Commun.* **2018**, *54*, 7046.

- [192] Z. Zou, T. Wang, X. Zhao, W. J. Jiang, H. Pan, D. Gao, C. Xu, *ACS Catal.* **2019**, *9*, 7356.
- [193] F. Sun, G. Wang, Y. Ding, C. Wang, B. Yuan, Y. Lin, *Adv. Energy Mater.* **2018**, *8*, 1800584.
- [194] W. Zhou, D. D. Huang, Y. P. Wu, J. Zhao, T. Wu, J. Zhang, D. S. Li, C. Sun, P. Feng, X. Bu, *Angew. Chem., Int. Ed.* **2019**, *58*, 4227.
- [195] D. Zhu, J. Liu, L. Wang, Y. Du, Y. Zheng, K. Davey, S.-Z. Qiao, *Nanoscale* **2019**, *11*, 3599.
- [196] S. Mukhopadhyay, J. Debgupta, C. Singh, A. Kar, S. K. Das, *Angew. Chem., Int. Ed.* **2018**, *57*, 1918.
- [197] M. Liu, L. Kong, X. Wang, J. He, X. H. Bu, *Small* **2019**, *15*, 1903410.
- [198] K. Rui, G. Zhao, Y. Chen, Y. Lin, Q. Zhou, J. Chen, J. Zhu, W. Sun, W. Huang, S. X. Dou, *Adv. Funct. Mater.* **2018**, *28*, 1801554.
- [199] J. X. Wu, C. T. He, G. R. Li, J. P. Zhang, *J. Mater. Chem. A* **2018**, *6*, 19176.
- [200] G. Wei, Z. Zhou, X. Zhao, W. Zhang, C. An, *ACS Appl. Mater. Interfaces* **2018**, *10*, 23721.
- [201] D. Ding, K. Shen, X. Chen, H. Chen, J. Chen, T. Fan, R. Wu, Y. Li, *ACS Catal.* **2018**, *8*, 7879.
- [202] J. Zhou, Y. Dou, A. Zhou, L. Shu, Y. Chen, J.-R. Li, *ACS Energy Lett.* **2018**, *3*, 1655.
- [203] T. Rodenas, S. Beeg, I. Spanos, S. Neugebauer, F. Girgsdies, G. Algara-Siller, P. P. M. Schlexer, P. Jakes, N. Pfaender, M. Willinger, M. Greiner, G. Prieto, R. Schloegl, S. Heumann, *Adv. Energy Mater.* **2018**, *8*, 1802404.
- [204] Y. Zhao, G. Fan, L. Yang, Y. Lin, F. Li, *Nanoscale* **2018**, *10*, 13555.
- [205] H. Wu, J. Wang, J. Yan, Z. Wu, W. Jin, *Nanoscale* **2019**, *11*, 20144.
- [206] T. Liu, L. Zhang, Y. Tian, *J. Mater. Chem. A* **2018**, *6*, 5935.
- [207] H. Zou, B. He, P. Kuang, J. Yu, K. Fan, *ACS Appl. Mater. Interfaces* **2018**, *10*, 22311.
- [208] J. Li, S. Lu, H. Huang, D. Liu, Z. Zhuang, C. Zhong, *ACS Sustainable Chem. Eng.* **2018**, *6*, 10021.
- [209] L. Zhang, T. Mi, M. A. Ziaee, L. Liang, R. Wang, *J. Mater. Chem. A* **2018**, *6*, 1639.
- [210] Y. Li, H. Xu, H. Huang, C. Wang, L. Gao, T. Ma, *Chem. Commun.* **2018**, *54*, 2739.
- [211] Y. Wang, Z. Zhang, X. Liu, F. Ding, P. Zou, X. Wang, Q. Zhao, H. Rao, *ACS Sustainable Chem. Eng.* **2018**, *6*, 12511.
- [212] H. Xu, Z. X. Shi, Y. X. Tong, G. R. Li, *Adv. Mater.* **2018**, *30*, 1705442.
- [213] X. Wang, L. Yu, B. Y. Guan, S. Song, X. W. D. Lou, *Adv. Mater.* **2018**, *30*, 1801211.
- [214] I. S. Amiinu, X. Liu, Z. Pu, W. Li, Q. Li, J. Zhang, H. Tang, H. Zhang, S. Mu, *Adv. Funct. Mater.* **2018**, *28*, 1704638.
- [215] Y. N. Chen, Y. Guo, H. Cui, Z. Xie, X. Zhang, J. Wei, Z. Zhou, *J. Mater. Chem. A* **2018**, *6*, 9716.
- [216] J. Ban, G. Xu, L. Zhang, G. Xu, L. Yang, Z. Sun, D. Jia, *Nanoscale* **2018**, *10*, 9077.
- [217] K. Zhang, C. Qu, Z. Liang, S. Gao, H. Zhang, B. Zhu, W. Meng, E. Fu, R. Zou, *ACS Appl. Mater. Interfaces* **2018**, *10*, 30460.
- [218] Y. Lin, H. Wan, D. Wu, G. Chen, N. Zhang, X. Liu, J. Li, Y. Cao, G. Qiu, R. Ma, *J. Am. Chem. Soc.* **2020**, *142*, 7317.
- [219] X. Yang, J. Chen, W. Yang, H. Lin, X. Luo, *Inorg. Chem. Front.* **2019**, *6*, 3475.
- [220] Z. Liang, C. Zhang, H. Yuan, W. Zhang, H. Zheng, R. Cao, *Chem. Commun.* **2018**, *54*, 7519.
- [221] S. Dilpazir, H. He, Z. Li, M. Wang, P. Lu, R. Liu, Z. Xie, D. Gao, G. Zhang, *ACS Appl. Energy Mater.* **2018**, *1*, 3283.
- [222] Z. Lionet, S. Nishijima, T. H. Kim, Y. Horiuchi, S. W. Lee, M. Matsuoka, *Dalton Trans.* **2019**, *48*, 13953.
- [223] H. Xu, J. Cao, C. Shan, B. Wang, P. Xi, W. Liu, Y. Tang, *Angew. Chem., Int. Ed.* **2018**, *57*, 8654.
- [224] W. Song, X. Teng, Y. Liu, J. Wang, Y. Niu, X. He, C. Zhang, Z. Chen, *Nanoscale* **2019**, *11*, 6401.
- [225] J. G. Li, H. Sun, L. Lv, Z. Li, X. Ao, C. Xu, Y. Li, C. Wang, *ACS Appl. Mater. Interfaces* **2019**, *11*, 8106.
- [226] B. Zhang, Z. Qi, Z. Wu, Y. H. Lui, T. H. Kim, X. Tang, L. Zhou, W. Huang, S. Hu, *ACS Energy Lett.* **2019**, *4*, 328.
- [227] L. Zhang, T. Meng, B. Mao, D. Guo, J. Qin, M. Cao, *RSC Adv.* **2017**, *7*, 50812.
- [228] S. Zheng, X. Guo, H. Xue, K. Pan, C. Liu, H. Pang, *Chem. Commun.* **2019**, *55*, 10904.
- [229] H. Xu, B. Fei, G. Cai, Y. Ha, J. Liu, H. Jia, J. Zhang, M. Liu, R. Wu, *Adv. Energy Mater.* **2020**, *10*, 1902714.
- [230] C. Guo, Y. Jiao, Y. Zheng, J. Luo, K. Davey, S. Z. Qiao, *Chem* **2019**, *5*, 2429.
- [231] D. S. Raja, X. F. Chuah, S. Y. Lu, *Adv. Energy Mater.* **2018**, *8*, 1801065.
- [232] D. S. Raja, H. W. Lin, S. Y. Lu, *Nano Energy* **2019**, *57*, 1.
- [233] H. W. Lin, D. S. Raja, X. F. Chuah, C. T. Hsieh, Y. A. Chen, S. Y. Lu, *Appl. Catal., B* **2019**, *258*, 118023.
- [234] Q. Yuan, Y. Yu, Y. Gong, X. Bi, *ACS Appl. Mater. Interfaces* **2020**, *12*, 3592.
- [235] Z. Li, J. Cui, Y. Liu, J. Li, K. Liu, M. Shao, *ACS Appl. Mater. Interfaces* **2018**, *10*, 34494.
- [236] X. Feng, X. Bo, L. Guo, *J. Power Sources* **2018**, *389*, 249.
- [237] C. Chen, A. Wu, H. Yan, Y. Xiao, C. Tian, H. Fu, *Chem. Sci.* **2018**, *9*, 4746.
- [238] K. Yang, P. Xu, Z. Lin, Y. Yang, P. Jiang, C. Wang, S. Liu, S. Gong, L. Hu, Q. Chen, *Small* **2018**, *14*, 1803009.
- [239] F. Wang, K. Li, J. Li, L. M. Wolf, K. Liu, H. Zhang, *Nanoscale* **2019**, *11*, 16658.
- [240] I. K. Ahn, W. Joo, J. H. Lee, H. G. Kim, S. Y. Lee, Y. Jung, J.-Y. Kim, G. B. Lee, M. Kim, Y. C. Joo, *Sci. Rep.* **2019**, *9*, 19539.
- [241] H. Lu, Y. Zhang, Y. Huang, C. Zhang, T. Liu, *ACS Appl. Mater. Interfaces* **2018**, *11*, 3372.
- [242] Y.-S. Wei, M. Zhang, M. Kitta, Z. Liu, S. Horike, Q. Xu, *J. Am. Chem. Soc.* **2019**, *141*, 7906.
- [243] Y. Yao, N. Mahmood, L. Pan, G. Shen, R. Zhang, R. Gao, F.-e. Aleem, X. Yuan, X. Zhang, J.-J. Zou, *Nanoscale* **2018**, *10*, 21327.
- [244] X. Wei, Y. Zhang, H. He, L. Peng, S. Xiao, S. Yao, P. Xiao, *Chem. Commun.* **2019**, *55*, 10896.
- [245] Y. Li, B. Jia, B. Chen, Q. Liu, M. Cai, Z. Xue, Y. Fan, H.-P. Wang, C.-Y. Su, G. Li, *Dalton Trans.* **2018**, *47*, 14679.
- [246] Y. Pan, K. Sun, S. Liu, X. Cao, K. Wu, W. C. Cheong, Z. Chen, Y. Wang, Y. Li, Y. Liu, D. Wang, Q. Peng, C. Chen, Y. Li, *J. Am. Chem. Soc.* **2018**, *140*, 2610.
- [247] J. Bian, Z. Song, X. Li, Y. Zhang, C. Cheng, *Nanoscale* **2020**, *12*, 8443.
- [248] E. Hu, J. Ning, D. Zhao, C. Xu, Y. Lin, Y. Zhong, Z. Zhang, Y. Wang, Y. Hu, *Small* **2018**, *14*, 1704233.
- [249] H. Sun, Y. Min, W. Yang, Y. Lian, L. Lin, K. Feng, Z. Deng, M. Chen, J. Zhong, L. Xu, Y. Peng, *ACS Catal.* **2019**, *9*, 8882.
- [250] L. M. Cao, Y. W. Hu, S. F. Tang, A. Iljin, J. W. Wang, Z. M. Zhang, T. B. Lu, *Adv. Sci.* **2018**, *5*, 1800949.
- [251] L. Yan, H. Jiang, Y. Wang, L. Li, X. Gu, P. Dai, D. Liu, S. F. Tang, G. Zhao, X. Zhao, K. M. Thomas, *Electrochim. Acta* **2019**, *297*, 755.
- [252] L. Yan, H. Jiang, Y. Xing, Y. Wang, D. Liu, X. Gu, P. Dai, L. Li, X. Zhao, *J. Mater. Chem. A* **2018**, *6*, 1682.
- [253] W. Wang, S. Xi, Y. Shao, W. Sun, S. Wang, J. Gao, C. Mao, X. Guo, G. Li, *ACS Sustainable Chem. Eng.* **2019**, *7*, 17227.
- [254] X. Li, X. Wang, J. Zhou, L. Han, C. Sun, Q. Wang, Z. Su, *J. Mater. Chem. A* **2018**, *6*, 5789.
- [255] Y. Hu, F. Li, Y. Long, H. Yang, L. Gao, X. Long, H. Hu, N. Xu, J. Jin, J. Ma, *J. Mater. Chem. A* **2018**, *6*, 10433.
- [256] Q. Hu, X. Liu, B. Zhu, L. Fan, X. Chai, Q. Zhang, J. Liu, C. He, Z. Lin, *Nano Energy* **2018**, *50*, 212.
- [257] D. Li, Z. Zong, Z. Tang, Z. Liu, S. Chen, Y. Tian, X. Wang, *ACS Sustainable Chem. Eng.* **2018**, *6*, 5105.
- [258] T. Sun, S. Zhang, L. Xu, D. Wang, Y. Li, *Chem. Commun.* **2018**, *54*, 12101.
- [259] T. Singh, C. Das, N. Bothra, N. Sikdar, S. Das, S. K. Pati, T. K. Maji, *Inorg. Chem.* **2020**, *59*, 3160.
- [260] Q. Xia, H. Liu, M. Jin, L. Lai, Y. Qiu, H. Zhai, H. Li, X. Liu, *Nanoscale* **2020**, *12*, 8969.

- [261] Z. Yu, Y. Bai, S. Zhang, Y. Liu, N. Zhang, G. Wang, J. Wei, Q. Wu, K. Sun, *ACS Appl. Mater. Interfaces* **2018**, *10*, 6245.
- [262] X. Luo, Q. Zhou, S. Du, J. Li, J. Zhong, X. Deng, Y. Liu, *ACS Appl. Mater. Interfaces* **2018**, *10*, 22291.
- [263] W. Wu, Y. Wu, D. Zheng, K. Wang, Z. Tang, *Electrochim. Acta* **2019**, *320*, 134568.
- [264] X. Shi, A. Wu, H. Yan, L. Zhang, C. Tian, L. Wang, H. Fu, *J. Mater. Chem. A* **2018**, *6*, 20100.
- [265] B. You, Y. J. Sun, *Acc. Chem. Res.* **2018**, *51*, 1571.
- [266] D. Li, E. J. Park, W. Zhu, Q. Shi, Y. Zhou, H. Tian, Y. Lin, A. Serov, B. Zulevi, E. D. Baca, C. Fujimoto, H. T. Chung, Y. S. Kim, *Nat. Energy* **2020**, *5*, 378.



**Ben Zhang** is currently a Master's student at the College of Polymer Science and Engineering, Sichuan University. His research interest is synthesizing metal–organic-framework-based catalytic materials for energy storage and conversion applications.



**Yijuan Zheng** is currently a Master's student at the College of Polymer Science and Engineering, Sichuan University. Her research interest is synthesizing functional nanomaterials related to electrocatalysis in energy conversion.



**Shuang Li** received her Master's degree at Shanghai Jiao Tong University. During her Master's period, she took part in the ERC grant 2DMATER at the Max Planck Institute for Polymer Research in Mainz, Germany in 2013. Then, she became a research scholar from 2014 at the University of Michigan, Ann Arbor. From 2015, she was doing her Ph.D. research studies in the group of Prof. Arne Thomas at Technische Universität Berlin. Now, she is doing her independent postdoctoral research at Technische Universität Berlin on the synthesis of metal–organic-precursor-based materials for electrocatalytic electrodes and devices.



**Yinghan Wang** is a full professor in the Department of Polymer Science at Sichuan University. He received his B.Eng. from East China University of Science and Technology, his M.Eng. from Sichuan University, his Ph.D. from Tokyo Institute of Technology. He joined JSR Corporation and DIC Corporation as a research fellow. His main research interests include functional membrane materials, fuel-cell proton-exchange membranes, polyimide liquid-crystal alignment materials, polymer-dispersed liquid crystals, high-performance composite materials, and energy-storage and electrocatalytic materials.





**Chong Cheng** is currently a full professor in the Department of Polymer Science at Sichuan University. He obtained his B.Sc. and Ph.D. from Sichuan University. After a research stay at the University of Michigan, Ann Arbor, USA, he joined the Freie Universität Berlin as an AvH research fellow. His current scientific interests include fabricating advanced low-dimensional materials for nanomedicines (antibacterial, virus inhibition, anti-tumor), stem cell scaffolds, electrocatalysts, and energy-related applications, especially the cutting-edge applications of coordination polymers and metal–organic frameworks.